# Processing of different sensory qualities in the olfactory bulb of *Xenopus laevis* studied by advanced line illumination microscopy

## Dissertation

for the award of the degree

"Doctor rerum naturalium"

of the Georg-August-Universität Göttingen

within the doctoral program

Göttingen Graduate School for Neurosciences, Biophysics, and Molecular Biosciences (GGNB)

of the Georg-August University School of Science (GAUSS)

submitted by

**Alexander Peter Ernst Brinkmann**
from Marburg

Göttingen 2016

## Thesis committee:

Prof. Dr. Dr. Detlev Schild
Institute of Neurophysiology and Cellular Biophysics
University Medical Center Göttingen

Prof. Dr. Tim Salditt
Institute for X-Ray Physics
Georg-August-University Göttingen

Prof. Dr. André Fiala
Department of Molecular Neurobiology of Behaviour
Georg-August-University Göttingen

## Members of the examination board:

Reviewer: Prof. Dr. Dr. Detlev Schild
Institute of Neurophysiology and Cellular Biophysics
Georg-August-University Göttingen

Second reviewer: Prof. Dr. Tim Salditt
Institute for X-Ray Physics
Georg-August-University Göttingen

## Further members of the examination board:

Prof. Dr. André Fiala
Department of Molecular Neurobiology of Behaviour
Georg-August-University Göttingen

Prof. Dr. Swen Hülsmann
University Medical Center Göttingen

Prof. Dr. Michael Müller
Department Neurophysiology and Sensory Physiology
University Medical Center Göttingen

Dr. Katrin Willig
Optical Nanoscopy in Neuroscience
Max-Planck-Institute of Experimental Medicine

## Date of oral examination:

13.09.2016

# Abstract

The olfactory system is renowned for its ability to sample and process a tremendously large odorant space. Lately, it has been shown that other sensory qualities such as temperature and pressure are detected in the olfactory system. However, little is known about how they are processed within the olfactory bulb and how this multisensory information is integrated in the context of olfaction.
In this thesis, two specific olfactory glomeruli — the mechanosensitive $\beta$- and the thermosensitive $\gamma$-glomerulus — in the olfactory bulb of *Xenopus laevis* tadpoles were analyzed by means of a custom-built line illumination microscope. The line illumination technique was combined with subtraction imaging and pixel reassignment to perform fast calcium recordings in three dimensions. These recordings, covering first- and second-order neurons in the olfactory bulb, revealed a strong interconnection of both sensitivity to temperature drops as well as mechanosensitivity with olfaction. Dual-sensitive mitral/tufted cells responding to amino acids as well as to temperature drops were located in the proximity of the $\gamma$-glomerulus. A dose-response curve for the mechanosensitivity of the $\beta$-glomerulus was measured. Additionally, the same glomerulus showed sensitivity to a surprisingly broad spectrum of single amino acids, thereby combining mechano- and chemosensitivity in the same structure. The axon separation of different olfactory receptor neurons within a single glomerulus was successful using double staining electroporation. Recordings obtained from such stainings suggest that the sensitivity of the $\beta$-glomerulus to amino acids was caused by a single broadly tuned olfactory receptor. Lastly, a sufficient resolution for single axon as well as for single dendrite recordings within the $\beta$-glomerulus was achieved by line illumination microscopy. The demonstrated increase in efficiency of the line scanning technique enables future experiments with two calcium indicators to analyze the signal transmission within a single glomerulus.

# Contents

# 1 Introduction

## 1.1 Fast confocal imaging

### 1.1.1 Why is fast imaging important?

Confocal laser scanning microscopy remains one of the workhorses in the field of neuroscience and enables, in combination with calcium imaging, the observation of large neuronal networks and their activity. Recently, the extension of fluorescent imaging into the super-resolution regime by different techniques such as STED, STORM or PALM has received considerable attention and drawn some focus back to advances in the field of optical imaging [1]. For calcium imaging the temporal imaging resolution is, however, at least as important as the spatial resolution of the imaging setup. Standard confocal laser scanning microscopes (cLSM) can achieve frame rates of a few Hz for full frame recordings (512 px x 512 px) [2]. It is crucial for a complete evaluation of neuronal networks to measure not only single planes but a sufficiently large volume. This is especially relevant at the level of the olfactory bulb with its fiber networks forming densely innervated glomeruli. Fast confocal imaging systems with frame rates of 30 Hz and more can extend the measurement into the third spatial dimension and collect several layers at the same speed at which standard cLSM setups collect single planes. The application of activity correlation imaging to distinguish mitral/tufted cell networks in 3D was successfully applied with stack rates of 2 Hz corresponding to a 40 Hz frame rate [3]. Furthermore, new developments of voltage-sensitive dyes demand fast image acquisition [4]. Besides, action potentials can be resolved with fast calcium dyes and a scanning frequency above 200 Hz [5]. In mitral/tufted cells of *Xenopus laevis* tadpoles action potentials and small calcium increments are correlated as was revealed by fast imaging with a sampling rate of 125 Hz [6]. Fast imaging can be either used to gather more temporal information and record even single action potentials or the imaging can be extended into the third spatial dimension to image large volumes of neuronal networks.

### 1.1.2 Fast confocal imaging methods

The advances in optical, confocal microscopy during the last years were not limited to the spatial resolution. Many techniques for fast imaging with frame rates of 30 Hz and more have become available. Some, like spinning-disk microscopes, are around for quite a while now [7]. Others had already been used for non-fluorescent recordings at the beginning of the last century, like light sheet microscopy [8], but were only recently applied to fluorescence microscopy [9, 10]. In addition, new scanning paradigms can increase the speed of conventional imaging methods. Resonant scanners improve the imaging speed of cLSM into the 30 Hz full frame regime [2]. Random-access scanning by means of acousto-optic deflectors has been realized in several implementations [11, 12]. The technique is usually combined with two-photon microscopy and was successfully applied to a variety of areas [13]. Even higher frame rates of up to 1 kHz for full frame recordings for calcium imaging are of course available with widefield techniques but they sacrifice the optical sectioning capability [14].

All these techniques have certain advantages and disadvantages. Light sheet microscopy, for instance, causes very little photobleaching. This enables long recording times but demands a relatively complicated positioning of the sample [15]. Furthermore, the penetration depth is limited and shadowing effects have to be compensated [16]. Random-access scanning yields the advantages of two-photon microscopy — albeit with decreases in terms of spatial resolution — but reaches the high temporal resolution only by constraining the imaging to a small number of pixels in each frame [13]. Single pixels can be recorded with acquisition rates of several kHz and the imaging can be limited to the most interesting regions by only accessing the corresponding pixels [12]. This yields, unfortunately, no benefit for the full observation of dense neuronal networks since the acquisition time for full frame recordings is not improved.
Here, line illumination microscopy was used for calcium imaging. The technique can cover large cellular networks with high frame rates. It is ideally suited for measurements in the olfactory bulb where it has already been successfully applied (e.g. [3, 17]). The sample positioning is as flexible as with a cLSM setup and especially the signal-to-noise ratio can be much better. A cLSM setup with resonant scanners and a 30 Hz full frame (512 px x 512 px) acquisition has to scan more than $260 \cdot 10^3$ points. Consequently, the pixel dwell time cannot exceed 0.13 µs. In contrast, a line

scanner acquires only 512 scan positions for the same image since the pixels along the line are recorded in parallel. The maximal line dwell time for the same frame rate is hence 65 µs. Furthermore, the technique benefits from the recent development of sCMOS cameras as will be discussed in the following section.
The concept of a line illumination microscope (LIM), as first proposed in 1974 [18], is to scan a line instead of a single point over the sample. Line scanning results in a slightly decreased lateral resolution and optical sectioning capability but provides in turn a much higher frame rate. The resolution along the line is achieved by sampling the emission line with the pixels of the line detector. Sheppard and Mao [19] analyzed the concept theoretically and since then the idea has been implemented and used in several designs (e.g. [20–22]). A custom-built version of a LIM exists in our laboratory [3] and a second version with an sCMOS camera was developed as part of my master's thesis [23]. This second sCMOS LIM was used for most of the measurements reported in this dissertation. In chapter 3.1 different methods will be implemented and analyzed to improve the efficiency of line illumination microscopes further. Simultaneously to the development of our sCMOS LIM, a similar setup was constructed by Mei et al. [24]. In contrast to their implementation, our setup is designed in a de-scanned way, i.e. the emission line is always projected to the same position on the camera chip.

### 1.1.3 Subtraction imaging and pixel reassignment

Fast imaging is typically limited by the signal-to-noise ratio (SNR) which tends to get too low if short exposure times are used. On the other hand, counteracting the decreasing SNR by opening the confocal aperture reduces both lateral resolution, and optical sectioning capability. The same trade-off is observed in line illumination microscopes. Both lateral and axial resolution are typically worse than in point scanners since the confocality is lost along the line. Techniques which improve SNR, lateral resolution and optical sectioning capabilities are thus especially interesting for line illumination microscopes.
The advances in detector technology enabled the usage of detector arrays [25] or cameras [26] for confocal imaging. The readout from small detector elements in the center ensures confocality. The remaining elements collect the light previously blocked by the physical confocal aperture. Although blocking the light in a normal confocal setup ensures the optical sectioning capability, it can now be used in more sophisticated ways to further enhance the imaging result. Two such methods are

subtraction imaging and pixel reassignment. The general idea of both methods will be discussed in the next paragraphs for point scanners, followed by the evaluation of their benefit for line illumination microscopes in chapter 3.1.2.

**Subtraction imaging** refers to the concept of calculating the final image from two recordings acquired with different pinhole sizes. The image acquired with a wide open confocal aperture is subtracted from the confocal recording with small aperture size. Sheppard and Cogswell described this method in different implementations, e.g. with a detector array setup [27]. Both, lateral resolution as well as the optical sectioning capability can be enhanced in this manner. The improvement in contrast and lateral resolution is achieved in a similar way as in the unsharp masking technique of image processing [27]. Optical sectioning is improved because the center of the detector array records in-focus as well as out-of-focus light. Areas farther away from the center are mainly hit by out-of-focus light. Subtracting the latter from the former reduces thus the out-of-focus component [28]. The beneficial effect on the optical sectioning capability has already been shown for a line scanning setup with low numerical apertures by Poher et al. [29] and will be further discussed for the line illumination microscope in sections 2.1.1 and 3.1.2.

**Pixel reassignment** is another technique using the intensities recorded in the off-center pixels for improvements of imaging quality. Müller et al. [26] realized the idea in a point scanning setup. They recorded for each pixel of the final image a whole camera frame with all off-center pixels. They named this procedure image scanning microscopy. While Müller et al. were the first to actually use such a microscope, the underlying idea had been described earlier [30] and the concept has recently been analyzed with a detector array in some detail [25]. Improvements were observed in the lateral resolution and the signal-to-noise ratio. A commercial laser scanning microscope using pixel reassignment is now available [31].
In contrast to subtraction imaging, reassignment is applied to the pixels positioned close to the center of the detector. Recording multiple pixels and adding their intensities together corresponds to a slight opening of the confocal aperture, which is in this case formed by the single detector elements of the camera. Instead of simply adding the intensities of all pixels together they are reassigned individually to the position from which they were most likely emitted. The most likely position for each recorded element is given by the product of excitation ($\mathrm{PSF}_{ex}$) and detection

($PSF_{det}$) point spread function. For the central pixel the two PSFs overlap and the most likely position is just the central position itself. For each off-center pixel the detection PSF is slightly shifted relative to the excitation PSF (cf. figure 1.1). If both PSFs have the same shape and width, the most likely position lies in between the two pixels, i.e. between the focus of the excitation and the position corresponding to the detection pixel. The recorded intensities can be reassigned accordingly, either by interpolation or by recording the image with a scan size of half the pixel size [25]. The latter avoids the need for interpolation (cf. figure 1.1). The reassignment increases SNR, and, since the overlap between the two PSFs gets narrower with displacement, the resulting effective PSF is also narrower. Consequently, the reassignment of all pixels improves the resolution. It is possible to implement the concept in a fully optical way as was recently demonstrated [32].
To our knowledge, pixel reassignment has not yet been realized with a line illumination microscope. The benefit of this technique for line illumination microscopy will be evaluated in section 3.1.2.

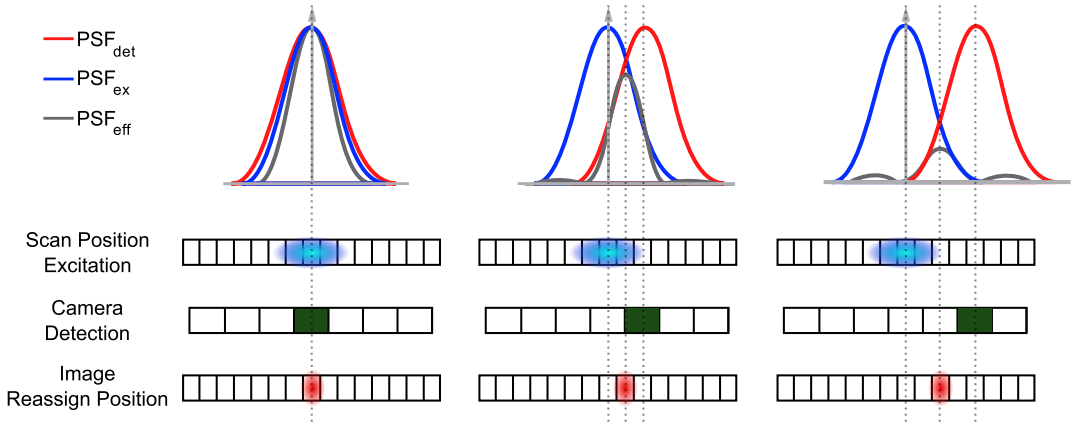


***Figure 1.1*** – *Concept of pixel reassignment. First image, the scan position and the position of detection overlap. This is always the case in normal acquisition mode. Second and third image, readout of off-axis detector elements. The $PSF_{ex}$ and the $PSF_{det}$ are shifted relative to each other. The product of the two functions defines the most likely position for the recorded intensity. The reassignment position for each recorded detector element coincides with a pixel of the final image because the scanning is depicted with a scan pixel size half as big as the single detector elements.*

## 1.2 The olfactory system of *Xenopus laevis*

Olfaction constitutes a very interesting and active research area. While our knowledge about the olfactory system has considerably improved over the last years, new findings typically also lead to new questions demanding further investigations. Some of the recent reviews dealing with the olfactory system revealed the intriguing complexity, capability, and relevance of this system (e.g. [33–36]).

### 1.2.1 Why *Xenopus*?

This thesis work investigated *Xenopus laevis* tadpoles. Why were these animals chosen for the experiments?

First of all, it is worthwhile to mention that the organisation of the olfactory system is very well preserved across species. Many findings observed in one animal model were relevant for different species [37, 38]. Furthermore, *Xenopus* is widely used for scientific experiments and is closer related to humans than other animals commonly used in olfactory research such as Zebrafish, *Drosophila* or *Caenorhabditis* [39].
A significant advantage of *Xenopus laevis* tadpoles is the accessibility of the olfactory system. The olfactory epithelia, nerves and bulbs can be obtained in one preparation [40, 41]. Various staining techniques for dye loading with calcium indicators exist [17], and the breeding efficiency is high enough to allow a sufficient number of representative experiments [39]. Gascuel and Amano described in their review [42] numerous opportunities specifically available for research on olfaction in *Xenopus laevis* and *Xenopus tropicalis*. They name several aspects of *Xenopus* ecology, such as the combination of aquatic and aerial olfaction, which make this animal model especially interesting.
Lastly, recent findings have characterized the $\gamma$-glomerulus in the olfactory system of *Xenopus laevis* as temperature-sensitive, and some indications were found for a mechanosensitive structure in the olfactory bulb [43, 44]. *Xenopus laevis* is thus a promising animal model for further investigations into the topic of different sensory qualities processed in the olfactory system.

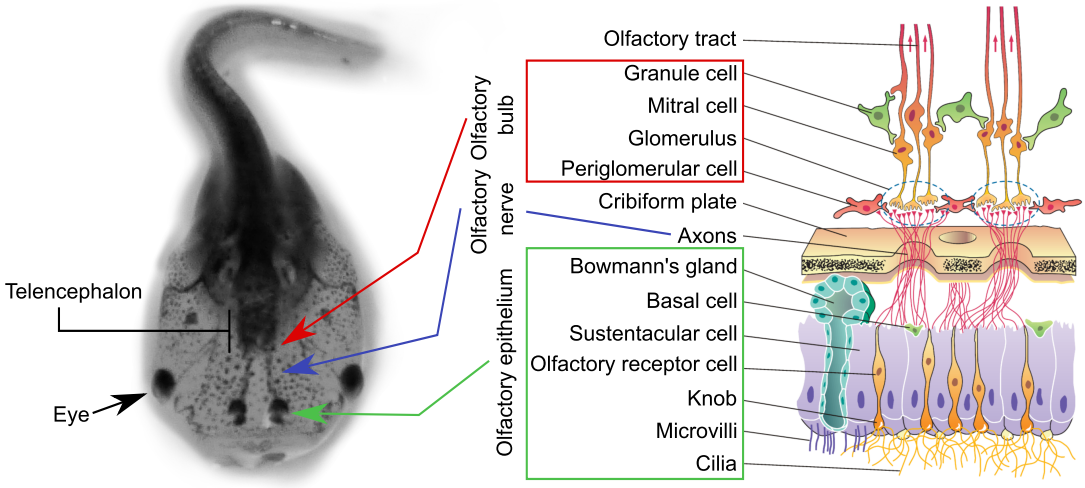


***Figure 1.2*** – *The right side of the image shows a sketch of the general organization of the olfactory system from the olfactory epithelium over the nerve to the olfactory bulb. The corresponding compartments are indicated in the image of a Xenopus laevis tadpole on the left side. Sketch modified from [45].*

### 1.2.2 General organization of the olfactory system

Figure 1.2 provides a general overview of the olfactory system:
Olfactory perception begins at the nasal epithelium where an odorant binds to olfactory receptors expressed on the cilia or microvilli. Cilia or microvilli emerge from the dendritic knob belonging to a bipolar olfactory receptor neuron (ORN). They are surrounded by the mucus produced by sustentacular cells and the bowman's glands [46, 47]. The mucus forms the border zone between olfactory epithelium and the environment. Basal cells in the olfactory epithelium provide its regenerative capacity [48].
Olfactory signals in vertebrates are often, but not always, transduced by a cAMP pathway [49–51]. In *Xenopus laevis* tadpoles some of the ORNs use the cAMP pathway, however, many others do not and these are amino acid-sensitive [52]. The latter depend probably on a PLC pathway, although also PLC- and cAMP-independent cells were observed [53].

ORN axons fasciculate into the olfactory nerves and terminate in the OB in skein-like structures called glomeruli. Each ORN is generally believed to express only one olfactory receptor (OR) but there seem to be exceptions to this rule [54]. These

exceptions are only partially explained by a transient expression of multiple ORs during development [55]. The OR expressed in a certain ORN bestows it a specific sensitivity to a subset of odorants. Furthermore, ORNs expressing the same OR project mostly to the same glomerulus or to a small number of glomeruli [56]. Thus, olfactory coding relies potentially on a spatial activation map of glomeruli, but also on temporal coding including latency coding of mitral/tufted cells (M/T cells) [17, 33, 57].
The glomeruli formed by axons from the ORNs are innervated by dendrites of the M/T cells. The M/T cells in turn project to higher brain areas.

### 1.2.3 The olfactory bulb of *Xenopus laevis* tadpoles

Figure 1.3 (A) shows an overview of the olfactory system of *Xenopus laevis* tadpoles with emphasis on the olfactory bulb. The latter is structured in several layers. Axons of ORNs terminate in the glomerular layer in glomeruli and form synapses with the dendrites of the M/T cells. This layer also harbors a relatively small number of periglomerular cells, each of which forms broad arborizations covering multiple glomeruli [58]. Periglomerular cells generally shape incoming olfactory signals via inhibition but are still lacking tufts within glomeruli in premetamorphic *Xenopus laevis* [58]. The next layer is the mitral cell layer containing the somata of M/T cells, followed by the granule cell layer. Granule cells establish reciprocal synapses with the M/T cells. M/T cells can be stained via pressure injection (bolus loading) of AM dyes as depicted in figure 1.3 (A). Typically, the ventral side of the main olfactory bulb is imaged since most of the glomeruli are located there.

Olfactory receptor neurons of the main olfactory epithelium terminate in about 350 glomeruli [59]. These can be segregated in 4 main compartments [59]. A separation into smaller compartments was suggested by Gaudin and Gascuel [60]. Yet, these smaller compartments cannot be distinguished reliably in calcium imaging experiments with whole mount preparations. Figure 1.3 (B) shows a maximum projection of the olfactory bulb where ORNs were labeled via electroporation. The four compartments mentioned aforehand are outlined. The lateral cluster consists of about 175 glomeruli [59] and corresponds to the projection fields 4-6 in the classification of Gaudin and Gascuel [60]. The medial cluster is positioned close to the border of the contralateral bulb and harbors about 100 glomeruli. It encloses the projection fields 1, 2 and 9. The intermediate cluster lies in between the medial and lateral cluster

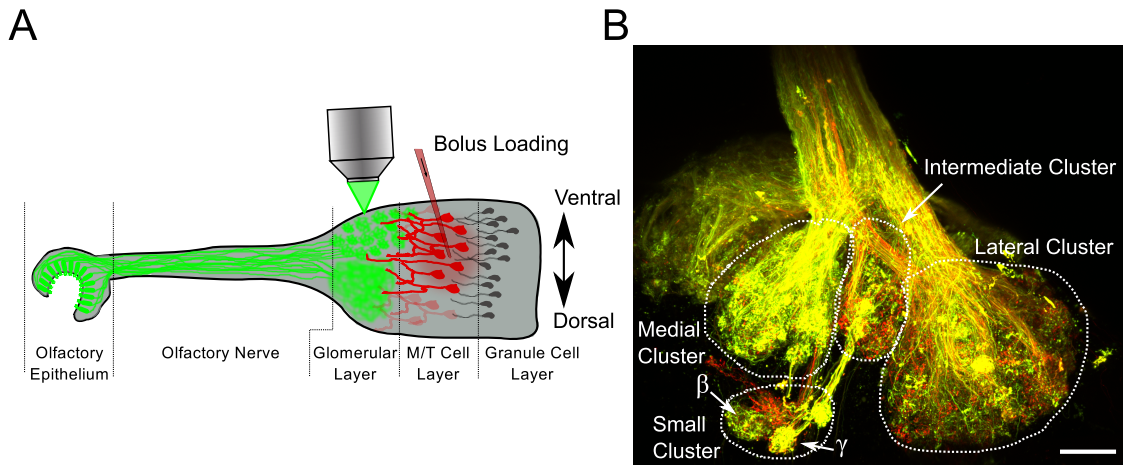


***Figure 1.3*** *– **(A)** Sketch of the olfactory system of larval Xenopus laevis. The different layers of the olfactory bulb are indicated. ORNs (green), M/T cells (red) and granule cells (gray) are displayed. Not shown are the periglomerular cells situated between the glomeruli. **(B)** Maximum intensity projection of a 145-µm-thick scan through the olfactory bulb after electroporation with different Alexa Fluor dyes recorded with an LSM 780 (Zeiss). Scale bar, 50 µm.*

---

and contains about 70 glomeruli corresponding to the projection fields 3 and 7. Finally, the small cluster refers to 4 or 5 glomeruli separated from the other clusters and is probably part of the projection field 3. Glomeruli in *Xenopus laevis* tadpoles have no distinct borders as typically observed in mammals. They are therefore often difficult to distinguish by means of fluorescent labeling alone. Fortunately, the $\beta$- and the $\gamma$-glomerulus (indicated in figure 1.3 (B)) belonging to the small cluster are an exception. They can be easily found back in different preparations due to their distinct position and are clearly distinguishable from other glomeruli.

The innervation patterns of both ORNs and M/T cells in *Xenopus laevis* tadpoles are different from the ones observed in mammals:
**ORN** axons often bifurcate multiple times before innervating more than one glomerulus [61, 62]. In mice each ORN innervates only one glomerulus [56]. Furthermore, ORNs in *Xenopus laevis* are also known to branch regularly before innervating the same glomerulus from two different sides [62]. They branch again extensively within the glomerulus.
**M/T cells** innervate multiple glomeruli in amphibians but typically only one in mammals [34, 63]. In *Xenopus laevis* M/T cells innervate on average more than one

glomerulus [58].

### 1.2.4 Olfactory stimuli

Olfactory stimuli for larval *Xenopus laevis* must be water-soluble since pre-metamorphic animals live in aquatic environments. The following stimuli were used throughout the thesis since they are well known to be effective for the main olfactory bulb:

**Amino acids** are important stimuli used in many experiments with *Xenopus laevis* tadpoles as they are potential food signals [64]. The responses evoked by amino acids are predominantly observed in ORNs which do not express the cAMP-pathway [52] and project to the lateral cluster [65]. Amino acids are widely used in Zebrafish studies (e.g. [66, 67]).
**Amines** are also considered as food signals [68] and trigger responses in all clusters of the olfactory bulb [65]. The same is true for **bile acids** which are considered to be relevant for social interactions [64, 65].
Finally, **alcohols, ketones and aldehydes** cause responses predominately in the medial cluster [65].

## 1.3 Non-chemical stimuli processed by the olfactory system

The predominant role of the olfactory system is to sample a large range of molecules which are either available air-borne or water-soluble. Odorants carry a wide range of valuable information about potential food sources, other animals or about potential dangers, like predators. The olfactory system is thus equipped with an impressive number of olfactory receptor genes. About 1000 were found in rodents, about 100 in fish and about 400 in *Xenopus tropicalis* [38, 69, 70].
In addition to the chemosensitivity, it might be beneficial for the olfactory system to obtain information about other modalities like temperature or mechanical stimulations. It is likely that both temperature as well as flow changes in the water or air passing through the nostrils significantly change the binding properties of odorants to ORs. Monitoring these parameters and potentially calibrating the processing of odorants accordingly might be necessary for the olfactory system.

Both temperature as well as mechanical stimuli were found to be registered in the olfactory system. Temperature changes presented as stimuli to the nose induced the activation of neurons in the Grüneberg ganglion (GG), a subsystem of the olfactory system of rodents, including mice, rats and hamsters [71, 72]. In *Drosophila* temperature information is conveyed to the mushroom body, a structure dedicated to olfaction among other tasks [73]. Mechanical stimulation triggered responses in many ORNs of the septal organ and the main olfactory epithelium in mice [74]. Observations of these two additional stimuli qualities in the olfactory system of mice were so far limited to the nose. The processing of these stimuli and their interconnection with the rest of the olfactory system remains thus elusive. The next sections will briefly summarize the current knowledge about temperature and mechanosensitivity in the olfactory system of mice as a well studied example and for our target species *Xenopus laevis*.

### 1.3.1 Thermosensitivity in the mouse olfactory system

Grüneberg ganglion neurons in mice respond to cold stimuli as well as alarm pheromones and other odorants but not to temperature increases [71, 75–78]. The thermosensitive GG neurons are, furthermore, responsive to dimethylpyrazine [78]. GG neurons project to the necklace glomeruli of the olfactory bulb [79]. Yet so far no studies investigated temperature-induced responses on the level of the necklace glomeruli. GG neurons show a dynamic response range to temperature decreases up to 10 °C [80]. The transduction cascade of the temperature-sensing GG neurons is cGMP-mediated [72, 81, 82].

Several theories have been discussed regarding the advantage of having a temperature-sensitive structure within the olfactory system. Among them were the possible synchronization of the breathing cycle [83] and the induction of a stress response caused by both chemical and temperature signals [80]. The separation from the mother in low temperature environments might be a reason for such an alarm signal [80].

### 1.3.2 Thermosensitivity in the *Xenopus laevis* olfactory system

Temperature drops presented as stimuli to the olfactory epithelium of *Xenopus laevis* tadpoles cause activity in one specific glomerulus, the $\gamma$-glomerulus, of the olfactory

bulb [43, 44]. Backtracing revealed that ORNs in the main olfactory epithelium are innervating the $\gamma$-glomerulus. Temperature increases did not elicit responses. No chemical stimuli activating the $\gamma$-glomerulus were found, including dimethylpyrazine and menthol. The dose response curve revealed a half-maximum at temperature changes of about -2.7 °C, a value which depended also on the ambient temperature. Furthermore, the temperature-evoked signal is transferred to the second-order neurons in the olfactory bulb. These M/T cells reacted with a range of different dynamics to the stimuli. Finally and remarkably, the $\gamma$-glomerulus is innervated by fibers from ORNs of both nasal cavities. They travel through the contralateral bulb and cross the anterior commissure to the ipsilateral bulb where they backproject to the $\gamma$-glomerulus. These fibers convey information as was shown by dissecting the ipsilateral olfactory nerve and monitoring responses in the M/T cell layer to temperature stimuli induced at the contralateral olfactory epithelium [44].

These results were acquired by Eugen Kludt and were communicated in his PhD dissertation [43]. The results were later published [44] together with the additional findings made in this thesis which will be presented in the results section 3.2.2.

### 1.3.3 Mechanosensitivity in the mouse olfactory system

Grosmaitre et al. [74] demonstrated the sensitivity of ORNs to puffs — i.e. outflow from a pipette tip elicited by pressure application — with Ringer's solution in mice. A large number of ORNs in the septal organ (∼70 %) and in the main olfactory epithelium (∼50 %) were reported to be sensitive to pressure puffs. In addition, these neurons responded to chemical stimuli. Knock-out experiments revealed that both, the chemosensitivity and mechanosensitivity, were mediated by a cAMP cascade. Repeated stimulation with pressure pulses caused adaptation. A different study performed by Connelly et al. [84] brought evidence that this mechanosensitivity relies on the expression of olfactory receptors. Thus, certain ORs like the SR1 receptor trigger responses to chemical and mechanical stimuli. The SR1 receptor was in turn described as broadly selective to different chemicals [85].

Preliminary experiments conducted on larval *Xenopus laevis* suggested that a small part of the olfactory bulb is activated by pressure changes applied to the epithelium [43].

## 1.4 Scope of the thesis

The dissertation covers three main topics which build on one another. Firstly, section 3.1 will deal with the development of new measurement techniques for fast calcium imaging in neuronal networks for which the demand was discussed in section 1.1.1. Secondly, section 3.2 will be dedicated to the analyses of different sensory qualities processed in the olfactory system — a topic which has lately received considerable attention (compare section 1.3). Lastly, section 3.3 will introduce 2-channel calcium recordings in the olfactory bulb.

**Line Illumination Microscopy for fast 2-channel 3D-imaging**

The first aim of the thesis was to adjust the line illumination microscope for the subsequent measurements and shape it into a suitable tool for fast calcium recordings in three spatial dimensions and two channels. This required changes in the microscope design to increase efficiency as well as the evaluation of the two reconstruction techniques, subtraction imaging and pixel reassignment.

**Different sensory qualities processed in the small cluster**

The aim of the second part was to investigate the processing of mechano- and thermosensitivity and their integration into the olfactory system. The data available in the literature about temperature- and mechanosensitivity of mice was acquired at the level of the nose (cf. section 1.3). As a consecutive step, this thesis' work addressed the next level, the olfactory bulb. The final implementation of the LIM was used to determine the properties of the small cluster in *Xenopus laevis* tadpoles.

**Opportunities and limitations of 2-channel calcium recordings**

Based on the two previous topics, the last part of the thesis was dedicated to simultaneous recordings with two calcium dyes and focus on the small cluster. The assessment of possibilities and limitations of such measurements with line illumination microscopy was the goal of the last part of the thesis. While the sequential measurement of first- and second-order neurons with calcium-sensitive dyes in the olfactory system is well-established, simultaneous recordings with two calcium dyes within a single glomerulus are entirely new.

# 2 Materials and Methods

## 2.1 Line illumination microscopy

Most experiments in this thesis were performed with a newer, 2-channel version of the custom-built 1-channel line illumination microscope described by Junek et al. [3]. The new setup was developed in 2011 specifically for fast recordings with two fluorescent channels as part of my master's thesis [23]. A full frame sCMOS camera (Neo sCMOS, Andor, Northern Ireland) was used as detector in contrast to the previously existing line-camera version. A similar setup, combining line scanning with an sCMOS camera, was constructed by Mei et al. [24] in a non-de-scanned way around the same time. In our de-scanned pathway the emission line remained in a fixed position on the camera chip and the image was reconstructed afterwards line-by-line as depicted in Figure 2.1. The excitation laser line was scanned over the sample (Figure 2.1 (A)) and a camera image was recorded for each position capturing the emission line. Figure 2.1 (B) shows the emission line on the camera chip for two different time points, i.e. two different positions of the excitation line. Independent on the position of the excitation line, the emission line on the camera chip remained in the same position. Consequently, always the same active sensor area was recorded. The de-scanning enabled us to change the confocality after the measurement by binning more or less pixels perpendicular to the line on the camera chip. The limited pixel size acted as an aperture ensuring confocality. One can thus not only collect the central line on the camera chip but also its neighbors, containing different ratios of in- and out-of-focus light. The additional lines were useful for subtraction imaging or pixel reassignment as will be described in the following sections. Figure 2.1 (C) shows a magnification of the emission line on the camera at a certain timepoint. The different lines used for normal confocal imaging (red), subtraction imaging (red+blue) and pixel reassignment (red+green) are indicated. The term 'camera line' will be used throughout the dissertation for lines on the camera composed of 2048 individual pixels but with a width of only one pixel and oriented

in the same way as the line created by the emission light. All line operations were performed individually for each of the constituting pixels. Figure 2.1 (D) shows images of Alexa 647 stained ORN axons calculated with the different reconstruction techniques. The data for all reconstructions was obtained from the same recording.

It was necessary to make a number of changes to the existing setup during the course of the experiments to enhance efficiency as well as temporal and spatial resolution. Therefore, the adjusted setup will be described in some detail in section 3.1. If not stated otherwise, all imaging experiments in this thesis were performed using the 2-channel line illumination microscope. Two 40x and one 63x water immersion objectives were used for imaging with numerical apertures of 0.8, 1.0 and 1.0, respectively.

### 2.1.1 Subtraction imaging

The concept of subtraction imaging was first successfully implemented for a basic line scanner with an array of LED lines as excitation sources by Poher et al. [29]. Subtraction imaging had already been tested with our specific setup during my master's thesis [23]. However, technical limitations of the camera system available at that time prevented the application of subtraction imaging in combination with frame rates higher than 5 Hz. This problem was overcome during the course of this thesis by implementing a newer sCMOS camera (Orca Flash 4.0, Hamamatsu) (cf. section 3.1.1).

The principle of subtraction imaging is to remove out-of-focus light from the normal recording containing both in-focus as well as out-of-focus components. This is achieved by subtracting an image acquired with a larger confocal aperture. For our line-scanning system we implemented the technique in a slightly different way by subtracting lines at the border of the active sensor area from the central line. The active sensor spanned an area corresponding to an aperture of about 8 airy units (AU). Figure 2.2 illustrates the generation of the emission line on the camera: The solid line represents light emerging from the in-focus layer of the sample and is focused via several lenses onto the central line of the detector. Light emerging from out-of-focus layers, as indicated exemplary by the dashed lines, is not focused directly on the sensor and thus hits a larger area on the camera. The intensity $I_0$ recorded by the central line of the active camera chip is consequently composed of

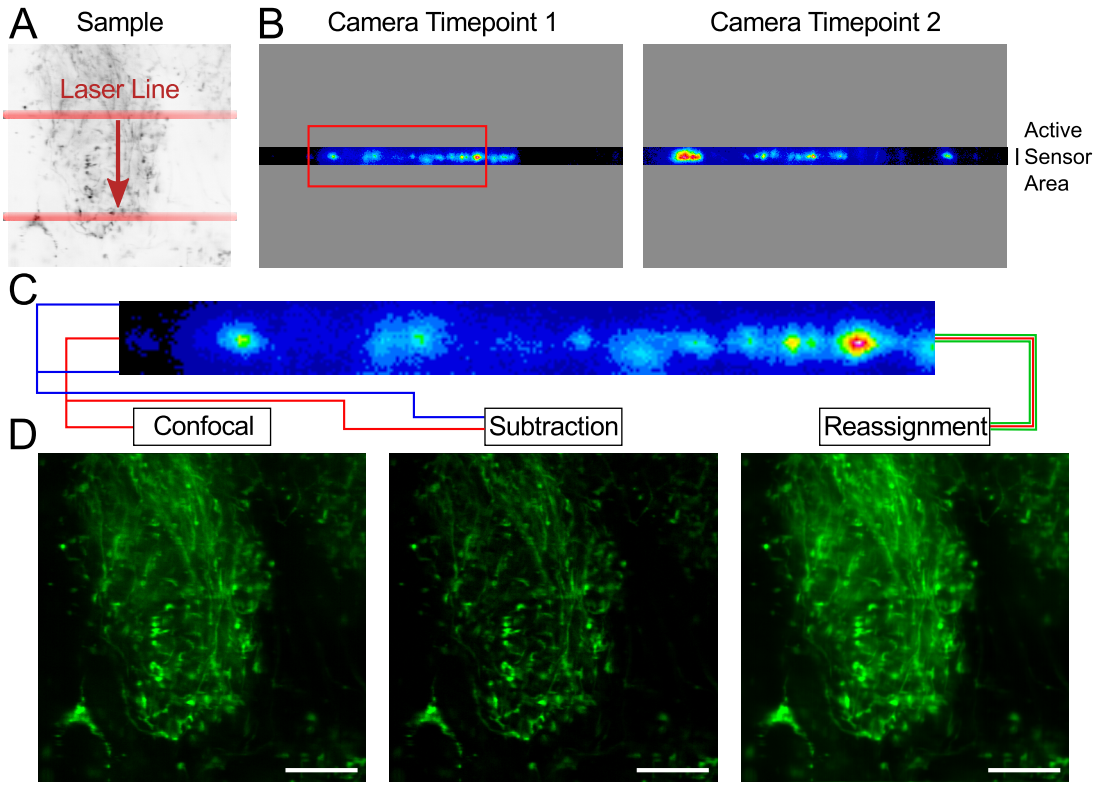


***Figure 2.1*** *– **(A)** The sample is scanned with the excitation laser line. **(B)** For each scan step the active pixel area on the camera chip is readout. The emission light is always focused to the same area on the camera chip. **(C)** Magnification of the emission line indicated with the red rectangle in (B). The camera lines used for a normal confocal recording (red), subtraction imaging (red+blue) and pixel reassignment (red+ green) are indicated. **(D)** Measurement of ORN terminals with the different reconstruction techniques. Intensity values are normalized. Scale bar, 20 µm*

---

an in-focus component $I_{in}$ and an out-of-focus component $I_{out}$:

$$I_0 = I_{out} + I_{in} \ . \tag{2.1}$$

Lines which are further away from the central line ($\pm x$ pixels) are mainly hit by out-of-focus light:

$$I_{\pm x} \approx I_{out} \ . \tag{2.2}$$

The undesired out-of-focus component on the central camera line (white line in figure 2.2) can thus be reduced by subtracting lines at the border of the active pixel

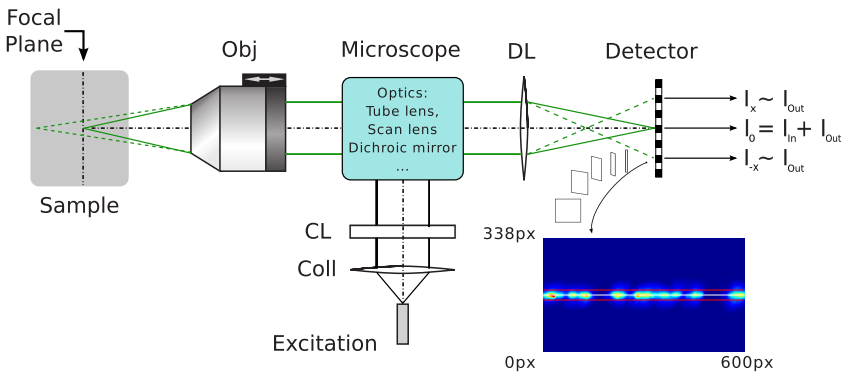


***Figure 2.2*** *– Sketch of the subtraction imaging concept for a line illumination microscope. The laser light excites fluorophores within the focal plane of the sample. The in-focus emission light (solid green line) is focused via several optical components on the detector. The out-of-focus light emerging from the sample is indicated exemplary with the green dashed lines and hits a larger number of lines on the detector. Lower right corner, segment of the emission line recorded by the camera chip. Coll, collimator lens. CL, cylindrical lens. Obj, Objective. DL, detector lens.*

area (red lines in figure 2.2):

$$I_s = I_0 - \gamma \cdot \left( \frac{I_{-x} + I_{+x}}{2} \right) \ . \tag{2.3}$$

Here, $I_s$ is the intensity of the central line after subtraction, and $\gamma$ is a scaling factor set to values between 0.8 and 1 to ensure that all pixels containing structure are assigned non-negative values. The average of several lines at the border of the active camera area can be used for subtraction. Typically, the average of 4-6 such lines yielded the best results. Since each line consists of 2048 pixels the line subtraction is of course performed on a pixel-by-pixel basis.

### 2.1.2 Pixel reassignment

The concept of pixel reassignment for a point scanner was introduced in section 1.1.3. Its implementation in a line scanning setup is less demanding, especially in terms of necessary computational power, since the reassignment can only be performed in the direction perpendicular to the scanning line. For the same reason is the improvement to the microscope's resolution constrained.

For pixel reassignment the scan pixel size was chosen to be half as big as the detector pixel size to avoid the need for interpolation during reassignment. The reassignment was performed for a total of 4 lines in this thesis, i.e. the two adjacent lines on either side of the central line. These can be recorded without any decrease in camera readout speed. Let $I_x(d)$ be the intensity of the line $x$ on the camera where 0 refers to the central line and $\pm 1$ to its direct neighbors and $d$ the scanning position of the line which corresponds to the line number in the final image. Then the intensity $I_r(0)$ for a given line of the final image after reassignment is:

$$I_r(0) = I_0(0) + \sum_{n=1}^{N} I_{\pm n}(\mp n) \ . \tag{2.4}$$

### 2.1.3 Evaluation of imaging performance

The lateral resolution, optical sectioning capability and the signal-to-noise ratio (SNR) were determined by different methods in order to evaluate the performance of the line illumination microscope in combination with subtraction imaging and pixel reassignment.

**The lateral resolution** was determined by measuring small fluorescent beads below the resolution limit with a diameter of 170 nm (PS-Speck™ Microscope Point Source Kit, Thermo Fisher Scientific, Carlsbad, USA). The intensities along the three main axes of each measured bead were fitted individually by a one-dimensional Gaussian and the full width half maximum (FWHM) of the fit was calculated as a measure for the respective resolution. The results of multiple beads were averaged. In addition, the theoretical lateral resolution ($d_{lat}$) is given by the Rayleigh-Criterion:

$$d_{lat} = \frac{0.61 \cdot \lambda_{em}}{\mathrm{NA}} \ . \tag{2.5}$$

Here $\lambda_{em}$ is the emission wavelength and NA the numerical aperture of the objective. The axial resolution $d_{ax}$ can also be calculated:

$$d_{ax} = \frac{0.88 \cdot \lambda_{ex}}{n - \sqrt{n^2 - \mathrm{NA}^2}} \ , \tag{2.6}$$

where $\lambda_{ex}$ is the excitation wavelength and $n$ the refractive index (for water immersion $n \approx 1.33$).

**The optical sectioning capability** was tested by measuring a thin and uniformly labeled fluorescent layer similar to the one used by Poher et al. [29]. A thin layer approximates the typical situation of densely labeled biological samples better than a single bead and is thus more suitable to determine the effect of subtraction imaging. Since a thin layer, ideally below the resolution limit, was not commercially available, an equivalent method after Model and Blank [86] was used. Basically, a high concentration of Fluorescein sodium salt solution (0.9 g/ml) was pressed between a cover slip and an object slider which approximates a thin fluorescent layer due to the limited penetration depth of the excitation light in the strongly absorbing solution [86].

**The signal to noise ratio (SNR)** was compared between the different imaging methods similar as described by Mei et al. [24]. A fluorescently labeled bead of 1 µm diameter (FluoSpheres, Thermo Fisher Scientific) was fixed to an object slider, covered with a thick layer of Fluorescein sodium salt solution with a concentration of 2 µg/ml and then scanned. The Fluorescein solution generated a strong background of out-of-focus light. The signal-to-noise ratio was defined according to Mei et al. [24] as the intensity measured in the center of the bead $I_C$ minus the background intensity $I_B$ divided by the standard deviation of the background intensity $\sigma(I_B)$:

$$\mathrm{SNR} = \frac{I_C - I_B}{\sigma(I_B)} \ . \tag{2.7}$$

The background intensity $I_B$ was defined as the average value of the area surrounding the bead.

## 2.2 Animals and sample preparation

All preparations were performed in agreement with the guidelines approved by the Göttingen University Committee of Ethics in Animal Experimentation. *Xenopus laevis* tadpoles of either sex and of stages from 50-56 were used for experiments according to the classification by Nieuwkoop and Faber [87]. The animals were bred in the laboratory.
The following methods for sample preparation and staining were all described in detail in our method paper [41].

### 2.2.1 Electroporation

Olfactory receptor neurons and their axonal fibers terminating in glomeruli were stained by electroporating the olfactory epithelium of the tadpoles with dextran-conjugated (10 kDa) fluorophores. The electroporation procedure for ORNs in tadpoles was previously described by Junek et al. [17]. The desired dextran-conjugated dyes were dissolved in a small amount of distilled water, typically 100 µl for the 5 mg units in which the dye was delivered. Crystals were produced by letting small droplets of the solution dry over night on a sheet of parafilm. The crystals can be stored for several month at -18 °C [41].
Non-calcium-sensitive Alexa Fluor dyes (Alexa Fluor 488, Alexa Fluor 594, Alexa Fluor 647, Alexa Fluor 680; Thermo Fisher Scientific) or the calcium indicator Calcium Green (Thermo Fisher Scientific) were chosen for ORN electroporation, using dextran conjugates.
At the beginning of the procedure the tadpole was anesthetized by placing it for one minute into a 0.02 % MS-222 (w/v, Sigma-Aldrich) solution. Afterwards the animal was fixed on a silicon cushion without harming it and placed under a binocular microscope. The area surrounding the nostrils was dried with a piece of tissue. Then dye crystals were placed into both nostrils where they dissolved. Crystals were added until they formed a saturated solution within the nostrils. One platinum electrode (cathode) was placed into the nostril and the second electrode (anode) was positioned nearby on the skin of the tadpole. A pulse train consisting of 6 pulses with a frequency of 2 Hz, a pulse duration of 20 ms and an amplitude of 20 V was delivered. Afterwards, the tadpoles were fed and kept 2-7 days under low light conditions. At least 24 h were allowed for recovery prior to sample preparation.
Double electroporation with multiple dyes was performed on different days with at least one day separating sessions.

### 2.2.2 Whole mount preparation

Tadpoles were anesthetized in ice-water where they remained for at least 3 minutes. The animal was decapitated directly afterwards. Subsequently, a tissue block comprising both nasal cavities, the olfactory nerves and the forebrain with the olfactory bulb was isolated. Next, the tissue block was flipped, exposing the ventral side upwards and was covered with a drop of Ringer's solution containing (in mM) 98 NaCl, 2 KCl, 1 $CaCl_2$, 2 $MgCl_2$, 5 glucose, 5 Na-pyruvate, 10 HEPES. The pH

and osmolarity of the Ringer's solution were adjusted to pH 7.8 and 230 mOsmol $l^{-1}$, respectively. Fine scissors were used to remove the meninges above the telencephalon. The sample was then transferred to a recording chamber filled with Ringer's solution and secured with a small net. The imaging was performed with upright microscopes, hence the ventral side had to point upwards. Accordingly, the nasal cavities ended up pointing downwards. To ensure that all stimuli effectively reached the nasal epithelia, the tissue just in front of the two nasal cavities rested on a string of the net thus lifting the nasal cavities slightly up.

### 2.2.3 Bolus loading

M/T cells in the olfactory bulb were stained after the whole mount preparation via bolus loading. This technique stains predominantly M/T cells but no axon terminals of the olfactory receptor neurons [43]. It thus labeled the complementary neuropil of the glomeruli after staining the presynaptic fibers via electroporation. For bolus loading stock solutions of Fluo-8 acetoxymethyl (Fluo-8 AM, Teflabs, Austin, USA) dissolved in DMSO and 20 % Pluronic F-127 (w/v) were prepared and stored at -18 °C. Prior to staining, the stock solution was diluted in Ringer's solution to a concentration of 250 µM with a remaining concentration of <5 % DMSO (v/v) and <1 % Pluronic F-127 (w/v, Sigma-Aldrich). The solution was then filled into a patch pipette pulled from borosilicate glass capillaries with a final tip diameter of $1 - 5$ µm. Afterwards, the pipette was mounted into a micromanipulator and carefully lowered under the microscope onto the olfactory bulb. Subsequently, the pipette was inserted into the tissue while applying a small positive pressure of 25 hPa to avoid clogging. For staining a specific glomerulus, the pipette tip was positioned approximately 50 µm rostrally to the region of interest and at a depth of 70 µm into the tissue. After reaching the desired position, the Fluo-8 AM solution was pressure-ejected with $100 - 250$ hPa depending on the size of the pipette tip for about 10 min. This procedure was repeated up to three times per olfactory bulb. About 30 minutes were allowed between the last dye application and the start of the experiments for uptake and de-esterification of the AM-coupled dye.

## 2.3 Stimulation with odorants, temperature and pressure

### 2.3.1 Solutions

Brain preparations were kept under a constant flow of Ringer's solution (recipe see section 2.2.2) during all measurements. The following chemicals — either purchased from Sigma-Aldrich or Merck — were dissolved in Ringer's solution and used as chemical stimuli:

**Forskolin (For)**, an activator of adenylyl cyclase and thus the cAMP-mediated pathway in ORNs, was applied as a stimulus at a concentration of $15 - 25$ µM.

**Amino acids (AA)** were used individually at a concentrations of 200 µM if not stated otherwise. The applied mixtures and subgroups were based on Caprio and Bird (1984) [88], Manzini et al. (2007) [89] and Kludt et al. (2015) [44]. The mixture of all individual amino acids (200 µM each) contained the following four subgroups:
Long-chain neutral (LCN): L-proline (Pro), L-valine (Val), L-leucine (Leu), L-isoleucine (Ile), L-methionine (Meth).
Short-chain neutral (SCN): L-glycine (Gly), L-alanine (Ala), L-serine (Ser), L-threonine (Thr), L-cystein (Cys).
Basic (BAS): L-arginine (Arg), L-lysine (Lys), L-histidine (His).
Aromatic (AROM): L-phenylalanine (Phe), L-tryptophan (Trp).
The amino acids L-glutamate, L-aspartate, L-glutamine, and L-aspargine were omitted in the mixture and as individual stimuli since they have direct effects on OB neurons [89].

**Amines** were only applied as a mixture containing the following at 200 µM each: 2-phenylethylamine, tyramine, butylamine, cyclohexylamine, hexylamine, 3-methylbutylamine, N,N-dimethylethylamine, 2-methylbutylamine, 1-formylpiperidine, 2-methylpiperidine, N-ethylcyclohexylamine, 1-ethylpiperidine, and piperidine.

**Alcohols** were used as a mixture only which contained the following at 200 µM each [90]: Beta-ionone, citral, beta-phenylethyl alcohol and gamma-phenylpropyl alcohol.

**Bile acids** were purchased from Sigma-Aldrich in a mixture containing 200 µM taurocholic acid and traces of glycocholic, dexoxycholic and other bile acids.

### 2.3.2 Odorant and temperature stimulation

Preparations were constantly perfused with room temperature Ringer's solution through a gravity-fed custom-built funnel applicator [91]. The outlet of the funnel was placed close to the epithelium but not pointing directly at it to avoid flow changes at the epithelium (cf. Figure 2.3). Furthermore, the funnel applicator was specifically designed to minimize pressure changes in the outflow by means of a funnel overflow [91]. A syringe needle connected to a vacuum pump was used as outflow. Its positioning ensured that stimuli added to the flow did not reach the olfactory bulb. Only the epithelium was perfused with higher concentrations of the stimuli as was checked by recording the intensity distribution of Fluorescein added in the same way as odorant stimuli.
Odorants were directly added to the funnel into the continuous Ringer's solution flow. Quantities of 400 µl were released by a triggered electronic pipette (HandyStep electronic, Brand, Wertheim, Germany). Interstimulus intervals within the same measurement were at least 20 s long and most often longer than 30 s. A minimum interval of 1 min was allowed between measurements for recovery. The reproducibility of the responses was checked regularly by repeated application of the same stimulus over the course of the measurements. The funnel was rinsed with pure Ringer's solution in between odorant applications.
The temperature experiments were performed similar to the odorant stimulations. Cooled Ringer's solution was used as stimulus in place of the chemicals. Adding Ringer's solution at 0 °C typically led to a drop of $\Delta T$ = -1 °C at the olfactory epithelium as measured by a NiCr-Ni thermocouple (Greisinger Elektronik).

### 2.3.3 Mechanical stimulation

Mechanical stimulation of the olfactory epithelium was achieved by short pressure ejections of odorant free Ringer's solution through a glass pipette. The 350 µm wide opening of the pipette was placed approximately 0.9 mm in front of the olfactory

epithelium. The rather large opening in combination with the distance to the nostril ensured that the whole epithelium was uniformly hit by the pulses. The pipette was connected to a reservoir of odor free Ringer's solution to which pressure could be applied by a pressure ejection device (PDES-02L, npi, Tamm, Germany). Pressure pulses with an amplitude of $0-250$ hPa were applied for stimulation and the pressure strength was recorded during the measurement. The Ringer's solution ejected from the pipette tip formed cones with a small angle leading to a decrease of pressure amplitude with distance to the tip. The diameter of the cone was measured at the recording site for different application strengths. The resulting values were used to correct the pressure values measured accordingly for all experiments. To determine the flow speed at the pipette tip, the volume emerging over a certain time was measured. The applied pressure amplitudes led to flow speeds at the pipette tip in the range of $0-0.56$ m/s . The dependency of the flow speed on the applied pressure was almost linear, particularly in the most relevant interval of $50-150$ hPa, as can be seen in figure 2.3 (B). Throughout this dissertation the results obtained will always be reported in relation to the pressure amplitudes since these were directly recorded. The stimulus application will be further discussed in section 4.2.3. The stimulation by ejection of Ringer's solution will be referred to as 'puff' in accordance with similar studies performed on ORNs of mice [74, 85].

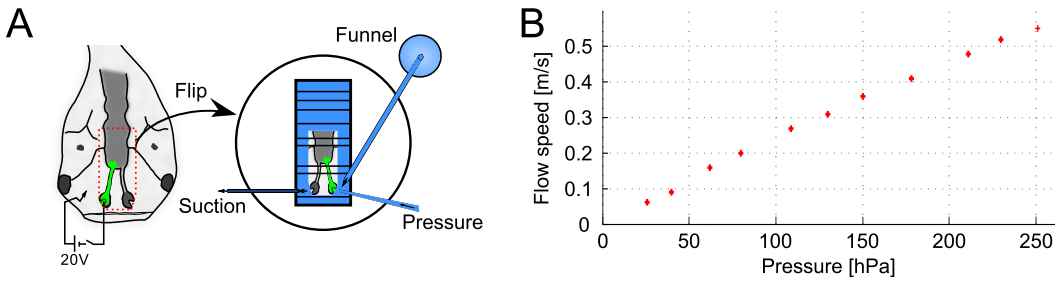


***Figure 2.3*** – ***(A)*** *Sketch of the electroporation procedure resulting in a green staining of ORNs and the olfactory nerve. The area marked with a red dotted line was isolated during the whole mount preparation, flipped and transferred to a recording chamber. Ringer's solution was constantly perfused over the sample via a funnel applicator which was also used for the application of odorants. A glass pipette positioned directly in front of the epithelium was used for stimulation with puffs of Ringer's solution.* ***(B)*** *Plot of the relationship between the applied pressure amplitude for the ejection of Ringer's solution through the pipette tip and the resulting flow speed at the tip.*

## 2.4 Image processing

Images acquired with the line illumination microscope were saved in a custom 16-bit tiff format including the measurement parameters and a measurement description. The files stored up to 6 dimensions, namely lateral $x$ and $y$, axial $z$, time $t$, spectral channel $c$ and — if desired — camera lines $d$. In the normal readout mode $d$ contained only the central line or up to 4 binned camera lines. For offline subtraction imaging or pixel reassignment the last dimension stored up to 30 lines of the camera chip.
Image processing was done with custom-written MATLAB (MathWorks) scripts and ImageJ. The camera background was estimated by taking dark images and the average value was subtracted from each image.
The same image processing steps were performed as described in our previously published papers [41, 44].

### 2.4.1 ΔF/F and response criterion

To display increases in the fluorescence signal $F(t)$ related to calcium concentration increases, $\Delta F/F$ values were displayed:

$$\frac{\Delta F}{F} = \frac{F(t) - F_0}{F_0} \ . \tag{2.8}$$

Here, $F_0$ stands for the average pre-stimulus fluorescence signal over the first $2-4$ seconds of the measurement corresponding to at least 10 data points. The $\Delta F/F$ maps were calculated pixel-by-pixel and low-pass filtered with a small Gaussian (width <2 pixels).
Peak responses for the single amino acid stimulations were determined after filtering the $\Delta F/F$ traces with a moving average filter spanning 5 frames. Subsequently, the maximum value was selected within an interval of 8 seconds after stimulus onset.
For the same measurements a response criterion was used to determine if a certain increase in fluorescent intensity $F(t)$ should be considered a stimulus response:

$$\max_{t_0}^{t_s}(F(t)) < \mathrm{avg}_{t_s}^{t_e}(F(t)) \ . \tag{2.9}$$

A stimulus related response was thus assumed if the maximum intensity in the region of interest during the pre-stimulus interval, $t_0 - t_s$, was smaller than the average

intensity over the interval $t_s - t_e$. The latter interval included the 4 seconds directly following stimulus application.

### 2.4.2 Shift and bleach correction

Corrections for shifts of the preparation and photobleaching of the fluorophores were only applied when necessary. Shift correction was applied in the lateral directions by a MATLAB script[1] as described by Kludt et al. [44]. Briefly, for the consecutive images $f(x, y)$ and $g(x, y)$ the non-normalized cross-correlation function was calculated:

$$c_{f,g}(\Delta x, \Delta y) = \int\int f(x, y) \cdot g(x + \Delta x, y + \Delta y) \mathrm{d}x\mathrm{d}y \ . \tag{2.10}$$

Zero padding was accounted for by multiplying a correction factor. The amount of shift was determined as ($\Delta x$,$\Delta y$) of the cross-correlation's maximum value by Gaussian fitting. The resulting value was used for shift correction via 2D linear interpolation.
Photobleaching was corrected by applying a Legendre low-pass filter as described by Bao et al. [92]. Bleach correction was mainly necessary for long measurements containing multiple stimulations. Whenever peak amplitudes for these responses were to be extracted the longer measurements were split into shorter segments, and $\Delta F/F$ values were computed individually rather than bleach correction of the whole recording. Bleach correction was thus mainly used for data displaying purposes.

### 2.4.3 Activity correlation imaging

Neighborhood correlation maps were used prior to activity correlation imaging (ACI) to facilitate the region of interest selection. The term 'neighborhood correlation map' refers to an image where the intensity of each pixel is determined as the average correlation of its intensity trace with each of its eight neighbors. The map highlights regions exhibiting similar activity, which is usually the case if all pixels belong to the same cell. Pixels predominantly containing noise and not reflecting any intensity changes caused by calcium fluctuations are mostly uncorrelated and consequently assigned low correlation values. This method was earlier described by Manzini et al. [59].

[1] Written by Dr. Mihai Alevra from our institute.

Activity correlation imaging is following the same concept. However, pixel intensity traces are not correlated with their neighbors but instead with a reference trace obtained from a region of interest (ROI). Thus, areas exhibiting similar activity as the selected region of interest are highlighted. The method was described by Junek et al. [3]. Briefly, the cross-correlation between the reference trace $r(t)$ obtained from the selected ROI and each individual pixel is calculated:

$$c_i = \frac{\sum_{n=1}^{N}(v_i(t_n) - \bar{v_i}) \cdot (r(t_n) - \bar{r})}{||v_i(t_n) - \bar{v_i}|| \cdot ||r(t_n) - \bar{r}||} \ . \tag{2.11}$$

The number of recorded timepoints is denoted by $N$ and $v_i(t_n)$ is the intensity of the $i$-th pixel at the time $t_n$. All displayed neighborhood and activity correlation maps were low-pass filtered.

# 3 Results

## 3.1 The line illumination microscope

In this first section of the results chapter the improvements and changes made to the line illumination microscope are described and the potential usage of off-center camera lines is evaluated. The section deals thus with the first goal of the thesis as mentioned in section 1.4.
The existing 2-channel line illumination microscope (LIM) was successfully used for the first experiments of this thesis. However, the direction in which experiments were developing made some changes necessary. As a result, the optical pathway of the microscope changed considerably. Here, the final design of the LIM after the modifications is discussed as it was used for all the experiments presented in this thesis. Afterwards, section 3.1.1 will deal specifically with the modifications and their benefit.

Figure 3.1 shows the optical pathway of the LIM and is described hereafter.

**Excitation Pathway:** Two lasers are available for the excitation of fluorophores at 488 nm and 561 nm with a maximum output power of 200 mW each (Sapphire 488 LP and Sapphire 561 LP, Coherent, USA). Both laser beams travel individually through acousto-optic modulators (AOM, AA.MT110, Pegasus Optik GmbH, Wallenhorst, Germany). The AOMs can be controlled via an analog input signal and modulate the beam intensity. Afterwards, three normal mirrors and one dichroic mirror (zt 488 RDC, AHF Analysetechnik, Tübingen, Germany) project both laser beams onto one single-core glass fiber. A fiber coupler (FiberPort PAFA-X-4-A, Thorlabs, USA) ensures coupling of both beams into the glass fiber (cf. figure 3.1 (A)). Using only one single-core fiber leads to significant losses of laser intensity during the coupling but ensures good alignment after decoupling. Consequently, fewer alignment optics are necessary in the limited space of the microscope frame. The glass fiber ends in

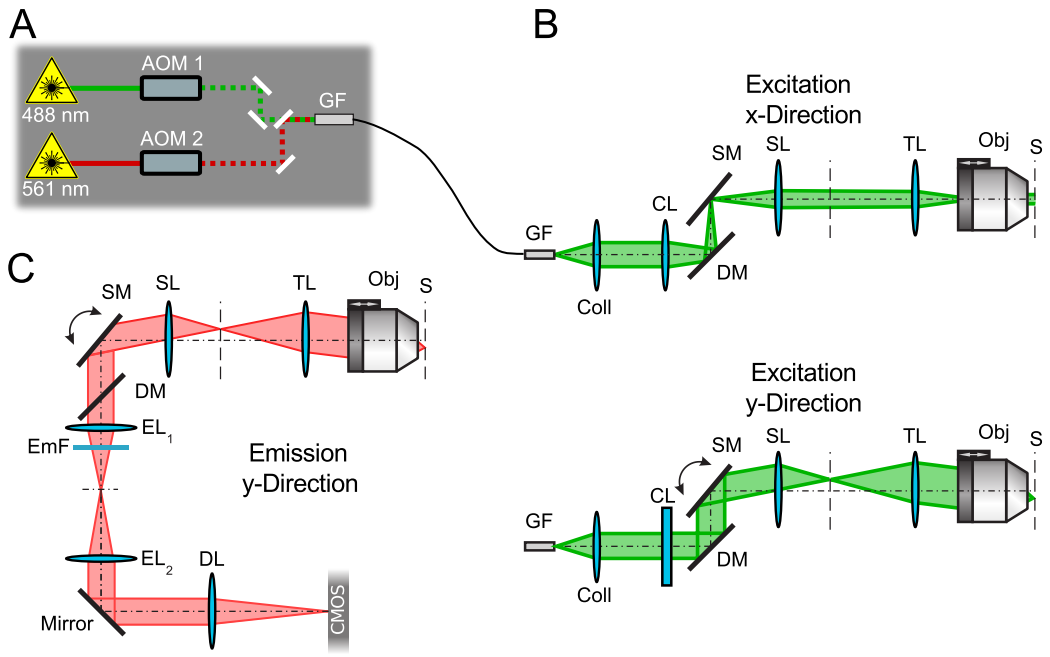


***Figure 3.1*** *– **(A)** Two laser beams are coupled into the same glass fiber (GF). The beam intensities can be modulated individually by acousto-optic modulators (AOM). **(B)** Sketch of the excitation pathway attached to the microscope for the x- and y-direction. **(C)** Emission pathway depicted only for the y-direction. The line is de-scanned and always focused to the same area on the camera chip. Coll, collimator lens. CL, cylindrical lens. DM, dichroic mirror. SM, scan mirror. SL, scan lens. TL, tube lens. Obj, objective. S, sample. EL, emission lens. EmF, emission filter. DL, detector lens.*

---

a box attached directly to the microscope frame which houses the remaining optical components. Attaching most of the optical pathway to the frame makes it possible to move the microscope instead of the sample which in turn can remain fixed over the course of the experiments. The rest of the excitation pathway is similar to the one of the single-channel LIM described by Junek et al. [3] and displayed in figure 3.1 (B) for the x- and y-direction. After decoupling the laser light is collimated with a biconvex collimator lens (Coll, f = 50 mm) creating a beam with approximately 13 mm diameter. Next, a cylindrical lens (CL, f = 40 mm) focuses the beam in one direction thereby creating a line on the scan mirror (SM) to which it is reflected via a dichroic mirror (DM, zt 405/488/561 rpc, Chroma, USA). Behind the scan mirror a scan lens (SL, f = 80 mm) and the tube lens (TL, f = 164.5 mm) focus the line on the backfocal plane of the objective. Accordingly, an excitation line perpendicular

to the one in the backfocal plane is created on the sample over which it can be scanned by rotating the scan mirror.

**Emission pathway:** The emission pathway is depicted in figure 3.1 (C). The emission light is collected by the same objective and passes through tube and scan lens before being deflected by the scan mirror. The deflection of both excitation and emission light at the same scan mirror with the same angle de-scans the emission light, i.e. the final position of the emission line on the detector remains always constant independent from the excitation line. Behind the scan mirror the emission light passes through the dichroic mirror (DM) instead of being reflected like the excitation and is then filtered by two emission filters (EmF) to eliminate remaining excitation components. Following this purification, the emission light travels through two biconvex lenses ($EL_1$, $EL_2$, f = 40 mm). In between these lenses an optical plane is created where a slit can be positioned to serve as a physical confocal aperture. Omission of the pyhsical aperture increases detection efficiency and allows the recording of out-of-focus light. A physical aperture can be useful to uncouple the final magnification on the detector from the size of the confocal aperture. However, for all experiments in this thesis only the camera pixels were used to ensure confocality. A mirror behind the second emission lens projects the emission light into the direction of the camera. The attachment of the camera directly to the mass of the microscope frame reduced the impact of vibrations caused by the fan. A detector lens (DL) focuses the light on the camera chip. The focal length of the detector lens determined the magnification and was typically chosen between 60 mm and 80 mm. The resulting magnification causes the 6.5 µm pixels of the camera chip to cover between 160 nm and 220 nm of the sample for the most frequently used 40x/1.0 objective. The scan mirror movement was adjusted to step sizes covering the same distance and thereby creating square sized pixels in the final image. A 2x2 binning of the pixels on the camera was applied most of the time, resulting in a spatial sampling of about 400 nm for most standard measurements. The 400 nm pixel scale corresponds to 0.68 airy units (AU). Consequently, the omission of a physical aperture was possible since the limited size of the camera pixels worked already as a descent confocal aperture.

The setup is controlled by custom-written software. Two DAQ devices (NI USB 6215, National Instruments, USA) serve for analog and digital input and output con-

trolling the scan mirror, the AOMs, and also the piezo actuator (PIFOC, Physik Instrumente, Palmbach, Germany) used for moving the objective in a range of 100 µm which allows the recording of three dimensional image stacks.

### 3.1.1 Improving imaging performance

Three main changes were made to optimize the 2-channel LIM based on the requirements identified in the first set of experiments. Namely, a different camera model was used, a second excitation laser was implemented into the design, and the separation into two emission channels was changed to an excitation based approach using AOMs. These three changes are described in this section.

**Camera:** Already during the construction of the 2-channel LIM it became evident that the sCMOS camera (Andor Technology, Belfast, UK) would put significant constraints on the setup due to its readout electronics. These were not capable of dealing with the rather special case of single line acquisition necessary for the LIM. Consequently, replacing the camera with a newer sCMOS model (Orca-Flash 4.0, Hamamatsu, Japan) was one of the first steps. A frame grabber card (Radient Framegrabber, Matrox, Canada) and custom-written software were used to enable the desired readout of the camera. The changes resulted in a single line readout speed of approximately 26 kHz which could be maintained indefinitely, limited only by the RAM of the acquisition computer. For comparison, the previously used camera allowed a line readout speed of only 7.6 kHz limited to a measurement duration of less than 12 s. For full frame recordings of 512x1024 pixels the now available frame rate increased from 15 Hz to 50 Hz and can easily reach several hundred Hz for smaller areas. Furthermore, the more flexible and faster readout structure made it possible to collect more camera lines without compromising measurement speed too much - a prerequisite for subtraction imaging and pixel reassignment. Typical line dwell times used throughout the thesis for calcium imaging experiments ranged from $50 - 200$ µs.

**Second Laser:** The early version of the 2-channel LIM comprised only one laser for excitation. Although combinations of calcium-sensitive dyes both excitable at 488 nm like Calcium Green and Fura-Red are available, many others are not usable. For example, even though Rhod-2 is theoretically excitable with 488 nm, the excitation is too inefficient, especially for fast recordings or when a second dye is much

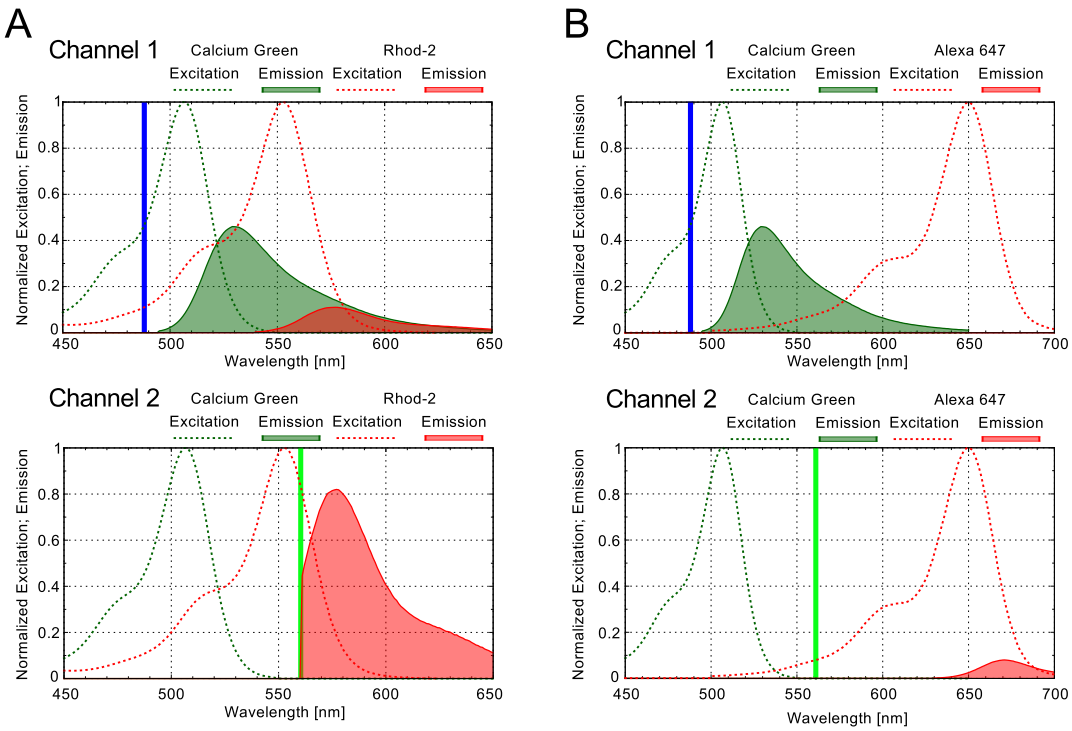


***Figure 3.2*** – ***(A)*** *Spectral data of Calcium Green and Rhod-2 labeling scaled to the corresponding excitation efficiency. Upper image, Channel 1 with 488 nm excitation. Lower image, Channel 2 with 561 nm excitation. A strong overlap in the first channel exists but the second channel contains only the Rhod-2 signal and can be used for cross-talk correction.* ***(B)*** *same as in (A) for the combination of Calcium Green and Alexa Fluor 647. Data was obtained from [93].*

stronger excited at the same time (cf. figure 3.2 (A) upper panel). Even the combination of calcium-sensitive with non-calcium-sensitive dyes was challenging due to strong overlap in the emission spectrum of fluorophores sharing the same excitation wavelength. Hence, a second laser at 561 nm was installed, increasing the range of suitable fluorophores considerably.

**2-channel:** Recording different fluorophores in two channels was realized in the earlier version of the 2-channel LIM by separating the emission light with dichroic mirrors based on wavelength. This allowed for precise separation of fluorophores. Furthermore, since the emission light was split into two lines projected to different areas of the camera, both channels could be recorded in one acquisition. Unfortunately, the detection efficiency was decreased significantly by the additional optical

components, including filters and dichroic mirrors. The possible measurement speed was in most experiments limited by the intensity of the signal whereas technical limitations — particularly with the new camera — played only a minor role. Efficient detection of the emission light without any unnecessary losses is thus crucial for fast scanning applications. The separation method was consequently changed to alternating illumination with the two different lasers. Two AOMs enabled rapid on and off switching of the laser beams. The rising time of the AOMs was with 160 ns/mm (time per mm of beam diameter) significantly smaller than the shortest line dwell time of 40 µs. Normally, the excitation was switched after each full frame acquisition. However, if the simultaneous acquisition of both channels without delay was important for the experiment, the AOMs switched the excitation in between single line recordings limiting the delay to the 40 µs exposure time. The two fluorophores were split into two channels by excitation as shown in figure 3.2 for Calcium Green and Rhod-2 or Alexa Fluor 647. Although the excitation of Alexa Fluor 647 was not optimal, it was well separated and the power of the second laser can be controlled independently to compensate for the lower excitation efficiency. As long as at least one of the two channels collected the pure signal from only one fluorophore, the correction of cross-talk was straight forward. No optical components for separation of the emission light were necessary and the whole emission spectrum of both dyes could always be recorded. In total, two dichroic mirrors and two filters could be removed from the optical pathway. The first channel in the previous design recorded only emission light from 500 nm to 550 nm, for the typical case of Calcium Green. Approximately 37 % of the total emission intensity was thus previously blocked by filters and became available with the excitation based separation [93]. The second channel was limited to wavelengths above 570 nm amounting to approximately 21 % intensity loss for Rhod-2 recordings [93].

### 3.1.2 Evaluation of imaging properties

The faster and more flexible readout with the new sCMOS camera renders the acquisition of additional, off-center camera lines more attractive. Subtraction imaging was already evaluated partly for the earlier version of the 2-channel LIM. It improved optical sectioning and image contrast [23]. Since the LIM changed considerably, a reevaluation was necessary. Furthermore, while subtraction imaging provides increased optical sectioning it is also increasing the noise of an image [94]. Pixel reassignment, on the other hand, is used to gain better resolution mainly in the lateral

direction and a significantly increased signal to noise ratio [25, 26]. The downside of pixel reassignment is a reduced optical sectioning capability as compared to the single line readout due to the larger confocal aperture. For pixel reassignment the lines directly adjacent to the central line are used. For subtraction imaging lines at the border of the active sensor area are important. It is hence possible to combine both methods. Both methods and their combination are evaluated in this section of the thesis.

### Lateral Resolution

Pixel reassignment has beneficial effects for point scanning systems on the lateral resolution due to higher peak intensities and sharper point spread functions [25, 26]. Line scanning allows for pixel reassignment in the direction perpendicular to the line only.
Lateral and axial resolution of the LIM with and without pixel reassignment were determined by measuring the FWHM through the main axes of small beads (cf. section 2.1.3). Figure 3.3 displays the results for measurements with a 40x/0.8 objective and a 60 mm detector lens. The central line corresponded to a confocal aperture of 0.27 AU. Furthermore, a 63x/1.0 objective was used, corresponding to 0.17 AU for the central line. Figure 3.3 (A) shows the average intensity profile after pixel reassignment of 7 measured beads through the main axes of the beads. The axial direction was scanned in 50 nm steps. The solid lines show fitted Gaussian curves. Clearly, the scanning direction (y) perpendicular to the line is much better resolved than the x-direction, a typical phenomenon in line scanning microscopy [95, 96]. The y-resolution was further improved by pixel reassignment as can be seen in figure 3.3 (B) where the intensity profile gained by simple summation of 5 camera lines (1.35 AU) is compared with the pixel reassignment method using the same 5 camera lines. Clearly, the reassignment shows a narrower profile. The table 3.1 lists the FWHM values obtained from the 7 measured beads for the 40x objective and for 8 beads measured with the 63x objective. All beads were fitted individually and the obtained FWHM values were averaged. Values for the confocal imaging with only the central line, the simple summation and the pixel reassignment are listed. Figure 3.3 (C) shows the data for comparison as a plot. The optimal resolution is achieved when measured with the central line. However, 0.27 AU and

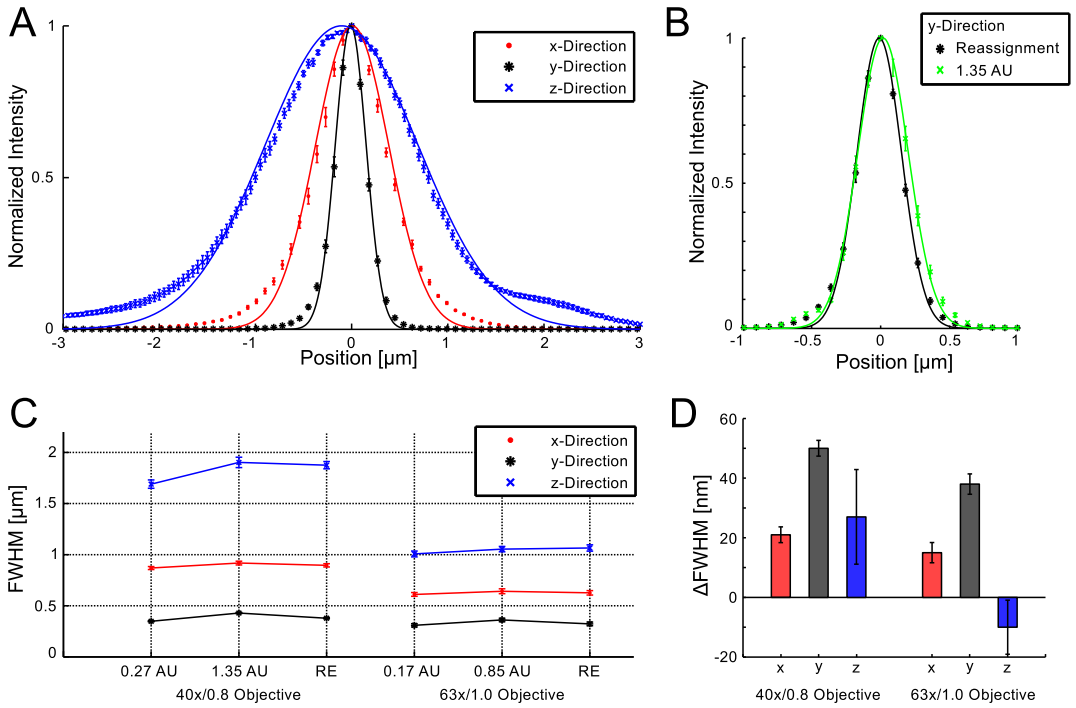


***Figure 3.3*** – ***(A)*** *Average intensity profile through the central pixel of fluorescent beads ($n = 7$, 170 nm bead diameter) along the lateral and axial dimensions after pixel reassignment. 40x/0.8 objective.* ***(B)*** *Same as in (A) for the direction perpendicular to the excitation line. In addition to the reassignment case, the profile is also shown for the same confocal aperture of 1.35 AU without reassignment.* ***(C)*** *Average FWHM values of 7 beads for the 40x objective and 8 beads for the 63x objective. The FWHM for a small confocal aperture, a medium confocal aperture and the reassignment case (RE) with the same confocal aperture as the medium case are shown.* ***(D)*** *Average difference of the FWHM between the normal summation and the pixel reassignment both corresponding to a medium confocal aperture. Error bars: SEM.*

---

0.17 AU respectively were for most measurements too small to yield a sufficient signal strength. Binning more lines and thus reaching confocal apertures of 1.35 AU and 0.85 AU for the two objectives deteriorates the resolution, some of which can be restored by using pixel reassignment instead of the simple summation. Figure 3.3 (D) shows the improvement in FWHM gained by pixel reassignment as compared to simple summation of an equal amount of camera lines. The lateral resolution in scanning direction is significantly enhanced for both objectives, for example by 50 nm corresponding to a 11.6 % gain for the 40x objective. Even the direction along the line benefits owed to the higher peak intensity reached by reassignment. The axial direction shows a large SEM and only small changes — e.g. a relative

change of only 1 % for the 40x objective — considering that the axial resolution is several times bigger than the lateral resolution. This is to be expected, reassignment should not have an effect on the axial direction since the confocal aperture remains the same and the lines are only shifted laterally.

| | | Full width half maximum [nm] | | |
|---|---|---|---|---|
| **Objective** | **Dimension** | **Central Line** | **Summation** | **Reassignment** |
| 40x, 0.8 NA | x | 870(10) | 920(20) | 900(20) |
| | y | 350(10) | 430(10) | 380(10) |
| | z | 1690(40) | 1900(50) | 1880(40) |
| 63x, 1.0 NA | x | 610(20) | 640(20) | 630(20) |
| | y | 300(20) | 360(20) | 320(20) |
| | z | 1000(30) | 1050(30) | 1070(30) |

***Table 3.1*** *– Full width half maximum for the two objectives and the three different reconstruction methods. Error, SEM.*

### Optical Sectioning

Subtraction imaging can improve the optical sectioning capability for line scanning microscopes as was shown by Poher et al. [29]. Here, the improvement was evaluated with a thin fluorescent layer (cf. section 2.1.3). Figure 3.4 shows the results of these measurements for the 40x/0.8 objective. In figure 3.4 (A) the axial intensity profile of a scan through the fluorescent layer is shown for the central line readout (0.27 AU) and the summation of 5 lines (1.35 AU). Summation and pixel reassignment are equivalent for the case of a uniformly stained thin layer. The central line recording performs slightly better in blocking out-of-focus light. The figure 3.4 (B) shows the average intensity profile for the same measurement obtained from two off-center lines close to the border of the active sensor area. The shape of both profiles in (A) and (B) can be explained with the sketch in figure 3.4 (C). The upper sketch in (C) depicts the direct excitation of the thin layer. The thin layer is at the focal plane corresponding to the position at 0 µm in (A) and (B). Strong in-focus emission light (solid green line) is generated which is focused mainly on the central line of the detector causing the high peak at 0 µm in (A). Since the layer is thin, almost no out-of-focus light is generated in this situation, explaining the almost zero value in panel (B) at 0 µm. On the other hand, in the lower sketch of (C), at a position of 5 µm axial, the excitation beam is focused to a spot in front of the thin layer. Accordingly,

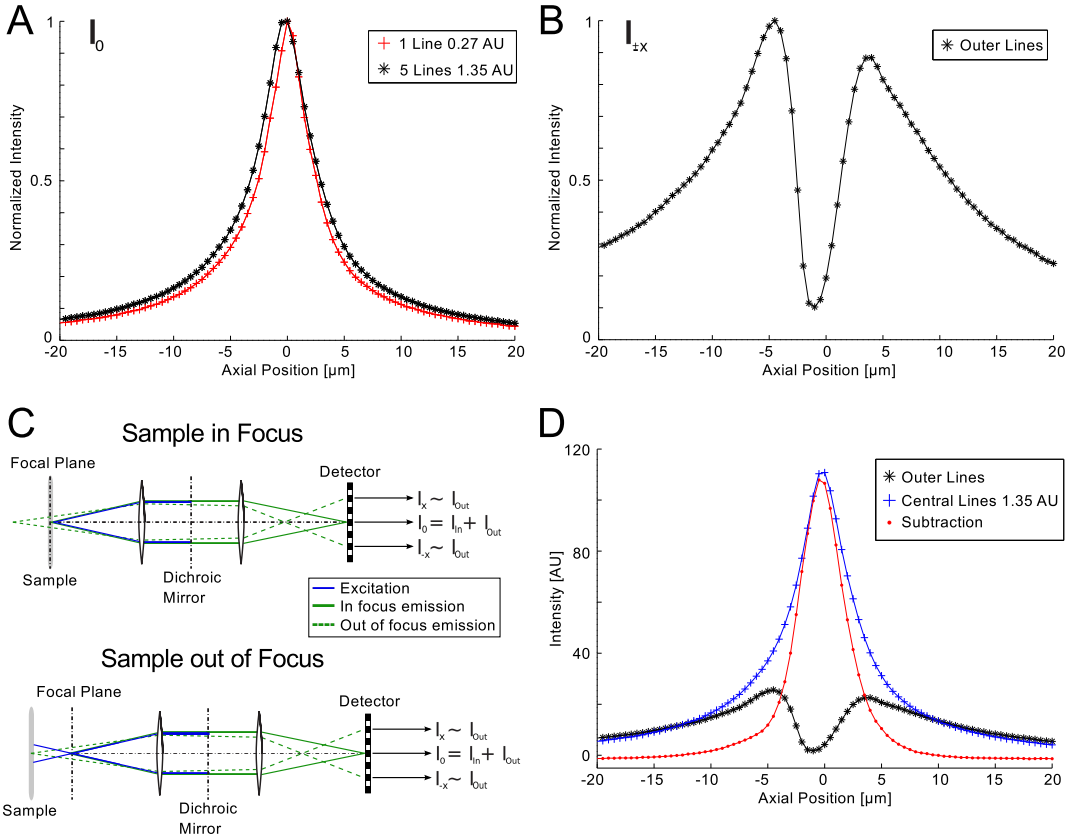


***Figure 3.4*** – ***(A)*** *Normalized intensity for a scan through a thin layer of Fluorescein. The intensities for readout of only 1 line on the camera and for the sum of 5 lines corresponding to 0.27 AU and 1.35 AU, respectively are displayed.* ***(B)*** *Data from the same measurement as in (A) for the readout of the off-center lines.* ***(C)*** *Sketch of the in-focus and out-of-focus light distribution over the detector. The upper image depicts the thin layer in focus corresponding to an axial position of 0 µm in (A) and (B). The lower image corresponds to a measurement were the sample is out-of-focus for example at axial position 5 µm in (A) and (B).* ***(D)*** *Intensity of the central lines and the outer lines for the same measurement as in (A) and (B) without normalization. In addition, the result of subtracting the off-center lines from the central line is plotted.*

the layer is hit by an expanded excitation laser beam causing the emission of out-of-focus light. Since the out-of-focus light (dashed green lines) is not focused directly to the detector, it hits a larger number of pixels. Consequently, both the central line (A) as well as the off-center lines (B) have non-zero intensity values. Subtracting the outer lines from the central line reduces the out-of-focus component in the resulting subtraction image as depicted in figure 3.4 (D). Note that in contrast to (D), (A) and (B) show normalized intensity values. In a thicker sample the intensity recorded by the off-center lines will not drop to zero at the 0 µm axial position since they

are hit by out-of-focus light from other layers. The thin-layer case illustrates the idea particularly well, however, the concept and benefit remains the same for thicker samples. The out-of-focus reduction causes a narrower intensity profile along the axial direction as can be seen in figure 3.4 (D).

### Signal-to-Noise Ratio

After the positive effects of pixel reassignment on lateral resolution and of subtraction imaging on optical sectioning have been established, the impact on the signal-to-noise ratio was evaluated. A labeled bead with a strong background generated by a surrounding Fluorescein solution is measured (cf. section 2.1.3).

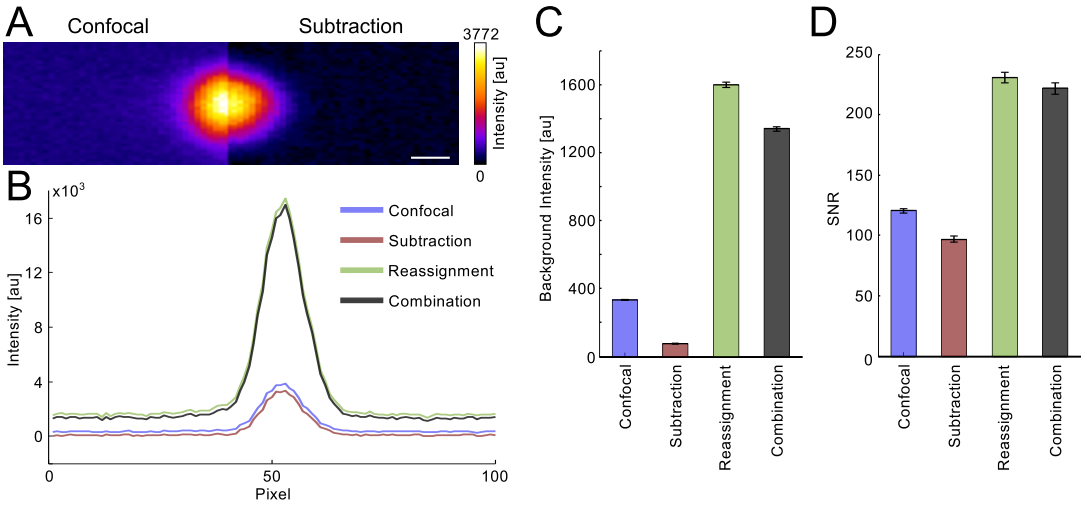


***Figure 3.5*** *– **(A)** Image of a labeled bead immersed in a 2 µg/µl solution of Fluorescein. Left side, normal recording from the central camera line. Right side, same recording after subtraction imaging. Scale bar, 1 µm. **(B)** Intensity profile through the bead from the measurement in (A). All data was taken from the same measurement with different reconstruction methods. **(C)** Background intensity for the different reconstruction methods averaged over 19 bead images. **(D)** Signal-to-noise ratio (SNR) averaged over 19 bead images. Error bars, STD.*

---

Figure 3.5 depicts the results for normal confocal readout (central line, 0.27 AU), subtraction imaging, pixel reassignment (1.37 AU) and the combination of subtraction imaging and pixel reassignment. Panel 3.5 (A) shows a scan of the bead and the surrounding solution. The left side corresponds to a normal central line recording and the right side to the same recording after application of subtraction imaging. Clearly, the background in the subtraction part of the image is lower. A closer

evaluation reveals, however, an increased background variation. Panel (B) shows the intensity along a horizontal line through the center of the bead. The signal after pixel reassignment is higher for the bead and for the background. Subtraction imaging can reduce the background intensity if applied to the central line alone or in combination with subtraction imaging. The bar plot depicted in panel (C) quantifies the averaged background intensity (n = 19 bead images) for the different methods. Background intensity increases naturally with the larger confocal aperture of pixel reassignment. The increase can be partly undone by combining it with subtraction imaging. Interesting in particular is the signal-to-noise ratio (SNR) plotted in panel (D). Subtraction imaging leads to a reduced signal-to-noise ratio. This is explainable by the reduction of intensity over the whole image and the noise from the readout electronics of each pixel which adds up if data from additional lines is subtracted. Reassignment improves the SNR considerably even if combined with subtraction imaging.

In conclusion, subtraction imaging and pixel reassignment broaden the usability of the LIM. Both methods can be applied relatively easy and both are useful for certain types of experiments. Subtraction imaging should be applied when precise optical sectioning is needed while SNR is less important or long exposure times can be used. Pixel reassignment can provide much higher SNRs and thus faster imaging or lower laser intensities are feasible while compromising the resolution less than the simple binning of camera pixels would. Both methods can be combined generating images with good SNR and a reduced background. They can be selected after the acquisition of images and can be individually combined. Subtraction imaging was regularly used to facilitate precise region of interest selection and for the measurements in section 3.2.5 and 3.3.2. Pixel reassignment was implemented parallel to the calcium imaging experiments of the following chapters and was used only for preliminary experiments and the results reported in section 3.3.3.

## 3.2 The small cluster

The line illumination microscope evaluated in the previous chapter was used for all recordings throughout the next sections. The increased acquisition speed and detection efficiency were used to perform calcium imaging on volumes.
The current chapter is dedicated to the second goal mentioned in section 1.4.

Namely, we aimed at evaluating the function and properties of the small cluster and at contributing to the ongoing research effort about additional modalities like temperature and mechanical simulations registered in the olfactory system.

The small cluster has been introduced in section 1.2.3. Subsequently, its two most prominent glomeruli, the $\beta$- and $\gamma$-glomerulus, were examined. Both structures are particularly interesting because they add information about two new stimulus qualities.

The temperature-related findings reported in section 3.2.2 of this chapter have been published in our paper [44]. The remaining results related to the $\beta$-glomerulus are part of a second submitted manuscript [97].

### 3.2.1 Stimulus space of the small cluster

Firstly, the stimulus space for the $\beta$- and $\gamma$-glomerulus was investigated. Time series of 60-µm-thick volumes separated into 6 layers were carried out with a stack rate of 2 Hz. The field of view (225 µm x 350 µm x 60 µm) covered most of the ventral olfactory bulb including the lateral, medial, intermediate and small cluster. Figure 3.6 shows an example of these recordings for two different animals; a younger (stage 51-53) and an older one (stage 54-56). The basal fluorescence of the Calcium Green stained ORN axons is shown in green while the overlay indicates the maximal $\Delta F/F$ response to various stimuli. Gliem et at. [65] observed responses to amino acids mainly in the lateral cluster while forskolin, an activator of the cAMP-pathway, triggered responses in the medial cluster. This general spatial response pattern was likewise observed in our experiments (cf. figure 3.6).

The $\gamma$-glomerulus was activated by stimulation of the OE with cold Ringer's solution leading to a temperature drop of about 1 °C at the mucosa. Interestingly, none of the other tested stimuli activated the $\gamma$-glomerulus. These observations are in line with previous findings by Eugen Kludt [43]. Note that the responses to cold Ringer's solution were limited to the $\gamma$-glomerulus and fibers innervating it. Temperature increases did not elicit any $[Ca^{2+}]$ changes.

The $\beta$-glomerulus showed a broader response spectrum and was activated by (i) the amino acid mixture (200 µM), (ii) forskolin (25 µM) and (iii) puffs with Ringer's

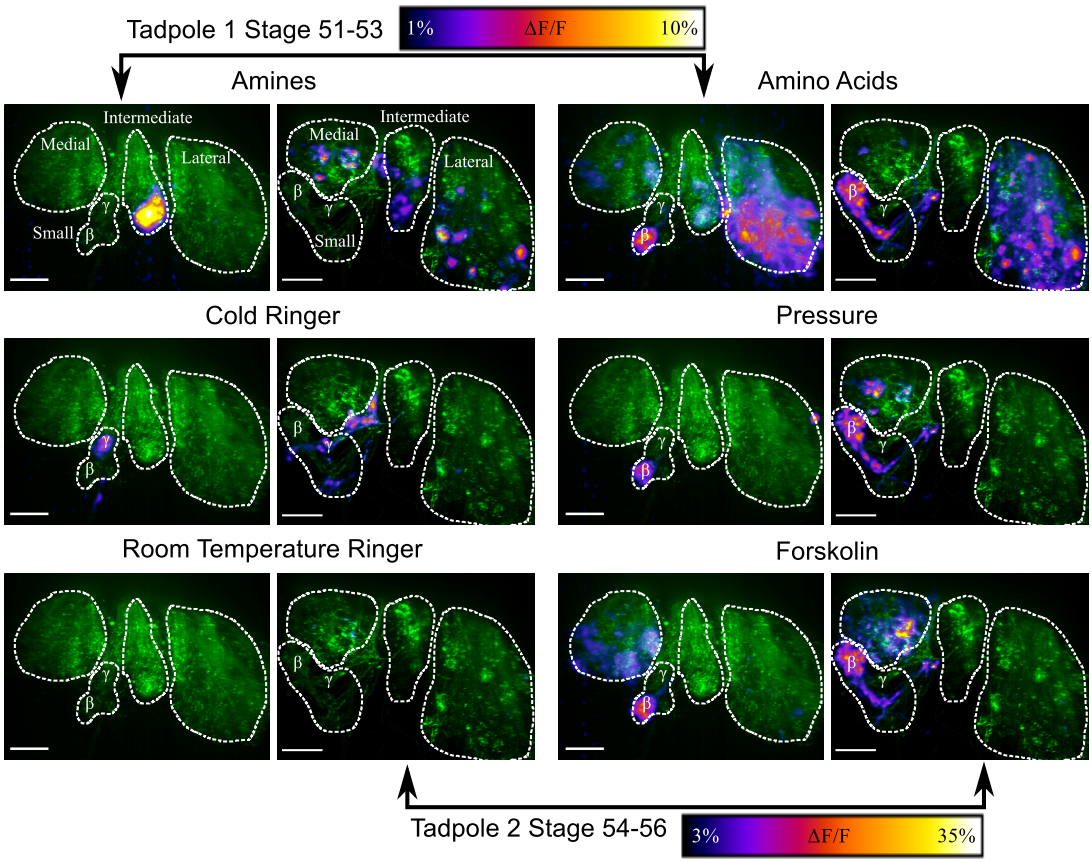


***Figure 3.6*** – *Peak $\Delta F/F$ response to 5 different stimuli and the control with Ringer's solution overlayed to the basal intensity level of Calcium Green electroporated ORNs at the OB for two different animals. The medial, lateral and intermediate cluster are visible as well as the small cluster containing the $\beta$-glomerulus ($\beta$) and the $\gamma$-glomerulus ($\gamma$). Images are maximum intensity projections of a 60-µm-thick volume. Scale bar, 50 µm.*

---

solution (150 - 200 hPa) delivered to the OE. The observed sensitivities are in line with previous findings [43]. Like the temperature stimulation, the mechanical stimulation of the OE led to locally restricted responses in the OB. Only the $\beta$-glomerulus was activated. Occasionally, additional responses in the medial cluster were observed but only for the higher amplitude range of delivered pressure pulses ($>$ 150 hPa). Some of these responses likely belonged to axons passing through the medial cluster and innervating the $\beta$-glomerulus. The $\beta$-glomerulus was the only structure which responded consistently to Ringer's solution puffs in different preparations. The control experiment with room temperature odor-free Ringer's solution did not trigger any $[Ca^{2+}]$ increases in the OB.

Normally, ORNs activated by amino acids do not show responses to the cAMP-pathway activator forskolin [52]. The combination of amino acid sensitivity and activity triggered by forskolin stimulation observed in the $\beta$-glomerulus is thus exceptional. Figure 3.6 illustrates this observation: the $\beta$-glomerulus is in both animals the only region responding to both amino acids and forskolin. Additional experiments were performed to determine whether stimuli involving the cAMP-pathway also activate the $\beta$-glomerulus. However, no responses were observed for the mixture of amines (n = 5), cold Ringer's solution (n = 4), mixture of alcohols (n = 4), bile acids (n = 4) or for a Ringer's solution with decreased pH of 7.5 (n = 5).

Overall, the two investigated glomeruli in the small cluster respond to an unusual range of stimuli. While the $\gamma$-glomerulus only reacts to temperature drops (cf. figure 3.6) with no direct connection to the chemical sensitivity of the olfactory system, the $\beta$-glomerulus combines sensitivity to mechanical stimulation with sensitivity to amino acids — a common stimulus for the olfactory system of *Xenopus laevis* tadpoles.

### 3.2.2 Temperature sensitivity as part of the olfactory system

In section 1.3.2, the previously obtained data on temperature-sensitivity, such as the dose-response curve and the bilateral innervation, was introduced. It was already established that axons terminating in the $\gamma$-glomerulus emerge from ORNs in the OE and that the activity caused by temperature drops is in fact transmitted to M/T cells. However, the following question remained: does the olfactory bulb combine sensitivity to chemicals and the temperature-related responses of the small cluster? The experiments described in this section were aimed at evaluating whether thermo- and chemosensitivity are processed in shared cellular networks.

Electroporating olfactory receptor neurons resulted in a fine staining of axons and the glomeruli which they innervated, as can be seen in figure 3.7 (A). The small cluster is distinguishable due to its position caudally of most other glomeruli. Single axons were particularly well resolved in this region as illustrated in figure 3.7 (B). The stimulation with cold Ringer's solution showed that the evoked responses were limited to the $\gamma$-glomerulus and the fibers innervating it, as observed in the previous section. Neighboring glomeruli showed no responses to the stimulation

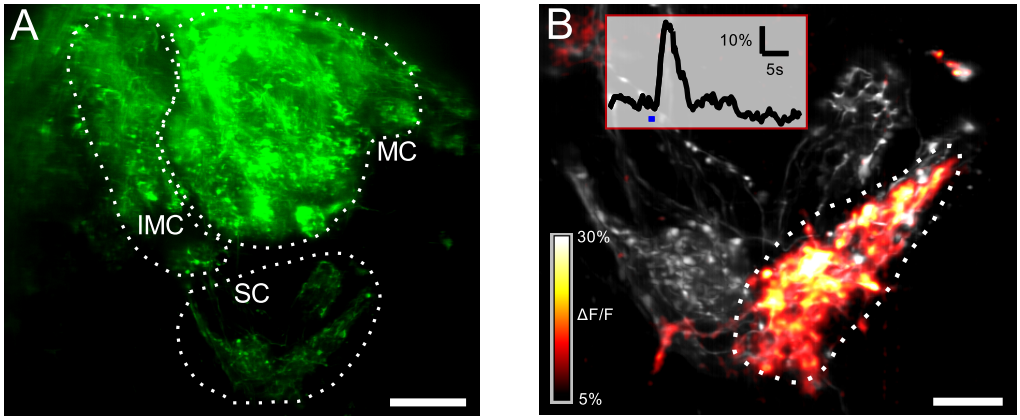


***Figure 3.7*** – ***(A)*** *Basal fluorescence of Calcium Green stained glomeruli. The field of view includes the intermediate cluster (IMC) the medial cluster (MC) and the small cluster (SC). Maximum intensity projection, 100-µm-thick volume. Scale bar, 50 µm.* ***(B)*** *Magnified version of the small cluster with the $\Delta F/F$ peak response to stimulation with cold Ringer's solution as an overlay. The inset shows the $\Delta F/F$ trace for the encircled region of interest. The $\gamma$-glomerulus is clearly identifiable as the responding region. Maximum intensity projection, 12-µm-thick volume. Scale bar, 20 µm. Image modified from our paper [41].*

(figure 3.7 (B)). Since temperature drops are the only established stimulus for the $\gamma$-glomerulus, the presynaptic side of the OB does not provide any indications for a combined processing of thermo- and chemosensitivity.

Analyzing the processing of temperature information in the second-order neurons is more challenging since bolus loading (cf. section 2.2.3) results in a denser staining, causing a reduced contrast. This is demonstrated in figure 3.8 where panel (A) shows the axons stained by electroporation with Alexa Fluor 647, and panel (B) shows the same area in the second channel where M/T cells and their dendrites were stained through bolus loading with Fluo-8 AM. The contrast is reduced, as compared to the presynaptic staining, for two main reasons. Firstly, the density of stained cells is higher because M/T cell somata as well as dendrites are stained. In contrast, on the presynaptic side only the axons are visible with the somata located far away in the epithelium. The amount of out-of-focus light contributing to the second channel is thus much higher. Secondly, the direct application of fluorophores into the tissue during bolus loading causes a higher background staining of the OB's surface for example.

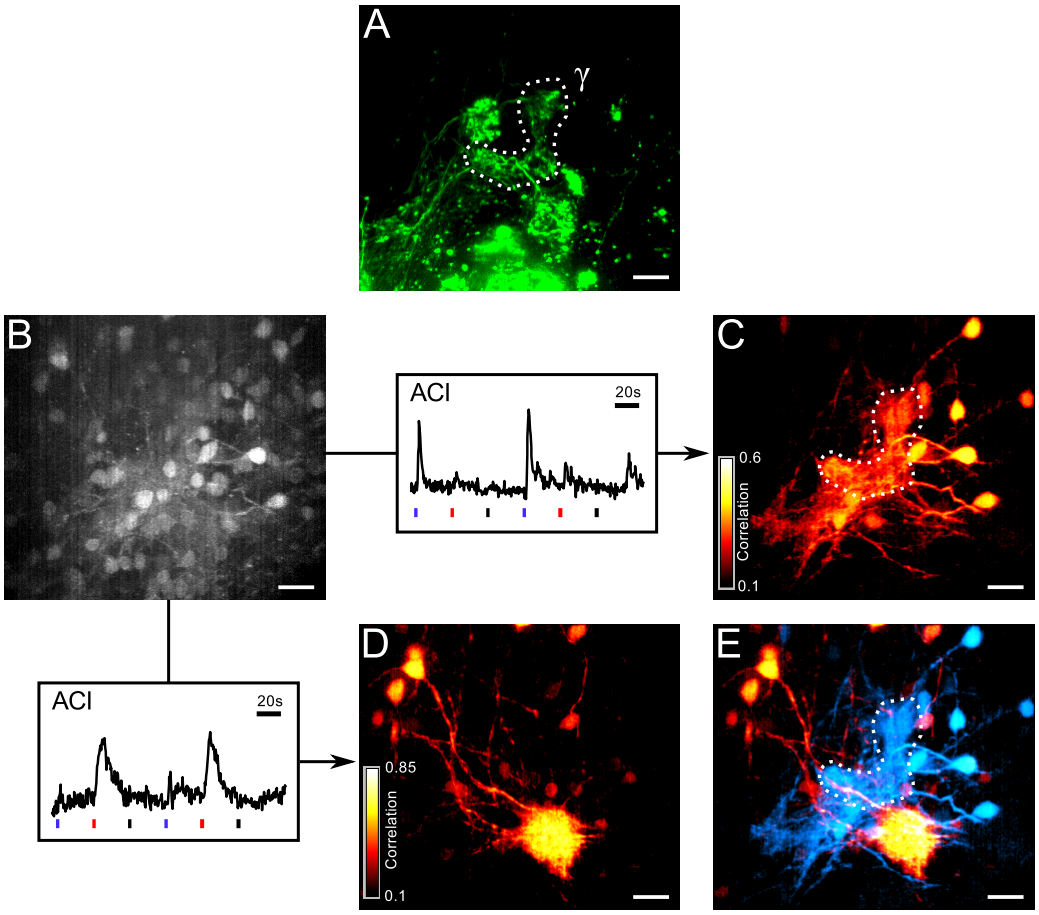


***Figure 3.8*** – ***(A)*** *Alexa Fluor 647 stained ORNs, the dotted line highlights the γ-glomerulus (γ).* ***(B)*** *Same region as in (A) in the second channel showing the basal fluorescence of Fluo-8 AM after bolus loading.* ***(C)*** *Using the displayed, normalized activity trace of a region responding to cold Ringer's solution for ACI results in a high contrast image highlighting all areas responding to temperature drops.* ***(D)*** *Second ACI map corresponding to the displayed, normalized activity trace with responses to L-histidine.* ***(E)*** *Overlay of the two ACI maps. The γ-glomerulus and connected M/T cells are clearly visible and can be easily distinguished from the L-histidine responsive cells. All images, maximum intensity projections of a 28-µm-thick volume. Scale bar, 20 µm. The bars below the traces depict stimulus application. Blue, red and black correspond to stimulation with cold Ringer's solution, L-histidine and room temperature Ringer's solution, respectively. Image modified from our paper [41].*

---

Fortunately, activity correlation imaging (cf. section 2.4.3) can be used to generate contrast based on activity monitored by calcium sensitive dyes. Figure 3.8 displays data from a time recording of a 28-µm-thick volume recorded in 14 layers and with a frame rate of 31 Hz. Over the course of the measurement the OE was stimulated

twice with cold Ringer's solution (cold, $\Delta T = -1$ °C), L-histidine (his, 10 µM) and room temperature Ringer's solution (control). The resulting responses were used as reference traces for the activity correlation imaging. Panel (C) shows the ACI map calculated with the indicated reference trace. The trace was obtained from a region of interest reacting only to cold Ringer's solution. The same is shown in panel (D) for a reference trace where the response was limited to stimulation with L-histidine. Panel (E) finally shows the overlay of the two calculated ACI maps. Consequently, ACI does not only help to generate contrast but can also be used to link M/T cells to their respective glomeruli based on their activation patterns. Figure 3.8 shows some M/T cells with dendrites connected to the $\gamma$-glomerulus and others which are innervating an L-histidine-sensitive glomerulus.

We combined a presynaptic staining with Alexa Fluor dyes to identify the location of the $\gamma$-glomerulus, the subsequent staining of M/T cells via bolus loading with Fluo-8 AM, and the ACI-based analysis of the obtained data. Together these techniques were used to investigate whether dual-sensitive M/T cells, i.e. M/T cells activated by both temperature drops and chemical stimuli, exist. After successful bolus loading and identification of the $\gamma$-glomerulus, 3D time series with 9 layers covering 36 µm and a frame rate of 26 Hz were performed. During the measurement, multiple applications of either cold Ringer's solution or the single amino acid L-histidine were delivered to the OE as stimulation. Figure 3.9 shows the result of such a measurement where the following stimulus sequence was used: cold, cold, his, cold. Panel 3.9 (A) shows 8 $\Delta$F/F traces obtained from M/T cell somata in one measurement. Blue bars under the traces indicate the application of cold Ringer's solution and the red bar, the application of L-histidine. The traces on the left belong to M/T cells responding only to cold Ringer's solution. The traces on the right side show responses only to L-histidine and belong thus to purely chemosensitive M/T cells. In between traces of M/T cells responding to both, L-histidine and temperature drops, are shown. Some of these responded predominantly to temperature drops others predominantly to the stimulation with L-histidine. Consequently, dual-sensitive M/T cells do not only exist but are in fact differentially tuned to temperature and odorants.

Figure 3.9 (B) shows the result of a representative measurement performed as described above. In the first image $B_{(I)}$ the electroporated axons are shown and

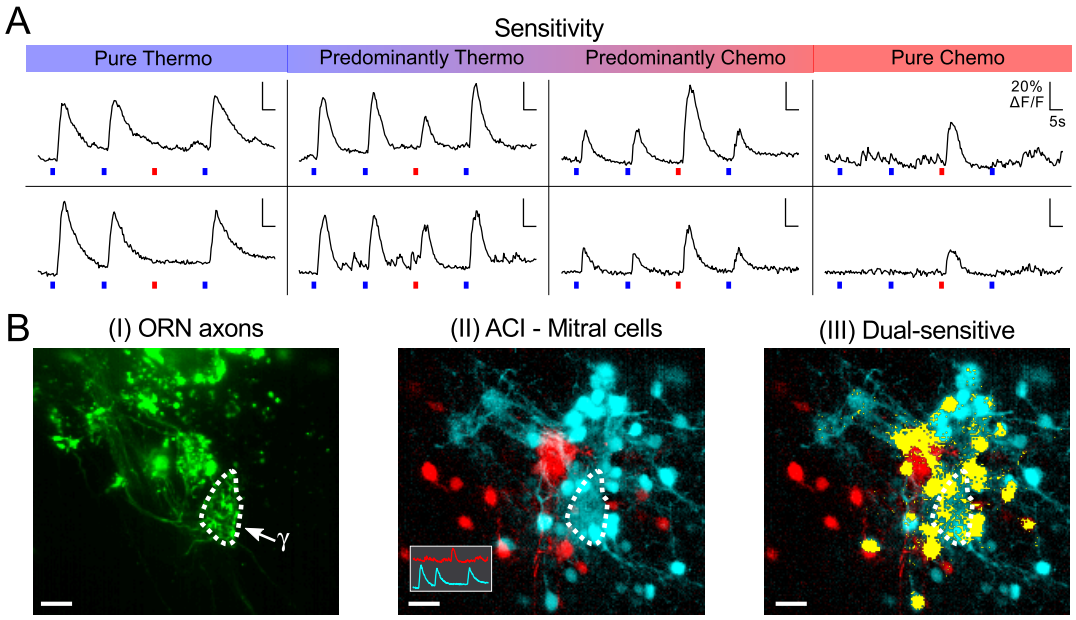


***Figure 3.9*** – ***(A)*** *$\Delta F/F$ traces for 8 different M/T cells from the same measurement. Red bars under the traces indicate L-histidine stimulus release, blue bars indicate a stimulation with cold Ringer's solution. The responses of the M/T cells vary from pure thermosensitivity over different degrees of dual sensitivity to pure chemo-sensitivity as indicated above the traces.* ***(B)*** *The first image (I) shows Alexa Fluor-stained ORNs and the $\gamma$-glomerulus ($\gamma$) is indicated. The second image (II) shows two overlayed ACI maps for the same area as in (I) corresponding to the two reference traces shown as an inset. The cyan trace represents only responses to cold Ringer's solution while the red trace shows only L-histidine induced reactions. The M/T cells were stained with Fluo-8 AM via bolus loading. In the last image (III) all dual-sensitive areas are indicated in yellow. Maximum intensity projection, 36-µm-thick volume. Scale bar, 20 µm. Image modified from our paper [44].*

---

the $\gamma$-glomerulus is indicated. The second image $B_{(II)}$ shows the ACI-map for the two reference traces indicated as an inset. One of the traces was obtained from a purely L-histidine-sensitive area (red). The second one was obtained from a purely temperature-sensitive region (cyan). Black indicates areas with low correlation values ($<0.15$) for both traces, whereas all red areas show a higher correlation to the L-histidine trace than compared to the temperature trace and vice versa for cyan colored areas. The last image $B_{(III)}$ highlights all dual-sensitive areas responding to both, the stimulation with cold Ringer's solution and to the L-histidine stimulation. The dual sensitivity was determined on a pixel-by-pixel basis and according to the response criterion defined in section 2.4.1. A given pixel was marked yellow

as dual-sensitive only if the criterion was fulfilled for both stimuli[1].
In total, 7 experiments in different animals were performed, of which 5 revealed the presence of dual-sensitive M/T cells. These experiments were well suited to prove the existence of dual-sensitive M/T cells as well as their differential tuning. Furthermore, the dendrites of many M/T cells innervating the $\gamma$-glomerulus were visible indicating the direct transmission of temperature information. However, the experiment with its time consuming staining procedures and its limited number of stained cells was less well suited to be performed on a larger scale. Therefore, Camille Okom performed a complementary set of experiments to determine the amount of dual-sensitive cells. Bath incubated slices were used instead of whole-mount preparations and large amounts of M/T cells were successfully stained and screened. For the measurements a larger field of view (366 µm x 450 µm x 40 µm) was used. As a result, a total of 183 responsive M/T cells in 9 animals were scanned. Of these, 151 responded to a mixture of amino acids, another 13 were only temperature-sensitive and 19 (59 % of all temperature-sensitive cells) showed sensitivity to amino acids and temperature drops. Compared to figure 3.9 the number of recorded temperature-sensitive M/T cells seems relatively low, which is most probably explained by the fact that the measured area in the slice experiments was not as well centered on the $\gamma$-glomerulus as in the whole mount experiments due to the lack of a presynaptic staining for orientation.

The results described in this section showed that chemo- and thermosensitivity are processed in shared cellular networks. The temperature sensitivity of the $\gamma$-glomerulus is thus directly linked to odor processing.

### 3.2.3 Pressure pulses delivered to the OE are registered by the $\beta$-glomerulus

Stimulating the olfactory epithelium with puffs of Ringer's solution (cf. section 2.3.3) resulted in responses restricted to the $\beta$-glomerulus in the small cluster. A general sensitivity to Ringer's solution puffs of ORNs was expected because such findings have been made in mice for a large number of ORNs [74, 85]. Besides, a compensation of flow changes which can influence the binding probability of odorants to ORs seems reasonable (compare section 4.2.3 for discussion). A sensitivity limited

[1]The data from the experiment can be watched as a movie at `http://www.jneurosci.org/content/35/20/7892.short` .

to only one glomerulus in the OB hints, however, at a more sophisticated sensor for pressure or flow rates potentially used as an independent input modality. Consequently, it seems worthwhile to investigate the properties of this structure further.

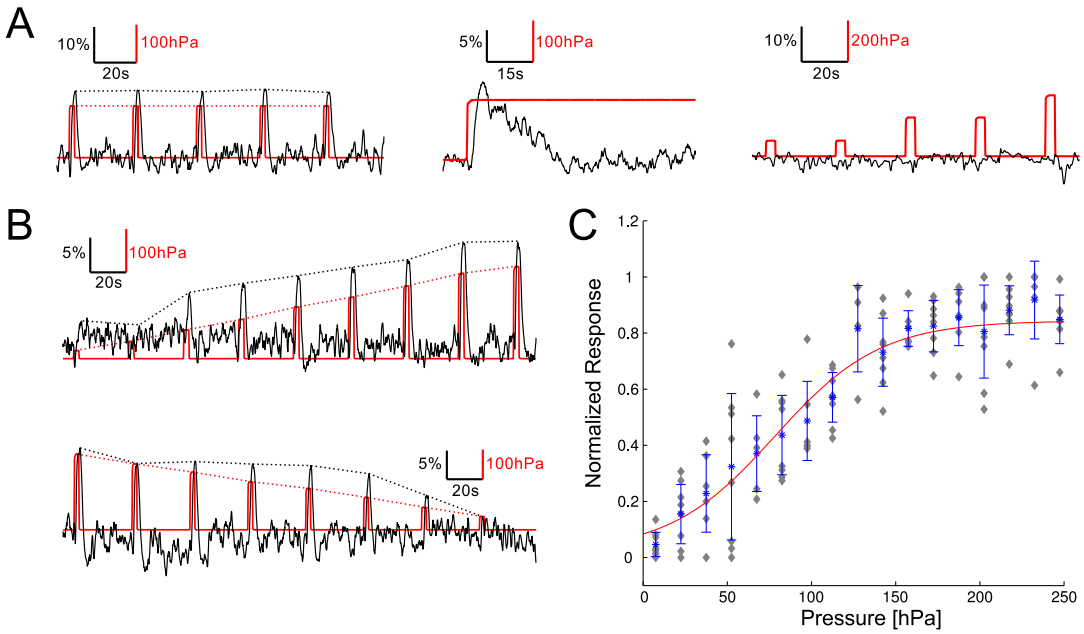


***Figure 3.10*** – ***(A)*** *$\Delta F/F$ traces (black) in response to puffs delivered with a certain pressure (red). From left to right: response of the $\beta$-glomerulus to repeated puffs of constant pressure amplitude (left), response of the $\beta$-glomerulus to long lasting application (middle) and response to pressure pulses in the range of 50-250 hPa in the lateral cluster (right). The dotted lines connect maximum values to facilitate comparison.* ***(B)*** *Representative $\Delta F/F$ traces of the $\beta$-glomerulus in response to 9 consecutive pressure pulses of increasing or decreasing strength.* ***(C)*** *Dose response curve for the response of the $\beta$-glomerulus to stimulation with pressure puffs. Blue asterisks are average values of all measurements ($n = 8$ animals). Error bars, STD. Gray diamonds represent the average values for each animal individually. A sigmoidal has been fitted to the mean values and is depicted as a red line. Image modified from [97].*

---

Time series were obtained for the $\beta$-glomerulus stained via electroporation with Calcium Green. Since puffs with Ringer's solution can be delivered very precisely and no wash-out is necessary, as it is with chemical stimuli, it was possible to take longer recordings with multiple stimulations in the same measurement. Multiple stimuli in one recording facilitate response comparison and yield more data points than single recordings. However, adaptation might play a role if the interstimulus

interval is too short. This possible effect was evaluated by applying a sequence of pressure puffs with the same amplitude and an interstimulus interval of 30 s. Figure 3.10 (A), left image, shows an example of such a measurement. The black trace corresponds to the $\Delta F/F$ response of the $\beta$-glomerulus and the red trace indicates the strength and timing of the delivered puffs. The response amplitude of the $\beta$-glomerulus was very similar over subsequent puffs and showed no decrease as outlined by the dotted black line. Furthermore, the repeatability of responses was regularly tested in between measurement.
Next, the response of the $\beta$-glomerulus to prolonged puffs of Ringer's solution was tested. An example of such a measurement is depicted in figure 3.10 (A), middle panel. After several seconds, a continuous outflow of Ringer's solution delivered with a pressure of 150 hPa was started (red trace). The $\Delta F/F$ response (black trace) of the $\beta$-glomerulus showed adaptation and dropped back to the base line within about 25 s. The $\beta$-glomerulus adapted to continuous exposure to a flow of Ringer's solution. The innervating ORNs measure accordingly not the absolute pressure or flow rate but rather the respective changes.
Figure 3.10 (A), last panel, shows the $\Delta F/F$ trace of the lateral cluster in a preparation in which the $\beta$-glomerulus responded to Ringer's solution puffs. No responses to puffs delivered with up to 300 hPa were observed in the lateral cluster. While activity following the application of Ringer's solution puffs was never observed in the lateral cluster, small areas of the medial cluster showed occasionally responses. However, these were either limited to the high pressure regime (>150 hPa) or caused by fibers projecting to the $\beta$-glomerulus. In any case, they were not observed consistently in different preparations.

The next set of experiments addressed the question whether the $\beta$-glomerulus' sensitivity is shaped by a dose-response curve, i.e. if the system potentially received information about the strength of the Ringer's solution puffs. Time series of the $\beta$-glomerulus were obtained while series of Ringer's solution puffs were delivered with different pressure amplitudes to the OE. The sequence in which the puffs were delivered was varied to exclude any effects of prolonged image acquisition on the response amplitudes. Measurements were taken with increasing and decreasing pressure strength between different applications. Also, random or alternating application schemes were used. For each of the 8 measured animals at least 3 measurements with multiple stimulations each were recorded. Figure 3.10 (B) shows traces for

two such measurements in the same manner as the previous panels of the figure. The maximum amplitude values changed with the amplitude of the pressure puffs as highlighted by the dotted lines. However, responses saturated after a certain pressure strength was reached and no response was observed for very weak puffs.
Although the response amplitudes were subject to variations, averaging of the results over repeated experimental trials resulted in the dose-response curve depicted in figure 3.10 (C). The blue asterisks denote the average values and the corresponding standard deviation of all measurements obtained from 8 different animals. The gray diamonds show the average values for the 8 animals individually. A sigmoidal was fitted to the average data points and the fit revealed a half-maximum pressure response at $78 \pm 18$ hPa.

These results demonstrate that the $\beta$-glomerulus shows adaptation to constant pressure application and that responses are shaped by a dose-response curve. The strength of the $\beta$-glomerulus' response is thus directly related to the strength of the Ringer's solution puff for a certain range of amplitudes (approximately $25 - 150$ hPa, cf. figure 3.10).

### 3.2.4 Several amino acids trigger responses in the $\beta$-glomerulus

It was already established in section 3.2.1 that apart from the $\beta$-glomerulus' sensitivity to Ringer's solution puffs, it is also stimulated by amino acids. However, the amino acids were only delivered in a mixture. The measurements were not coined at determining which individual amino acids activate the $\beta$-glomerulus. Consequently, the next set of experiments was dedicated to the evaluation of single amino acid stimulation and their effect on the $\beta$-glomerulus.
Longer interstimulus intervals are necessary in between stimulations with odorants to ensure wash-out. This is especially important if response amplitudes are to be evaluated. Thus, response traces of the Calcium Green electroporated $\beta$-glomerulus were obtained individually for all 15 amino acids and forskolin with one application per measurement and a minimum time between measurements of 2 min in a total of 9 different animals. The absolute increase in fluorescence intensity caused by the amino acids varied significantly between preparations and was subject to a number of undesired influences, such as staining intensity or funnel positioning. To exclude these disturbing factors and increase the comparability between preparations, all recorded traces were individually normalized to the maximum fluorescence

amplitude measured in response to a stimulation with the amino acid mixture. The application sequence for single amino acids was alternated for the different preparations to limit any potential influence of the total measurement duration or the stimulation sequence. Because of the $\beta$-glomerulus' sensitivity to mechanical stimulations, special care was taken to avoid any flow changes during stimulus application as described in section 2.3.2. Ringer's solution was applied regularly as a control stimulus to the funnel applicator ensuring that no responses were caused by the application alone.

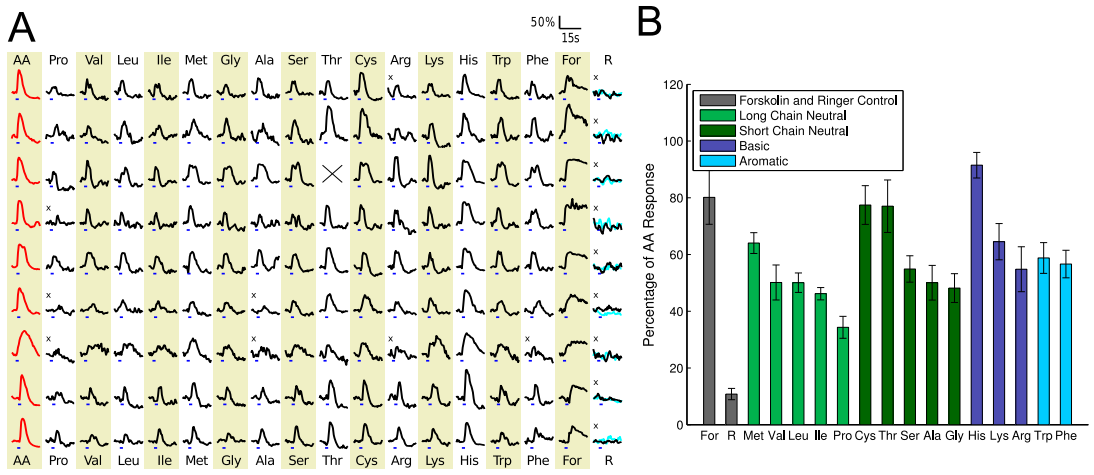


***Figure 3.11*** *– **(A)**$\Delta F/F$ traces for 9 $\beta$-glomeruli in different animals stained with Calcium Green via electroporation. For each animal, traces corresponding to stimulations with all 15 single amino acids and forskolin (For) are displayed. The traces were normalized to the maximal response caused by the amino acid mixture (AA). The first column shows the average signal of 3 stimulations with the amino acid mixture, the last column shows two control measurements for each animal with room-temperature Ringer (R). Traces marked with an x did not fulfill the response criterion (cf. section 2.4.1). **(B)** Average of the maximal response amplitudes for the 9 animals. The values are given relative to the average amino acid mixture response. Amino acid subgroups are color coded as indicated in the inset. Error bars, SEM. Image modified from [97].*

---

The recorded response traces are shown in figure 3.11 (A). The normalized traces for the amino acid mixture, the 15 individual amino acids, forskolin and the control are displayed for all 9 measured animals. While the control triggered no responses, all 15 amino acids activated the $\beta$-glomerulus individually. Out of the 134 individual amino acid applications, only 8 triggered an ambiguous calcium signal, which did not meet the criterion defining a stimulus-induced response (cf. section 2.4.1).

These are marked with a cross in figure 3.11 (A), specifically 3 for L-proline, 2 for L-alanine, 2 for L-arginine, and 1 for L-phenyalalanine were concerned. However, in most cases the response seemed to be only delayed. Overall, the data set indicates a general sensitivity of the $\beta$-glomerulus to all amino acids tested. Note that forskolin induced $[Ca^{2+}]$ increases in all experiments.

The broad sensitivity of the $\beta$-glomerulus to amino acids is rather exceptional. A previous study found that most amino acid-sensitive ORNs in *Xenopus laevis* tadpoles only respond to a small number of odorants [98, 99]. Another study reported a similar result at the level of the OB: 97 % out of 67 individually tested glomeruli in the amino acid-sensitive lateral cluster responded to less than 12 amino acids and not one of them responded to all 15 amino acids [89]. The $\beta$-glomerulus, in comparison, is a rather general amino acid-sensing structure. In addition, the responses to the different amino acids were found to be differentially tuned. Figure 3.11 (B) displays the average maximal response amplitudes for the individual amino acids and all 9 tested animals. The response strength varies significantly between individual amino acids. It covers a range between $34 \pm 4$ % for the smallest amplitude in response to L-proline and $92 \pm 5$ % for the highest amplitude corresponding to L-histidine. Values are given relative to the amino acid mixture response.

### 3.2.5 Response profile of individual axons

The previous results attested that the $\beta$-glomerulus possesses a rather broad response spectrum to amino acids not commonly found in single ORNs of *Xenopus laevis* [98]. This raises the question whether the broad sensitivity is achieved by one very general olfactory receptor or by several classes of ORNs with narrower response spectra. It is commonly assumed that only ORNs expressing the same olfactory receptor converge onto a single glomerulus [56]. However, the homogeneous innervation with only one class of ORN per glomerulus seems to have exceptions, particularly during development [56, 100]. It is thus worthwhile testing whether this general rule holds in the developing system of larval *Xenopus laevis* [55].

A first indication strengthening the 'one general amino acid receptor' hypothesis is provided by figure 3.11 (B). Since only a limited number of animals (n = 9) were evaluated, large variations of the response strength to individual amino acids would be expected, should different classes of ORNs with different sensitivities innervate

the $\beta$-glomerulus. The rather small SEM values indicate, however, constant ratios for the sensitivities between single amino acids. A more direct evaluation of the single ORN responses innervating the $\beta$-glomerulus is, nevertheless, desirable.
Unfortunately, although backtracing of ORNs innervating certain glomeruli is possible [44], it remains very tedious and can be subject to flaws if more than just the axons of the target glomerulus get stained. Furthermore, the success rate of this technique is too low to provide the necessary number of measurements. A more promising and more reliable approach is the separation of different axons directly within the $\beta$-glomerulus and the subsequent comparison of their individual response profiles. The electroporation technique in combination with the precise imaging capability of three dimensional structures provided by the line illumination microscope made it possible to distinguish at least two different axons per glomerulus. The tadpoles were electroporated with Calcium Green using the standard protocol consisting of 6 voltage pulses as described in section 2.2.1. The electroporation protocol typically resulted in a good staining of many ORNs and their axons. After electroporation, the living tadpoles were kept under low light conditions and electroporated again two days later. The second electroporation was performed with Alexa Fluor 647 and only 3 voltage pulses, limiting the staining to fewer ORNs. After a recovery time of at least 2 days, whole mount preparations were prepared and the $\beta$-glomerulus was imaged.

Figure 3.12 (A) shows representative results. A 3D stack of the $\beta$-glomerulus was recorded in two channels (green, Calcium Green; red, Alexa Fluor 647). Afterwards, subtraction imaging was used to facilitate the differentiation between areas stained with either the red or the green dye. Since Alexa Fluor 647 stained a smaller amount of ORNs, two sets of axons were found in each $\beta$-glomerulus: axons stained with Calcium Green and Alexa Fluor 647 and axons only stained with Calcium Green. A pair of response traces belonging to two different ORNs is obtained by selecting two regions of interest, one visible in both channels and the second visible only in the green channel. An example of two such regions is outlined in figure 3.12 (A). Note that the figure displays a maximum intensity projection while the region of interest selection was performed on the 8 individual layers of the image stack and is thus more precise. This method allowed the unambiguous identification of individual intraglomerular ORN fibers but is limited to two comparable axons per glomerulus. Each region chosen additionally might be connected to the ones selected previously.

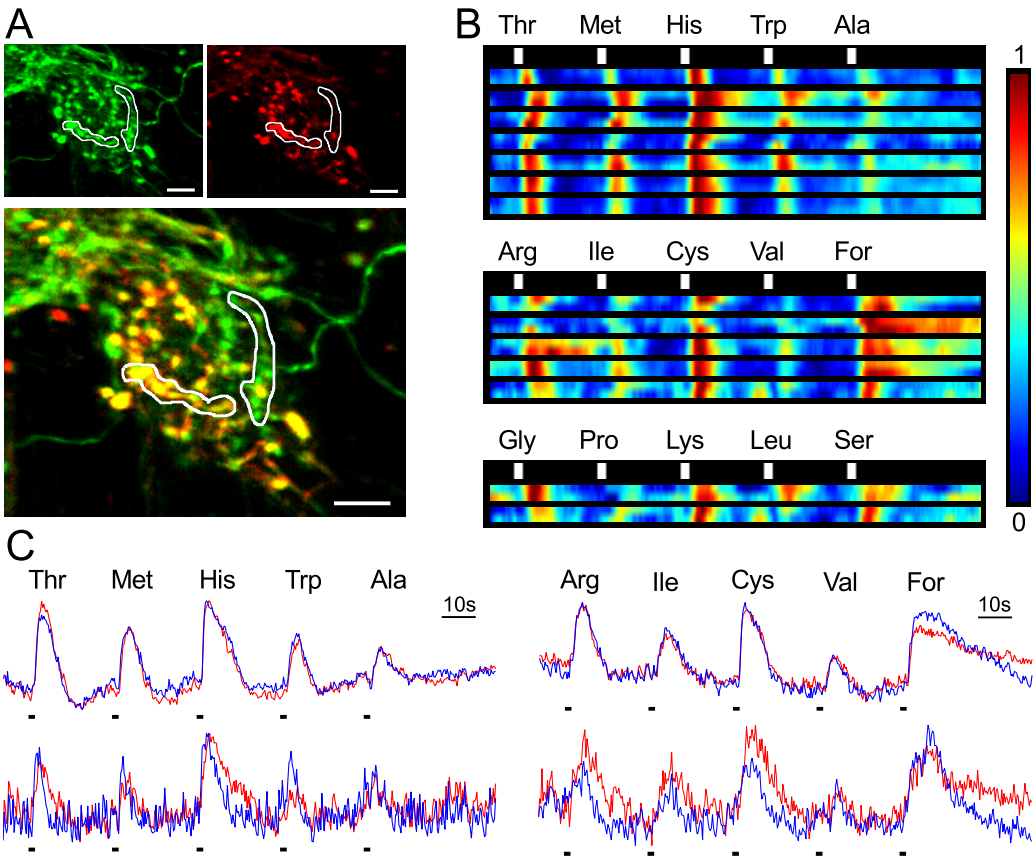


***Figure 3.12*** – ***(A)*** *Maximum intensity projections of a 9-µm-thick volume containing the β-glomerulus after application of subtraction imaging. The two upper images correspond to the Calcium Green staining and the Alexa Fluor 647 staining, respectively. The lower image shows the overlay of both channels. Two regions of interest belonging to different axons are indicated. Scale bar, 10 µm.* ***(B)*** *Normalized response traces corresponding to 7, 5 and 2 pairs of axons measured in different animals for 3 sets of stimuli. Each block shows two color-coded traces corresponding to different ORNs within the same β-glomerulus. Stimulus application is indicated by the white rectangles above the traces. Total recording time for each trace, 145 seconds.* ***(C)*** *Four pairs of traces showing the normalized response of ORNs within the β-glomerulus to two groups of different amino acids. The pair of blue and red traces in each set depict the normalized response for two different ORN axons within the same glomerulus. Each pair shows a high degree of correlation. The lower traces were taken from β-glomeruli responding with roughly 4 times smaller peak amplitudes. Bars below the traces indicate stimulus delivery. Image modified from [97].*

---

However, by measuring 7 different animals a total of 7 trace pairs could be obtained for a stimulation sequence of Thr, Met, His, Trp, Ala and 5 pairs for Arg, Ile, Cys, Val, forskolin and 2 for Gly, Pro, Lys, Leu, Ser. The stimuli of each set were delivered

subsequently in one measurement and the traces of each axon pair were compared. Figure 3.12 (B) shows the ΔF/F data as color-coded traces in a compact form. The 7, 5 and 2 sets of traces for the three different stimulus sequences are displayed. The similarity between axons from the same glomerulus is high and a slightly lower correlation can be observed between pairs obtained from measurements in different animals. Responses limited to only one of the fibers of a recorded pair were never observed.
Figure 3.12 (C) shows four pairs of normalized ΔF/F traces for two different stimulus sequences. Again, a very high similarity can be observed between the two traces from each pair (red and blue). The correlation is especially prominent for the strong amino acid induced responses in the upper traces. The lower traces had an approximately 4 times lower peak response to the amino acid stimulations. The normalized traces are thus stronger influenced by spontaneous activity which might explain the small differences for these two pairs.

Overall, the experiments performed in this section successfully separated individual fibers within one glomerulus. The analysis of the amino acid-induced response profiles revealed a high correlation between fibers within the $\beta$-glomerulus of the same animal. This is in line with the observation described at the beginning of the section and thus further supports the notion that the $\beta$-glomerulus is innervated by only one class of ORNs.

### 3.2.6 M/T cells innervate the $\beta$-glomerulus

All previous measurements performed on the $\beta$-glomerulus focused on the presynaptic side, i.e. the axons of ORNs innervating the $\beta$-glomerulus and stained by electroporation of the olfactory epithelium. The experiments described in this section aimed at establishing whether the $\beta$-glomerulus is innervated by dendrites from mitral/tufted cells (M/T cells) - the second-order neurons of the olfactory bulb - and whether the information gathered by the $\beta$-glomerulus is conveyed to these cells. For these experiments, Alexa Fluor 647 was electroporated into the ORNs to identify the location of the $\beta$-glomerulus. Afterwards, bolus loading with Fluo-8 AM was performed close to the $\beta$-glomerulus. Since the contrast after bolus loading is limited (cf. section 3.2.2), time series of 25-µm-thick volumes — divided into 6 layers and acquired with a frame rate of 31 Hz — around the $\beta$-glomerulus were used for activity correlation imaging. During those measurements up to 7 single amino acids

were applied in a stimulus sequence.

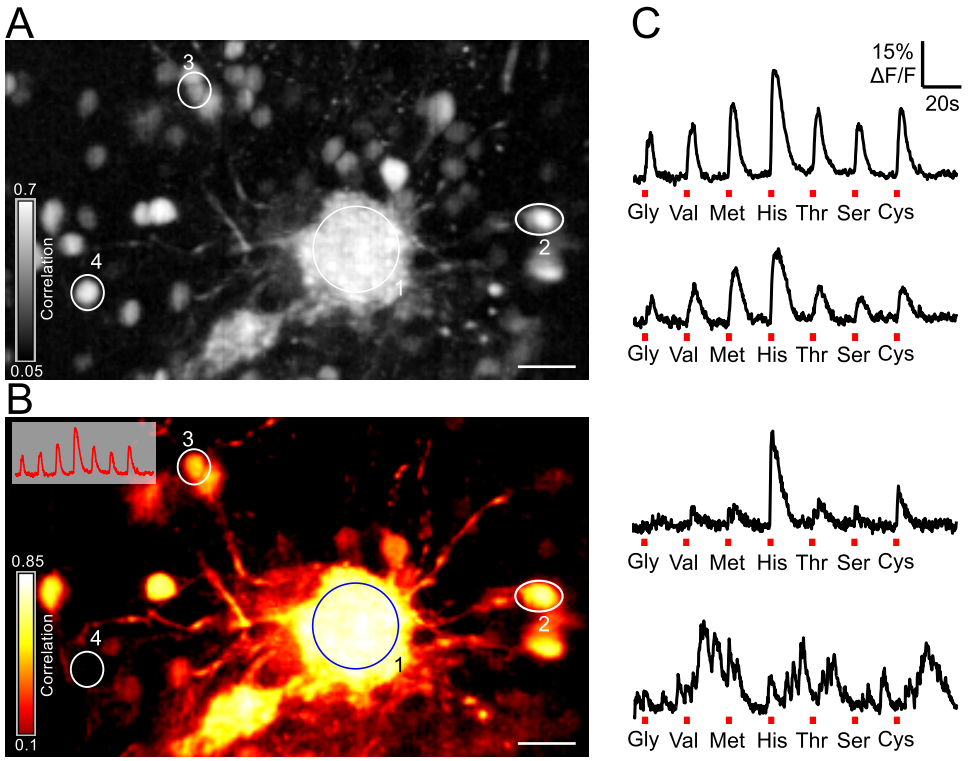


***Figure 3.13*** – ***(A)*** *Neighborhood correlation map of a 25-µm-thick volume containing the β-glomerulus (ROI 1). Surrounding M/T cell somata are visible.* ***(B)*** *Activity correlation imaging of the same data as in (A) with the reference trace shown as an inset and obtained from ROI 1. Dendrites connecting M/T cell somata to the β-glomerulus were revealed.* ***(C)*** *ΔF/F traces for the 4 outlined regions of interest: 1. β-glomerulus, 2. and 3. M/T cells with dendrites projecting towards the β-glomerulus, 4. M/T cell only visible in the neighborhood correlation map and with no apparent connection to the β-glomerulus. Scale bars, 20 µm. Image modified from [97].*

---

Figure 3.13 (A) shows the neighborhood correlation map obtained from such a recording. This map highlighted somata and neurites with correlated activity in neighboring pixels. The β-glomerulus is clearly surrounded by numerous active M/T cells. The map was used for the selection of regions of interest. A reference trace from the β-glomerulus was obtained for activity correlation imaging. The corresponding result is shown in figure 3.13 (B). The inset displays the reference trace. Compared to the neighborhood correlation map, the ACI map highlighted only M/T cells with an activity similar to that of the β-glomerulus. Consequently, less cell bodies were observed. However, the improved contrast revealed dendrites

for some of the M/T cells which were innervating the $\beta$-glomerulus. Note that maximum intensity projections of the correlation maps were created for display purposes. However, they were more accurately calculated on a layer-by-layer basis. The panel (C) of the figure shows the $\Delta F/F$ traces for the 4 indicated regions of interest. The first trace corresponds to the $\beta$-glomerulus and the second trace shows a very similar response profile as would be expected from an M/T cell directly innervating the $\beta$-glomerulus. The third trace belongs to another M/T cell with a connection to the $\beta$-glomerulus and a response profile displaying reduced sensitivity for all tested amino acids except L-histidine and L-cystein. The last trace belongs to an M/T cell activated independently from the $\beta$-glomerulus and without any apparent connection to it. It appears accordingly only in the neighborhood correlation map, not in the ACI map.

Many M/T cells in the proximity of the $\beta$-glomerulus followed its responses to amino acid stimulation closely. Furthermore, ACI revealed M/T cell dendrites connecting to the $\beta$-glomerulus for a total of 7 M/T cells in 3 measurements. The $\beta$-glomerulus is thus innervated by the second-order neurons of the olfactory system. Furthermore, the existing differences regarding the response patterns of the connected M/T cells hint at a complex processing of the information conveyed by the $\beta$-glomerulus.

### 3.2.7 Mechanical stimuli influence M/T cell networks

The previous section established that the $\beta$-glomerulus is connected to M/T cells and amino acid sensitivity is conveyed to these second-order neurons. This section subsequently investigated the influence of the $\beta$-glomerulus' sensitivity to puffs with Ringer's solution on M/T cells. The experiments were performed on Fluo-8 AM stained olfactory bulbs and sequences of Ringer's solution puffs were delivered to the OE.

Figure 3.14 (A) shows in red the puff strength in hPa and in black the $\Delta F/F$ traces of different regions of interest. Two sets of traces are displayed, the traces in each set were recorded in the same measurement. The first trace was taken from the dendrites forming the postsynaptic side of the $\beta$-glomerulus ($\beta$-Gl) and shows the expected increases in fluorescence intensity upon stimulation with Ringer's solution puffs. The second trace of each set shows M/T cells (MC1) in the neighborhood of the $\beta$-glomerulus which responded in the same way as the glomerulus itself. These

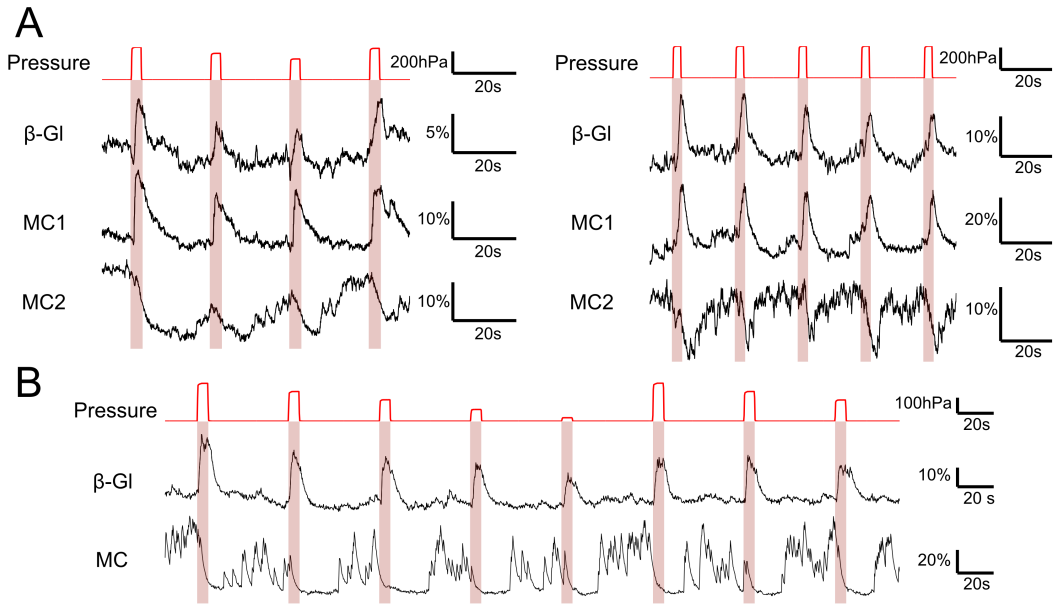


***Figure 3.14*** *– **(A)** $\Delta F/F$ traces from two measurements in Fluo-8-stained olfactory bulbs. Response profiles for 4 different M/T cells (MC1-2) to puffs delivered to the olfactory epithelium and the responses of the corresponding $\beta$-glomerulus ($\beta$-Gl). The red traces display the applied pressure pulses. For both measurements an M/T cell showing positive responses to pressure stimulation and a second one showing inhibition are displayed. **(B)** Similar to (A) but with a different animal and a longer recording. The displayed M/T cell showed extensive spontaneous activity and strong inhibition following each stimulus. Image modified from [97].*

---

were most likely directly innervating the $\beta$-glomerulus since no other presynaptic structure was responding to Ringer's solution puffs. The information gathered by the $\beta$-glomerulus regarding mechanical stimulation was thus also relayed to the second-order neurons. The last traces of the two displayed sets are particularly interesting. In both cases different M/T cells (MC2) were inhibited in their spontaneous activity upon stimulation of the OE with Ringer's solution puffs. Further measurements revealed more inhibited M/T cells. A particularly good example is shown in figure 3.14 (B). The postsynaptic $\beta$-glomerulus responded to the Ringer's solution puffs, as expected, with increases of $[Ca^{2+}]$. The strength of the increase was related to the amplitude of the pressure puff. The $\Delta F/F$ trace of the M/T cell, on the other hand, revealed a pronounced spontaneous activity interrupted by silent periods after each puff. The puffs induced a strong and long lasting inhibition on this M/T cell. Consequently, information regarding mechanical stimulation is not only conveyed

and processed by M/T cells connected to the $\beta$-glomerulus but also influences other parts of the network by inducing inhibition.

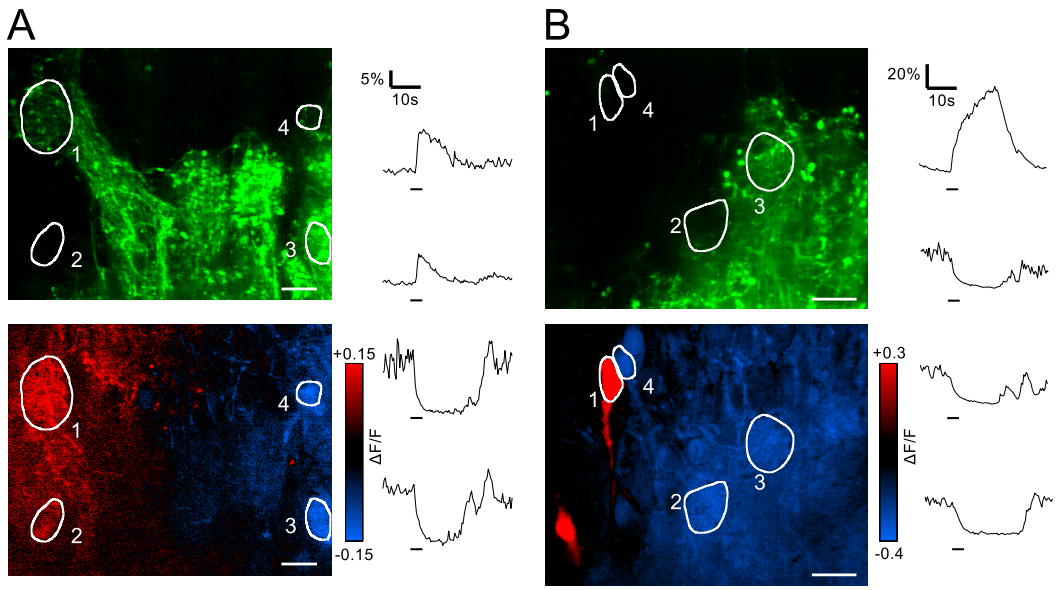


***Figure 3.15*** *– **(A)** Upper image, Alexa Fluor 647-electroporated ORN axons. The field of view contains the $\beta$-glomerulus (ROI 1) and a part of the lateral cluster which comprises ROI 3 and 4. Lower image, $\Delta F/F$ map of the same field of view at maximum response during a puff of 150 hPa delivered to the olfactory epithelium. The staining was achieved by bolus loading with Fluo-8 AM. The color coding refers to positive (red) and negative (blue) responses. On the right side of the images are $\Delta F/F$ traces for the 4 indicated ROIs displayed. **(B)** similar to (A) but with a field of view containing only the lateral cluster and the surrounding M/T cells. Scale bars, 20 µm. Image modified from [97].*

A closer look at the acquired data sets revealed that many inhibited M/T cells were located at the border of the field of view centered on the $\beta$-glomerulus. Accordingly, the field of view was extended for the next set of experiments. An example of such a recording is shown in figure 3.15 (A). The upper image shows in green an Alexa Fluor 647 staining of the ORN axons for orientation. The $\beta$-glomerulus can be identified (ROI 1) and the border of the lateral cluster comprising ROI 3 and 4 is visible on the right side. The lower image shows a color-coded map of the peak $\Delta$F/F response to a 150 hPa puff. This image was recorded in the second channel and corresponds to the Fluo-8 AM staining of the M/T cells and their dendrites. Black areas signify almost no changes in fluorescence intensity while red areas re-

sponded with an increase and blue areas with a decrease of fluorescent intensity. Clearly, the $\beta$-glomerulus and the surrounding area, including an M/T cell at ROI 2, were activated by the puff. Interestingly, the visible parts of the lateral cluster were completely inhibited. This is reflected in the traces on the right side of the images. The upper two correspond to the positively reacting regions 1 and 2, the lower ones to the inhibited part of the lateral cluster and regions 3 and 4. Figure 3.15 (B) shows the same experiment performed on a field of view centered on the lateral cluster of a different animal. Again, large parts of the lateral cluster, including the postsynaptic fibers of the glomeruli (e.g. ROI 2 and 3), were strongly inhibited. On the other hand, two M/T cells (e.g. ROI 1) showed a strong increase in fluorescence intensity. Again, the $\Delta F/F$ traces on the right side correspond to the four indicated regions of interest. Note, that the images presented here are not maximum projections but single layers. Although the inhibition of the lateral cluster was very widespread it did not extend to the whole volume of the cluster. The inhibition of postsynaptic glomeruli in the lateral cluster was observed in 4 (out of 6) more measurements with different animals and covered always multiple glomeruli. Since no such effect was observed on presynaptic glomerular fibers, it is likely that the information conveyed by the $\beta$-glomerulus influences large parts of the M/T cell network. In any case, mechanical stimuli have a widespread impact on the network of second-order neurons.

## 3.3 Simultaneous calcium imaging of first- and second-order neurons

In the previous chapter the properties of both first- and second-order neurons of the olfactory bulb were analyzed regarding thermo-, chemo- and mechanosensitivity. Often 2-channel recordings were used, for example as a counter staining or for the identification of different axons within one glomerulus. The LIM — as described in the first chapter of the results — was also designed to perform 2-channel recordings with two different calcium dyes. A combination of the dextran conjugated Fluo-4 (Thermo Fisher Scientific) electroporated to the ORNs and Rhod-2 AM or X-Rhod AM (Thermo Fisher Scientific) staining on the M/T cell level was considered very promising for such experiments. Unfortunately, the production of the dextran-conjugated Fluo-4 dye was discontinued by the manufacturer and only suboptimal combinations for 2-channel measurements remained, as will be discussed in

the next sections. As a consequence, the measurements in the previous chapter were performed in a sequential way; firstly on ORN axons, secondly on M/T cells. Only this separation into two sets of experiments allowed us to use always the best suited calcium indicator. Lately, additional calcium-sensitive dyes were developed in the Department of Organic and Biomolecular Chemistry (Göttingen) and preliminary results indicated a high potential for 2-channel recordings. Since the development of these new dyes was only very recently finished, measurements with the new fluorophores could not be included in this thesis. Instead, this chapter will explore the possibilities and limitations of simultaneous 2-channel recordings based on the results of the previous two chapters. It will thus deal with the third goal mentioned in section 1.4.

The small cluster is a very suitable target for 2-channel recordings closely located at the ventral surface of the OB and thus offering good imaging conditions. The results discussed above raise further research questions addressable with such measurements. How is the dual sensitivity of M/T cells to temperature drops and odorants explained? How do simultaneous amino acid and flow changes influence the coding via the $\beta$-glomerulus? Both questions would benefit from the possibility of simultaneous calcium recordings in first- and second-order neurons.

Therefore, given that the LIM was improved and the technical possibility of fast 2-channel recordings was thus established, we will consider the following questions:

- Which calcium dyes can be used?
- Can the recordings be performed on the level of single axons or are they limited to whole glomeruli?
- Can single dendrites within a glomerulus be recorded or are experiments limited to the M/T cell somata level?

### 3.3.1 Available dyes

The major obstacle remaining for simultaneous 2-channel recordings is the combination of two calcium-sensitive fluorophores.

The staining of ORNs by electroporation, which enabled recordings on functional glomeruli in the OB, was only successful with a limited number of different fluorophores. As a calcium sensor, Calcium Green was used very reliably. However, no alternatives exist at the moment. Rhod is available as a dextran conjugated dye but extensive trials with various electroporation procedures performed by Thomas Offner in our laboratory did not yield promising results. The staining density was low and only few structures in the OB showed responses. Different staining techniques, like ligand-induced staining, exist and were studied in our laboratory but are not yet providing sufficient staining efficiency to serve as alternatives. Consequently, Calcium Green remained the only choice for the ORN electroporation. A red calcium indicator is thus necessary for the staining of M/T cells. Since bolus loading principally works with all AM dyes, a couple of choices exists. Rhod-2 AM is for example a possible candidate and its spectrum can be separated with the two channels of the LIM (cf. section 3.1.1 and figure 3.2). The overlap during excitation with the 488 nm laser can be reduced further when X-Rhod-1 is used instead of Rhod-2 as shown in figure 3.16. With both combinations, a cross talk effect exists only in one channel and can be corrected.

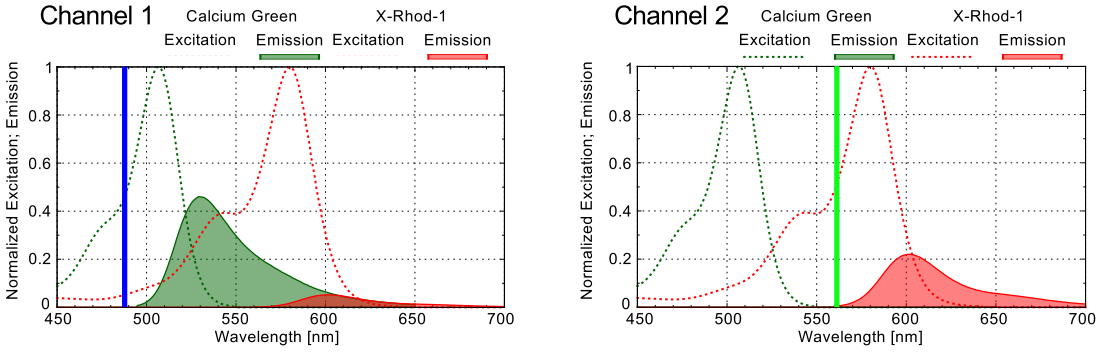


***Figure 3.16*** – *Excitation and emission spectra of Calcium Green and X-Rhod-1 in the two excitation channels. Left image, Channel 1 with 488 nm excitation. Right image, Channel 2 with 561 nm excitation. Data was obtained from [93].*

Unfortunately, the calcium binding dynamics of CalciumGreen, Rhod-2 and X-Rhod-1 are quite different. Table 3.2 shows that Calcium Green has a significantly lower $k_d$ value than the other two dyes. Consequently, both the response dynamics as well as the potential buffering effect differ. This makes the comparison between the responses of the first- and second-order neurons difficult. Furthermore, bolus

loading with Rhod-2 and X-Rhod-1 was mostly unsuccessful. Increasing the number of injections yielded a staining of M/T cells but activity was so rarely observed that no simultaneous 2-channel calcium recordings could be performed.

Most recently the development of a new, red calcium-sensitive dye in the Department of Organic and Biomolecular Chemistry (Göttingen) showed very promising results in combination with electroporation and measurements at the level of the OB[2]. Such a dye would replace Calcium Green and enable the use of Fluo-8 AM for M/T cells. Fluo-8 has been used throughout this thesis because it yielded the good staining results and signal-to-noise ratios.

| Calcium Indicator | Absorption [nm] | Emission [nm] | $k_d$ [nM] |
|---|---|---|---|
| Calcium-green-1 | 506 | 531 | 190 |
| Rhod 2 | 556 | 576 | 1000 |
| X-rhod 1 | 576 | 602 | 700 |

***Table 3.2*** *– The table lists the wavelength with maximal absorption and emission as well as the $k_d$ values for the different calcium indicator dyes. Data obtained from [101].*

### 3.3.2 Single axon recordings

The resolution on the presynaptic side after electroporation is very satisfying as can be seen in the respective images throughout the thesis (e.g. figure 3.7). It is possible — especially in the well-separated small cluster — to record from small parts of single axons. It is, however, far more challenging to differentiate between fibers of different ORNs within a glomerulus. Double electroporation was successfully established in section 3.2.5 of this thesis but is limited to a small amount of fibers. ACI provides a different approach to this problem. Fibers could potentially be separated based on activity. Figure 3.17 (A) proves that this is generally possible. The figure shows a glomerulus recorded with the LIM. Clearly, the application of subtraction imaging led to a better contrast and reduced the amount of out-of-focus light, which is crucial for the subsequent separation of single axons. Applying ACI on the subtraction imaging result revealed two different components. Figure 3.17 (B) shows two sets of traces obtained from different regions within the glomerulus.

[2]Experiments performed by Guobin Bao in our laboratory.

A trace from each set was used to generate the ACI result shown in (A). The traces within each of the two sets displayed a high correlation and belonged most likely to a fiber from the same ORN. Regions exhibiting the same activity pattern were found in very different locations of the glomerulus. However, it is known that ORN axons innervate glomeruli in a dense and complicated way often bifurcating multiple times [62]. Consequently, a distribution of similar activity patterns throughout the glomerulus is not unexpected. The differences in between the two depicted sets in figure 3.17 (B) were large enough to separate them well by activity correlation imaging (cf. 3.17 (A)). The separation of axons by their activity is hence generally possible and not necessarily limited to only two axons as in the example. The differences in the response patterns were caused, to a significant degree, by different spontaneous activity. Unfortunately, spontaneous activity is only rarely observed with Calcium Green in ORN axons. Stimulus induced responses, at least in the $\beta$-glomerulus, are strongly correlated between different fibers within a glomerulus (cf. figure 3.12) and not useful for ACI-based separation.
The general question of separability of single axons in glomeruli was studied by Daniëlle de Jong in our laboratory. While her findings regarding Calcium Green were in line with the observations reported here, a different, recently developed dye (JG205[3]) showed more promising results probably due to faster dynamics and thus a better visibility of spontaneous activity [102].

In summary, the electroporation technique combined with subtraction imaging and 3D recordings of the LIM can be used to differentiate single axons within a glomerulus. This was performed successfully with a double labeling approach in this thesis. However, a more flexible separation by activity is possible although the successful application will depend on the availability of new calcium-sensitive fluorophores.

### 3.3.3 Single dendrite recordings

The staining of the M/T cell network by bolus loading is much denser and thus poorer in contrast as opposed to the fibers from ORNs in the olfactory bulb. The reasons for this — M/T cell somata located in the same area and dye delivered directly to the region of interest — have already been discussed in section 3.2.2. The basal fluorescence of the staining is insufficient to distinguish many structures. In

[3]Developed by Julia Graf, Department of organic and biomolecular chemistry, Göttingen.

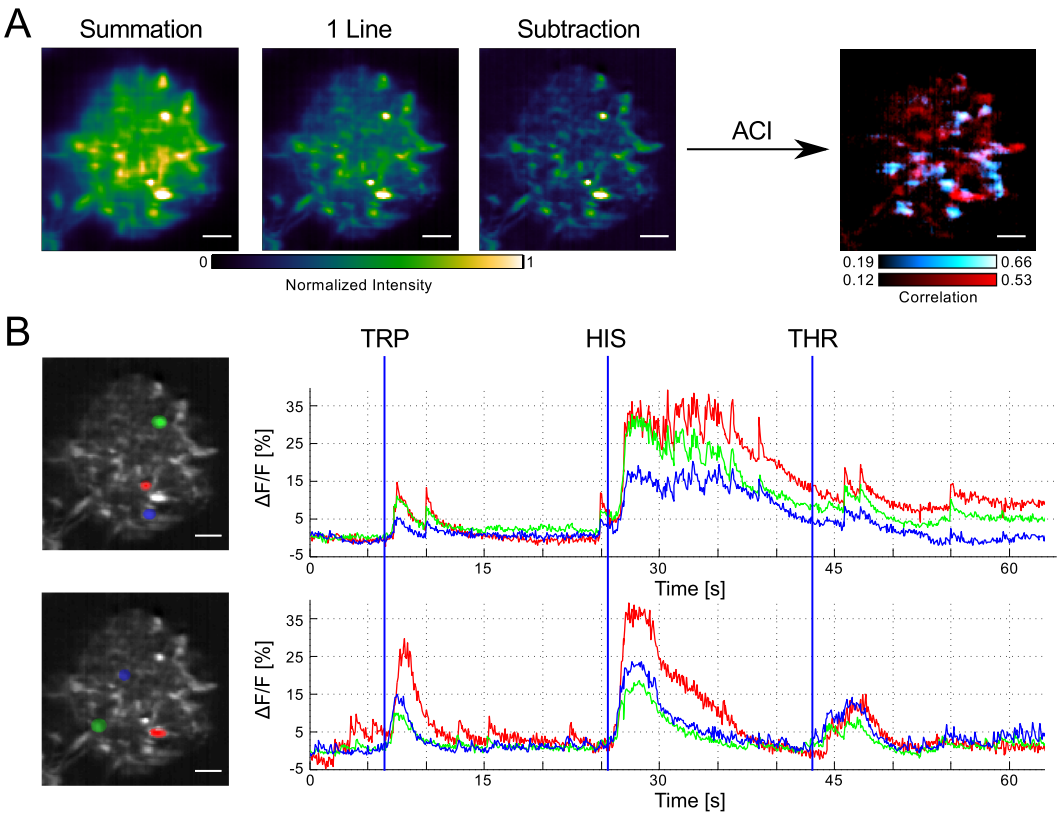


***Figure 3.17*** – ***(A)*** *Recording of a glomerulus, from left to right: with summation of multiple lines corresponding to an open aperture state of 3.45 AU, a normal confocal central line recording corresponding to 0.46 AU and the same image after application of subtraction imaging. All images are shown with normalized intensities. The last image on the right shows the glomerulus after application of subtraction imaging and ACI corresponding to two different reference traces coded in red and blue.* ***(B)*** *Same glomerulus as in (A) with two sets of regions of interest each consisting of three separate regions. On the right side of the images the ΔF/F traces corresponding to the indicated regions of interest are shown. Blue vertical bars indicate stimulus delivery. The two red traces were used as reference traces for ACI in (A). Scale bars, 5 µm.*

figure 3.8, section 3.2.2, it was shown that ACI applied to a recording with induced stimulations can generate contrast in an image where few structures were formerly distinguishable. Another advantage of the M/T cell staining is that Fluo-8 AM reveals a significant amount of spontaneous activity which can be used to distinguish different M/T cell networks. This works especially well on the larger scale of multiple glomeruli and M/T cell somata as was previously described by Junek et al. [3]. An example of such a measurement with subsequent application of ACI is presented

in figure 3.18. The first panel shows a neighborhood correlation map which was used to generate enough contrast for region of interest selection. The next four images show color-coded ACI maps as an overlay to the gray neighborhood correlation map. They correspond to the respective normalized reference traces in the last panel. ACI revealed nicely the different areas exhibiting similar activity. Unfortunately, the contrast within the glomeruli is too low to distinguish single dendrites. Adjusting the imaging settings and scanning a single glomerulus with higher resolution can sometimes provide - after application of ACI - sufficient contrast for separating dendrites.

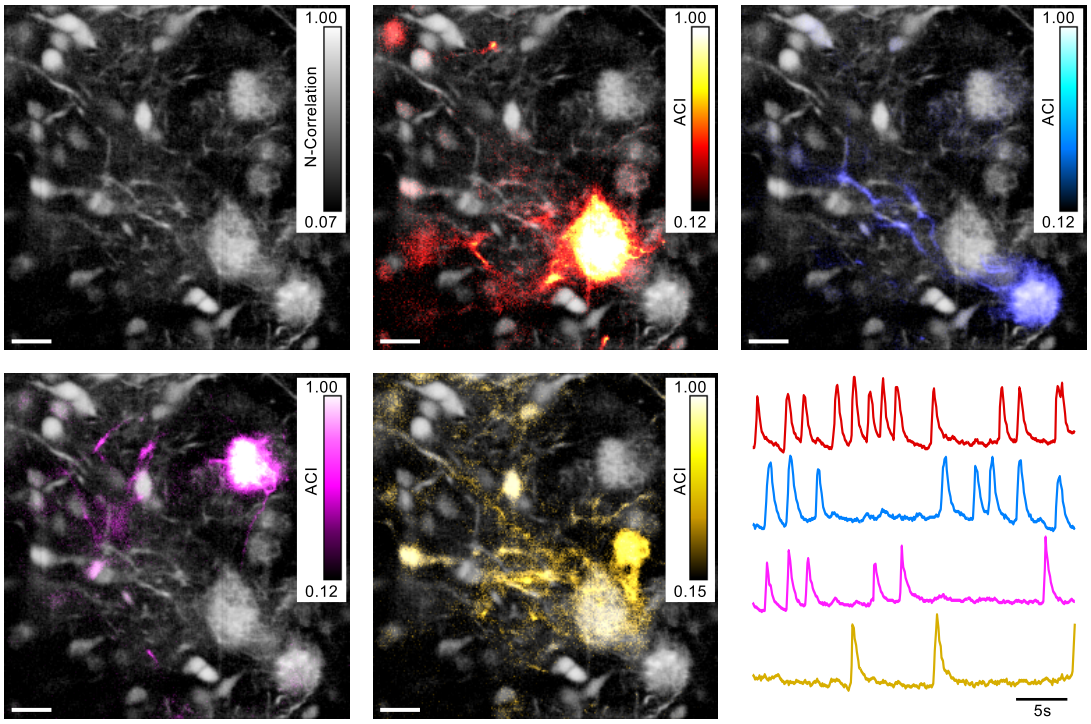


***Figure 3.18*** – *Recording of the olfactory bulb after Fluo-8 AM bolus loading. Spontaneous activity was used to generate contrast. The first panel displays the neighborhood correlation map, subsequent panels show an overlay of ACI maps to the neighborhood correlation. The last panel displays the corresponding reference traces. The traces are individually normalized. Scale bar: 20 µm*

---

Spontaneous activity is an unreliable ally when focusing on a specific structure. The target might not show any spontaneous activity or too little of it. This would render the preparation useless and would limit experiments to preparations with strong spontaneous activity thereby creating a potential bias. A more reliable generation of meaningful reference traces is therefore essential. Generating such a sequence by

stimulation can be achieved with odorant stimulation (cf. figure 3.8). The disadvantage is that many cells react to odorants and that the responses are relatively long. Consequently, long interstimulus intervals are necessary and the correlation is less precise. Here, studies performed at the small cluster have the valuable alternative of temperature and mechanical stimulations. Both were limited to a smaller number of sensitive cells and thus better distinguishable from background activity. Furthermore, analyzing the response profiles of the $\beta$-glomerulus revealed that especially the activity induced by Ringer's solution puffs follows the stimulus application much more closely than the stimulation with odorants. Figure 3.19 shows the average response profile to a stimulation with the amino acid mixture (n = 9), forskolin (n = 9), and Ringer's solution puffs (n = 5). The data for amino acids and forskolin were obtained from the same set of experiments as presented in figure 3.11. All traces were fitted with the following function:

$$f(x) = a + b \cdot \left(e^{\frac{-x}{\tau_1}}\right) \cdot \left(1 - e^{\frac{-x}{\tau_2}}\right) \ . \tag{3.1}$$

The variables $a$, $b$, $\tau_1$, and $\tau_2$ were freely fitted and the fit is plotted as a blue line. Furthermore, the duration of the Ringer's solution puff is shown as a red shade over the trace of the last panel. The onset of the response was delayed but the overall duration of the response lasted only slightly longer than that of the stimulation. All response traces were individually fitted and the FWHM was determined. For forskolin the responses outlasted the measurement duration. The FWHM could thus not be accurately determined but was on average longer than 14 s. For the amino acid mixture the FWHM was determined to $4.3 \pm 1.6$ s and for the Ringer's solution puff to $2.7 \pm 0.2$ s. Consequently, Ringer's solution puffs provide a controllable stimulus with narrow responses and are well-suited to generate reference traces for ACI. Amino acid responses lasted on average longer and the response duration varied significantly between measurements depending on funnel an outflow positioning. These differences in the response shapes are useful to distinguish $[Ca^{2+}]$ increases caused by odorants and those affiliated with mechanical stimuli.

Figure 3.20 shows a stimulus-generated reference trace. Panel (A) displays the generation of the reference traces. Ringer's solution puffs with various pressure amplitudes were delivered to the OE over a recording time of 145 s. The $\Delta F/F$ response to the stimulus sequence is depicted below. This reference trace was then

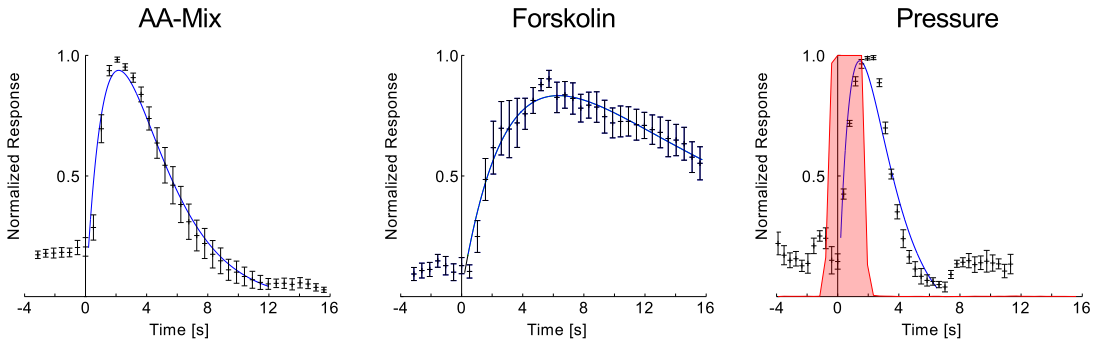


***Figure 3.19*** – *Normalized response of the β-glomerulus from left to right to the amino acids mixture, forskolin and a pressure pulse averaged over 9, 9 and 5 applications, respectively. Blue lines indicate the result of the fit. The red overlay shows the duration of the pressure application. Error bars, SEM.*

---

used for activity correlation imaging, as depicted in Panel (B), where the first image shows Alexa Fluor 647-electroporated ORN fibers and the second panel, the ACI result for M/T cell dendrites. The ACI map generated sufficient contrast to distinguish different dendrites and the merge in the last panel reveals that the presynaptic intensity image and the postsynaptic ACI map provide information about complementary structures. Replacing the Alexa Fluor 647 with a suitable calcium-sensitive dye would enable simultaneous recordings of the fibers of first- and second-order-neurons within a single glomerulus.

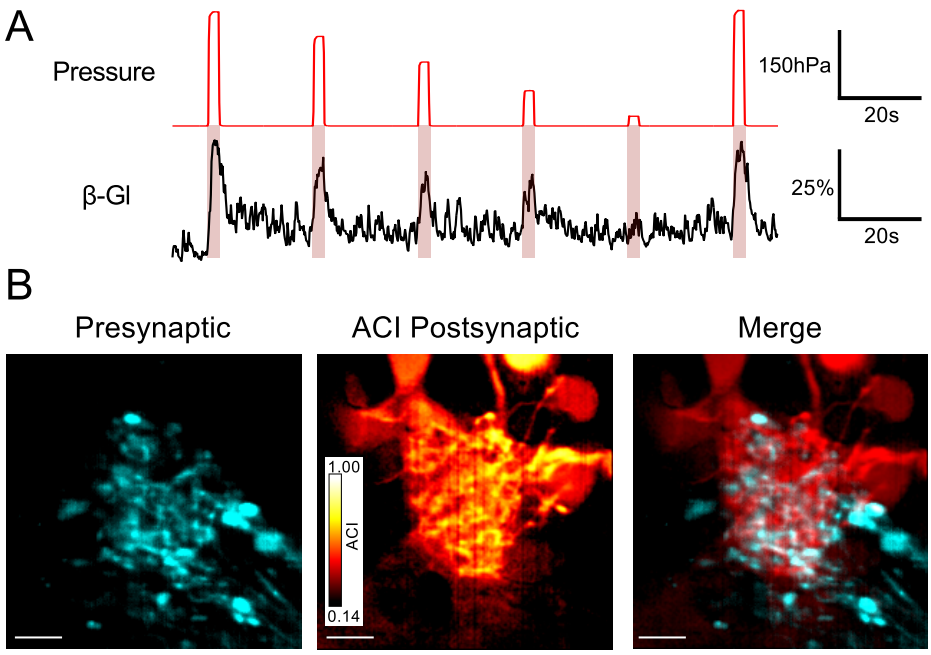


***Figure 3.20*** – ***(A)*** *Upper trace: pressure strength applied over time. Lower trace: $\Delta F/F$ trace for the postsynaptic fibers of a Fluo-8 AM-stained $\beta$-glomerulus.* ***(B)*** *From left to right: Alexa Fluor 647-stained axons of the $\beta$-glomerulus, ACI map of the M/T cell dendrites calculated with the reference trace shown in (A), merge of the presynaptic intensity map and the postsynaptic ACI map. Scale bars, 20 µm.*

# 4 Discussion

## 4.1 Imaging

### 4.1.1 Subtraction imaging and pixel reassignment

Pixel reassignment improves the imaging quality the line illumination microscope. Although the best resolution is achieved with a small confocal aperture, pixel reassignment performs significantly better than simple summation (cf. table 3.1). Confocal apertures of about 1 AU offer a better trade-off between signal-to-noise ratio and resolution and are therefore more commonly used than smaller ones. Binning several camera lines together was thus often used and the comparison between reassignment and simple binning is more relevant than the theoretically achievable maximal resolution with only one line. The reassignment can be as easily performed as the normal summation and comes at no additional costs, making it a valuable improvement for almost all measurements. In addition, pixel reassignment increases the peak intensities and can further enhance the signal-to-noise ratio (cf. figure 3.5).

The implementation of pixel reassignment in the Zeiss Airy Scan module can increase the resolution of a point scanning setup up to 1.7 fold compared to widefield imaging [31]. However, this is achieved by a combination of pixel reassignment and deconvolution and consequently demands high computational power. Pixel reassignment alone can improve resolution in a point scanning setup up to 1.53 fold but is limited to 1.45 fold in a practical implementation [25]. For comparison, a normal confocal recording would yield an improvement factor of 1.39 [25].
In line illumination microscopes the reassignment is limited to the direction perpendicular to the line. The improvement in resolution is smaller. The resolution of the LIM after reassignment was close to the theoretical value given by equation 2.5. For example, the resolution in the y-direction with the 40x/0.8 objective after pixel reassignment was determined to $380 \pm 10$ nm. The theoretical resolution calculated

with an emission wavelength of 505 nm for the fluorescent beads and equation 2.5 is 385 nm. Without reassignment and with the same amount of lines binned together the resolution was limited to $430 \pm 10$ nm. In conclusion, pixel reassignment for our line illumination microscope does not yield an improvement beyond the theoretical value as achieved by the combination of point scanning, pixel reassignment and deconvolution [31]. However, pixel reassignment in our LIM was successfully used to improve SNR without sacrificing resolution as a simple summation would (cf. table 3.1).

The determination of the spatial resolution revealed a considerable difference between the resolution perpendicular to the line and the resolution parallel to the line. This is a common disadvantage of line illumination setups, although normally observed to a lesser degree [95, 96]. The large difference measured here can be explained by the fact that beads from different positions along the line were analyzed and averaged. If only beads in the middle of the line were evaluated, the resolution along the x-direction was smaller and approached the typical factor of 1.3 compared to the y-resolution.

Heintzmann et al. [94] analyzed the performance of subtraction imaging for a point scanning setup in some detail. While they confirmed the resolution enhancement both in the lateral and axial direction, they also mentioned that the SNR is deteriorated by subtraction imaging. Furthermore, they showed that a posteriori image processing can achieve similar results without reducing the SNR. Nevertheless, subtraction imaging can be applied with minimal computational power and can thus be performed online during data acquisition. Furthermore, it can be used on a single recorded frame whereas the image processing techniques suggested by Heintzmann et al. [94] need a fully and precisely recorded stack.
Subtraction imaging, in the way it was implemented for our LIM, significantly improves the optical sectioning capability (cf. section 3.1.2), a finding which is in line with a previous result [29]. Yet, the SNR decreased after applying subtraction imaging, as expected. The technique is thus well suited for all recordings where SNRs are less important but a high demand for good optical sectioning exists. The measurements in section 3.2.5 illustrate how this method can be successfully applied. Here, the differentiation of single fibers within a glomerulus demanded reliable optical sectioning. Since Calcium Green and Alexa Fluor dyes provided sufficient signal

intensities, the slight reduction in SNR was acceptable. Finally, pixel reassignment and subtraction imaging can be combined and provide a compromise between lateral resolution, SNR and optical sectioning capability.

### 4.1.2 Future developments of the LIM

Line illumination microscopy competes with a number of other fast imaging techniques. Its simplicity and flexibility are a significant advantage and the imaging speed of up to 400 Hz for areas of 64 x 1024 pixels with line dwell times of 40 µs certainly belongs to the highest acquisition rates achievable with confocal microscopes. A standard cLSM would achieve only 0.4 Hz for the same area and pixel dwell time. In particular, the recording of several emission lines enables a very flexible post-processing. The confocality can be chosen a posteriori and subtraction imaging or pixel reassignment can be performed and combined. The implementation of 2-channel recordings via a separation based on excitation yields a very high recording efficiency. Besides, the speed and flexibility of line illumination microscopes enable measurements on large neuronal networks.

Future improvements might encompass the application of pixel reassignment or subtraction imaging directly during data acquisition. Using mirrors with a single reflecting line [22] as a replacement for the dichroic mirrors can further enhance the detection efficiency. Finally, the readout of the camera chip is still not flexible enough. Although the necessary additional lines for subtraction imaging can be recorded, the acquisition of more than 4 additional camera lines still limits the imaging speed. The usage of subtraction imaging thus always poses a trade-off between resolution and speed. Fortunately, the readout duration is mainly prolonged because the camera lines cannot be collected individually. To gather information from the off-center lines, all lines between the central line and the desired off-center line have to be acquired as well. This problem will likely be solved in one of the next updates of the camera control framework.

## 4.2 The small cluster

The septal organ and the Grüneberg ganglion are two olfactory subsystems in rodents detecting mechanical, temperature and chemical stimuli [71, 74]. The olfactory

system of *Xenopus laevis* tadpoles perceives these modalities as well. The initial registration step takes place in ORNs of the main olfactory epithelium. Temperature and mechanical stimulation is further processed in the small cluster of the olfactory bulb. The distinct subsystems septal organ and GG in rodents are located in the nose but separated from the main nasal epithelium [72]. In contrast, mechano- and thermosensitive ORNs in *Xenopus laevis* tadpoles are located together with chemosensitive ORNs in the main olfactory epithelium. The processing in the olfactory bulb is performed in the small cluster remotely located in a ventral and rostral position relative to the other clusters. The results of this thesis demonstrate that temperature and mechanical stimuli elicit $[Ca^{2+}]$ increases in the small cluster only. However, at the M/T cell level both stimuli have a larger impact and are strongly interconnected with the processing of odorants.
The temperature and pressure sensitivity are thus encoded in the OB of *Xenopus laevis* tadpoles. The small cluster is still identifiable within the glomerular layer after metamorphosis [60] but it is unknown whether it remains mechano- and thermosensitive.

### 4.2.1 $\gamma$-glomerulus: Temperature sensitivity

The temperature sensitivity of the Gruneberg ganglion (GG) in mice has been demonstrated by Brechbühl et al. [76]. However, measurements were only performed at the level of the olfactory epithelium. Later measurements by Eugen Kludt in *Xenopus laevis* revealed the temperature sensitivity of the $\gamma$-glomerulus in the olfactory bulb [44]. Temperature information gathered in the olfactory epithelium is thus conveyed to M/T cells and processed in the olfactory bulb.
The dual-sensitive M/T cells described in section 3.2.2 revealed that thermo- and chemosensitivity are interconnected. Both qualities are processed in shared cellular networks. The experiments performed on whole mount preparations revealed in each of the 7 performed experiments more than 3 M/T cells responding to temperature drops. Often the number was much higher (cf. figure 3.9). In contrast, the screening for dual-sensitive cells in slices revealed only 32 temperature sensitive M/T cells out of 183 recorded. The screening was performed on a larger field of view and not focused to the $\gamma$-glomerulus. A smaller number of thermosensitive M/T cells was thus to be expected. Comparing the two experiments suggests that M/T cells in the neighborhood of the $\gamma$-glomerulus have a higher probability of being

thermosensitive. Interestingly, 59 % of the recorded thermosensitive M/T cells were dual-sensitive. Consequently, the combined processing of thermo- and chemostimuli is rather the rule than the exception.
Temperature-sensitive GG neurons in mice also respond to some chemical stimuli [78]. In contrast, no chemical stimulus eliciting activity in the $\gamma$-glomerulus was found [44]. Consequently, the activation of M/T cells by both L-histidine and temperature drops cannot be explained by a response of the $\gamma$-glomerulus alone. The dual sensitivity is likely a property of M/T cells innervating two glomeruli, the $\gamma$-glomerulus and a second L-histidine-sensitive glomerulus. Such a double innervation is not unlikely since M/T cells in *Xenopus laevis* tadpoles are known to innervate more than one glomerulus [58]. Furthermore, we observed some temperature-sensitive M/T cells extending a second dendrite into the lateral cluster [44]. Meanwhile, an indirect effect cannot be excluded. Dual sensitivity might be caused indirectly by a granule-cell mediated lateral inhibition of M/T cells modulated by the temperature-sensitive $\gamma$-glomerulus [44]. Investigating which of these mechanisms underlies the dual sensitivity will be the purpose of future experiments. In addition, it will be interesting to see how dual-sensitive M/T cells react to simultaneous or slightly delayed stimulations with cold Ringer's solution and amino acids.

The calcium-binding kinetics and fluorescence properties of fluorophores like Calcium Green are temperature-dependent [103], which may potentially cause measurement artifacts. However, our measurement design minimized such potential influences on the dye. The detection of dual-sensitive cells described in section 3.2.2 was conducted in whole-mount preparations. Consequently, the cold Ringer's solution could not reach the deeper cell layers where $[Ca^{2+}]$ was recorded from. Furthermore, the funnel position and outflow ensured that the applied stimuli did not reach the olfactory bulb as was checked by applying a Fluorescein solution through the funnel applicator.

Understanding the function of temperature sensitivity in the olfactory system will be the goal of future experiments. The data presented here revealed a strong integration of thermosensitivity processed by the $\gamma$-glomerulus into the olfactory system. The temperature information plays hence likely a crucial role for coding of odorants. Furthermore, the highly sensitive $\gamma$-glomerulus might complement temperature sensors on the skin [44].

The bilateral innervation of the $\gamma$-glomerulus was an unexpected and intriguing result. The delay between the arrival of temperature stimuli at the two nostrils can be registered by the bilaterally innervated $\gamma$-glomerulus. It is potentially used by the system for determining the direction of cold water flows. Additional experiments could evaluate the system's capability to determine the flow directions. A possible experiment paradigm involves the stimulation of the olfactory epithelia from different angles — or equivalently the stimulation of both nostrils individually with different delays between the two stimuli — and the simultaneous observation of responding M/T cells. Some indications for such a spatial detection of stimuli in the olfactory system can be found in the literature. Several studies reported that differences in either odor concentration or time delay between the two nostrils affect the spatial mapping of olfactory stimuli [44]. Such effects were reported in humans [104], moles [105], rats [106], sharks [107] and flies [108].

### 4.2.2 $\beta$-glomerulus: Amino acid sensitivity

Single olfactory receptors in mammals tend to be tuned to a relatively narrow range of odorants [85]. As previously discussed, it is assumed that each olfactory receptor neuron expresses only one type of OR and that ORNs of one class project to the same glomerulus. Consequently, glomeruli are expected to be of high selectivity in mammals. In other animals, like *Drosophila*, ORs are more often responsive to a broader range of odorants [109]. In *Xenopus laevis* tadpoles, most ORNs [98] and glomeruli [65, 89] were found to be rather narrowly tuned although there were a few exceptions. This was particularly well studied for a large number of amino acid-sensitive ORNs [98].

The broad sensitivity of the $\beta$-glomerulus reported in this dissertation is thus rather exceptional. A screening of 67 glomeruli in the lateral cluster performed by Manzini et al. [89] revealed not a single glomerulus sensitive to as many amino acids as the $\beta$-glomerulus is (cf. section 3.2.4). Interestingly, a previous study reported the existence of ORN classes in the olfactory epithelium of *Xenopus laevis* tadpoles sensitive to 15 and more individual amino acids [98]. While it was speculated that the sensitivity is narrowed further in the glomerular layer it is now very likely that some of these ORNs project to the $\beta$-glomerulus in the small cluster.

The forskolin-stimulated $[Ca^{2+}]$ increases in the $\beta$-glomerulus were surprising, given that previous studies found amino acid-sensitive ORNs to be mostly cAMP-indepen-

dent [52, 65]. The cAMP-pathway is thus potentially underpinning the mechanosensitivity as was already reported for ORNs in mice [74]. Future experiments, using for example adenylyl cyclase inhibitors, could evaluate if the mechanosensitivity, the amino acid sensitivity or both, are mediated by the cAMP transduction cascade.

Special precautions were taken to prevent pressure changes during application of amino acids (cf. section 2.3.3). In addition, regular application of odor free Ringer's solution as control verified that the pure application through the funnel did not elicit mechanical stimulation activating the $\beta$-glomerulus. Lastly, in section 3.3.3 the considerable differences in the shape of $[Ca^{2+}]$ responses caused by amino acids or Ringer's solution puffs were analyzed. In conclusion, it was possible to distinguish responses caused by odorant or mechanical stimulation very reliable. Even smaller responses to, for example, L-proline are thus unambiguously caused by the odorant itself (cf. figure 3.11).

We were able to separate presynaptic fibers within a single glomerulus and obtain recordings of $[Ca^{2+}]$ changes in these fibers. In section 3.2.5, the separation by double staining revealed a high correlation between response profiles of different axons within the $\beta$-glomerulus upon stimulation with different amino acids. Consequently, the broad sensitivity to amino acids is most likely caused by one single olfactory receptor. This is in line with a finding reported by Manzini et al. [98], i.e. broadly sensitive ORNs, albeit clearly representing a minority, do indeed exist.

In mice, a frequent co-existence of mechanosensitivity and broad sensitivity to odorants was reported [74, 85]. In the septal organ 76 % of ORNs are mechanosensitive [74]. Interestingly, the septal organ is broadly tuned to odorants, although only few ORs are expressed. Nine ORs are expressed in >90 % of the septal organ ORNs. Among these, the SR1 receptor is noticeable by its expression in about 50 % of all ORNs in the septal organ [110]. SR1 was later found to be selective to a very broad range of chemically diverse odorants [85] and, in addition, to mediate mechanosensitivity [84]. Connelly et al. [84] reported that the receptor itself endows the ORNs with their mechanosensitivity. The septal organ, with its broad sensitivity range to odorants, is speculated to serve as an outpost alerting the remaining olfactory system to the general presence of odorants [85].
The similarities between the $\beta$-glomerulus and the septal organ or more specifically

the SR1 receptor expressing ORNs – i.e. the broad sensitivity caused by only one receptor and the mechanosensitivity – suggest that it could fulfill a similar role in *Xenopus laevis*. In contrast to ORNs expressing the SR1 receptor, the broad sensitivity of the $\beta$-glomerulus was limited to one class of chemicals, namely amino acids. Amino acids are, however, of high importance in the olfactory system of *Xenopus laevis* tadpoles. The lateral cluster in the olfactory bulb is activated predominantly by amino acids [65] and contains with its $\sim$175 glomeruli about 50 % of all glomeruli in the bulb. In addition, these amino acid-sensitive glomeruli are tuned to various combinations of different amino acids [89]. The olfactory system of *Xenopus laevis* tadpoles is hence equipped with all requirements to distinguish different amino acids very precisely. The broad sensitivity to amino acids observed in the $\beta$-glomerulus covers thus a significant amount of relevant stimuli and qualifies accordingly as a general reporter for changes in the odorant environment.
Alerting the olfactory system to changes in the odorant composition might be especially helpful for latency-mediated odor coding. Recently, this type of coding based on first-spike latencies in M/T cells has been suggested by a number of studies [17, 111–113]. A predicting signal provided by the $\beta$-glomerulus could serve as a starting point of a new latency pattern.

### 4.2.3 $\beta$-glomerulus: Mechanosensitivity

$[Ca^{2+}]$ increases were registered in the $\beta$-glomerulus in response to Ringer's solution puffs delivered to the olfactory epithelium. Puffs were generated with a pressure range of 0 to 250 hPa. Only the $\beta$-glomerulus showed puff-related activity, suggesting that it is especially sensitive to mechanical stimulation. The limitation of $[Ca^{2+}]$ increases to the $\beta$-glomerulus is a first indication that the applied pressure range is physiological and thus an adequate stimulus. Pressure amplitudes above the physiological range should stimulate a broad range of ORNs and not only one specific set. Indeed, stronger pressure pulses sometimes activated additional axons in the olfactory bulb. Additionally, the finely tuned dose response curve with its half maximum value at 78 hPa supports the notion that the $\beta$-glomerulus is processing mechanical stimulations.
Similar experiments were performed in mice and a pressure range of 0 to 2757 hPa was used for stimulation [74]. The effective pressure amplitude reaching the ORNs was, however, estimated to about 8 hPa only [74]. The value is considerably lower than the amplitudes used in our experiments. However, this discrepancy can be ex-

plained by several differences between the experiments. First of all, the physiological pressure range for mice was derived from the pressure expected in the nose during sniffing [74]. Conversely, the nostrils of tadpoles are waterfilled and tadpoles are neither inhaling nor exhaling. The pressure changes caused by alternations of the flow or by movement of the tadpole are hence more relevant for the tadpole olfactory system than sniffs. The pressure amplitudes applied in our experiments can be converted to corresponding flow rates in a range of 0 to 0.56 m/s at the pipette tip and a half maximum value of the dose response curve at about 0.17 m/s (compare section 2.3.3). These flow rates can easily be reached during normal movement of the tadpoles. The maximal movement speed of Hyla versicolor tadpoles is for example 0.27 m/s [114]. The Ringer's solution puffs applied fall thus in a physiologically relevant range.
It is, furthermore, noteworthy that the pressure amplitudes applied should be considered upper limits. The pressure amplitudes as well as the flow rates were measured before or at the pipette tip. The nostril was, however, positioned 0.9 mm downstream. Leakage along the tubes, the distance between pipette and epithelium, the shape of the nostril, and the location of the ORNs all influence the final pressure amplitude. Some of these effects have been corrected for (cf. section 2.3.3). Grosmaitre et al. [74] removed the epithelium from the nose and stimulated the ORNs directly, which is especially important for the comparison with our measurements. The nostrils of the tadpoles were left intact, resulting in a more natural behavior of the flow over the ORNs. This flow is considerably affected by the shape of the nostrils and also the movement of cilia. Studying the flow within the nostrils will be important to better understand the registration of both odorants as well as mechanical stimuli in the olfactory system.

The dose-response curve of the $\beta$-glomerulus suggests that the olfactory system processes detailed information about the registered strength of mechanical stimulations. Mechanosensitive M/T cells showed different response dynamics (data not shown) potentially shaping the range of distinguishable pressure amplitudes further, similar as described for the temperature-sensitive M/T cells [44].
The limitation of the $[Ca^{2+}]$ increases in the olfactory bulb to the $\beta$-glomerulus in response to Ringer's solution puffs suggests a rather specialized registration of this modality. In contrast, in mice a large number of ORNs was found to be mechanosensitive, both in the septal organ (76 %) and the main olfactory organ (49 %). Con-

nelly et al. [84] reported that G-protein-coupled receptors underlie the observed mechanosensitivity whereas typically force-gated ion channels are thought to be responsible for mechanosensitivity. Even more intriguingly, different ORs provide differently tuned mechanosensitivity — and of course many are not mechanosensitive at all. These facts converge with our description of a single mechanosensitive glomerulus in *Xenopus laevis* tadpoles where one can speculate that only the OR expressed in ORNs innervating the $\beta$-glomerulus is sensitive to the applied pressure amplitudes. Mechanosensitivity in combination with broad odorant sensitivity as observed in the septal organ of mice was also observed in the $\beta$-glomerulus (cf. section 3.2.4).

The purpose of pressure detection and processing in the olfactory system remains unclear. However, a couple of interpretations are supported by different experiments. Since only the $\beta$-glomerulus was found to be mechanosensitive it might fulfill the single purpose of providing additional information about pressure amplitudes or flow rates to the olfactory system. The impact of Ringer's solution puffs over many M/T cells and especially the inhibition observed (cf. section 3.2.7) suggests, however, that this information is used on a larger scale to influence and shape the responses of the olfactory system.
The beneficial effect of a predicting signal for latency coding was discussed above. Since the flow dynamics within the nostril are especially crucial for this kind of coding, information about the flow rate may be of particular importance. Mainland et al. [115] described that sniffing is actually an important part in the odorant perception in humans. Integrating flow rates and odor responses during sniffs is considered a prerequisite to estimating odor qualities and intensities [74, 115]. Although tadpoles do not sniff, flow changes caused by movement need to be compensated. Grosmaitre et al. [74] reported that mechanosensitivity of ORNs in mice is necessary for the synchronization of rhythmic activity in the olfactory bulb with respiration. Mori et al. [83] speculated that both temperature and mechanosensitivity are used to measure the precise timing of inhaling and exhaling phases. A flow through the olfactory system is actively produced not only by sniffing in mammals but also by other types of behavior in different species [38]. Snakes flick their tongue to bring odorants to the vomeronasal organ [116] and flounders and other aquatic animals actively pump water through their nasal chamber [38, 117]. Also in tadpoles, flow changes equivalent to the inhaling and exhaling observed in rodents, might

be actively induced since tadpoles are seldom at rest but show instead a rhythmic up-and-down movement. On the other hand, only one glomerulus in *Xenopus laevis* tadpoles was found to be mechanosensitive whereas a large number of ORNs in mice is mechanosensitive. This might indicate that mechanosensitivity is of higher importance for animals with breathing cycles.
Lastly, the mechanosensitivity of ORNs in mice enhances the firing rate in response to weak odorant stimulations if these stimuli are accompanied by a pressure change [74]. Analyzing the effect of simultaneous or slightly shifted application of puffs and odorant stimulation will be very interesting, especially at the M/T cell level. The inhibition observed by mechano-stimulation (cf. figure 3.15) might influence the subsequent processing of odorants in M/T cells and enhance the contrast because spontaneous activity is suppressed. Preliminary experiments indicated that a pressure pulse followed by stimulation with odorants led indeed to a sharp and well separated [$Ca^{2+}$] peak in some M/T cells. However, the delivery of pressure pulses had a tendency to disturb the stimulation with odorants demanding additional experiments with more sophisticated application setups.

## 4.3 Axon and dendrite separation for 2-channel calcium imaging

A red calcium indicator which can be electroporated into ORNs of *Xenopus laevis* tadpoles was not available during this thesis and prohibited further experiments with two calcium-sensitive dyes. However, recent developments of such fluorophores show promising results. The imaging techniques used throughout this thesis will be valuable for simultaneous calcium recordings on first- and second-order neurons in the olfactory bulb:
Combining the LIM's 3D imaging capabilities in two channels with efficient calcium indicators will allow the simultaneous recording of [$Ca^{2+}$] changes in both pre- and postsynaptic neurons in the olfactory bulb at the same time. This is possible at the level of single fibers within a single glomerulus as was shown in section 3.3. The separation of single axons via double electroporation was already discussed above. The activity based separation depends on the development of new calcium indicators but first promising results were obtained demonstrating the feasibility (cf. figure 3.17, [102]). Improvements of optical sectioning capability are highly important within

the densely innervated glomeruli to differentiate fibers reliably. Signals recorded from out-of-focus components due to insufficient optical sectioning can induce an artificial similarity of fiber responses throughout the glomerulus and would render ACI useless. Therefore, subtraction imaging improved the result and success rate of both techniques considerably. Glomeruli are innervated by ORN axons in complicated ways and the axons branch multiple times within the glomerulus [62] (cf. section 3.3.2). Separation of fibers within a glomerlus relies thus on three dimensional recordings as performed in section 3.2.5. Otherwise, only unconnected cross sections of axons will be visible.

Generating activity traces with mechanical stimulation sequences was effective for obtaining a good resolution of dendrites using activity correlation imaging. Here, the stimulation was performed with interstimulus intervals of 25 s. Septal organ neurons in mice follow mechanical stimulations with frequencies of up to 0.5 Hz [74]. Stimulation by pressure pulses of the $\beta$-glomerulus is thus likely possible with even shorter and more frequent applications. This is not only interesting for the generation of activity correlation imaging-based contrast but will also enable new experiments on signal transmission from first- to second-order neurons.

# 5 Summary

In this thesis several techniques for line illumination microscopy have been introduced and evaluated. Detection based on an sCMOS camera yielded high frame rates and a flexible readout. Two measurement channels were realized by switching the excitation with acousto-optic modulators. Besides, the recording of off-center camera pixels was used for subtraction imaging and pixel reassignment. The usefulness of the two latter techniques was evaluated for line scanning systems. Subtraction imaging had a positive effect on the optical sectioning capability. Pixel reassignment improved the lateral resolution and the signal-to-noise ratio. Both techniques can be used individually or in combination. In conclusion, the line illumination microscope was shaped into a flexible and efficient tool and used throughout this thesis to extend calcium imaging in the olfactory bulb from single plane recordings to fast volume acquisitions.

Differentially tuned M/T cells of *Xenopus laevis* tadpoles sensitive to both temperature and chemicals were found in the proximity of the $\gamma$-glomerulus. This finding shows that temperature sensitivity is strongly connected with the processing of odor information in the olfactory bulb.
Further investigations in the small cluster in the olfactory bulb revealed that the $\beta$-glomerulus responds to mechanical stimulations delivered to the olfactory epithelium. A dose-response curve was recorded for a range of pressure amplitudes. Furthermore, the adaptation of the $\beta$-glomerulus was shown in response to prolonged stimulation with Ringer's solution puffs. The neuropil is thus sensitive to pressure or flow changes instead of absolute values. Activity induced by Ringer's solution puffs was transferred to second-order neurons in which it caused both excitatory as well as inhibitory effects on a larger scale. Consequently, mechanosensitivity, although limited to a single glomerulus on the presynaptic side, has a widespread influence on the olfactory system.
The $\beta$-glomerulus was in all measured animals amino acid-sensitive and reacted to

forskolin, an activator of the cAMP-mediated pathway. The sensitivity to amino acids observed was much broader for the $\beta$-glomerulus than for the other glomeruli of *Xenopus laevis* tadpoles. Measurements conducted on pairs of single axons within the $\beta$-glomerulus revealed a very similar response profile of the ORNs innervating the $\beta$-glomerulus. It is thus very likely that the broad sensitivity of the $\beta$-glomerulus is caused by only one broadly tuned olfactory receptor.

Finally, we have shown that simultaneous measurements in two channels can be performed to differentiate single fibers within a glomerulus. In order to resolve single dendrites, a specific calcium response pattern was generated by stimulation with a sequence of pressure pulses. Subsequently, this trace was used as a reference trace in ACI. The two results enable simultaneous calcium measurements in pre- and postsynaptic fibers within a single glomerulus.

# Bibliography


[1] L. Schermelleh, R. Heintzmann, and H. Leonhardt. A guide to super-resolution fluorescence microscopy. *The Journal of Cell Biology*, 190(2):165–175, July 2010.

[2] J. Jonkman and C. M. Brown. Any way you slice it—a comparison of confocal microscopy techniques. *Journal of Biomolecular Techniques: JBT*, 26(2):54, 2015.

[3] S. Junek, T.-W. Chen, M. Alevra, and D. Schild. Activity correlation imaging: visualizing function and structure of neuronal populations. *Biophysical Journal*, 96(9):3801–3809, May 2009.

[4] L. M. Loew. Design and use of organic voltage sensitive dyes. In *Membrane potential imaging in the nervous system*, pages 13–23. Springer, 2010.

[5] K. Michel, M. Michaelis, G. Mazzuoli, K. Mueller, P. Vanden Berghe, and M. Schemann. Fast calcium and voltage-sensitive dye imaging in enteric neurones reveal calcium peaks associated with single action potential discharge. *The Journal of Physiology*, 589(Pt 24):5941–5947, December 2011.

[6] B.-J. Lin, T.-W. Chen, and D. Schild. Cell type-specific relationships between spiking and [Ca2+]i in neurons of the Xenopus tadpole olfactory bulb. *The Journal of Physiology*, 582(Pt 1):163–175, July 2007.

[7] R. Gräf, J. Rietdorf, and T. Zimmermann. Live cell spinning disk microscopy. In *Advances in Biochemical Engineering/Biotechnology*, volume 95, pages 57–75. Springer, 2005.

[8] T. Mappes, N. Jahr, A. Csaki, N. Vogler, J. Popp, and W. Fritzsche. The invention of immersion ultramicroscopy in 1912-The birth of nanotechnology? *Angewandte Chemie - International Edition*, 51(45):11208–11212, 2012.

[9] A. H. Voie, D. H. Burns, and F. A. Spelman. Orthogonal-plane fluorescence optical sectioning: three-dimensional imaging of macroscopic biological specimens. *Journal of Microscopy*, 170(Pt 3):229–236, 1993.

[10] J. Huisken and D. Y. R. Stainier. Even fluorescence excitation by multidirectional selective plane illumination microscopy (mSPIM). *Optics Letters*, 32(17):2608–2610, September 2007.

[11] G. D. Reddy and P. Saggau. Fast three-dimensional laser scanning scheme using acousto-optic deflectors. *Journal of Biomedical Optics*, 10(6):064038–064038, 2005.

[12] R. Salome, Y. Kremer, S. Dieudonne, J.-F. Léger, O. Krichevsky, C. Wyart, D. Chatenay, and L. Bourdieu. Ultrafast random-access scanning in two-photon microscopy using acousto-optic deflectors. *Journal of Neuroscience Methods*, 154(1):161–174, 2006.

[13] G. Katona, G. Szalay, P. Maák, A. Kaszás, M. Veress, D. Hillier, B. Chiovini, E. S. Vizi, B. Roska, and B. Rózsa. Fast two-photon in vivo imaging with three-dimensional random-access scanning in large tissue volumes. *Nature Methods*, 9(2):201–208, 2012.

[14] M. A. Martens, W. Boesmans, and P. Vanden Berghe. Calcium imaging at kHz frame rates resolves millisecond timing in neuronal circuits and varicosities. *Biomedical Optics Express*, 5(8):2648–61, 2014.

[15] P. J. Keller, A. D. Schmidt, J. Wittbrodt, and E. H. K. Stelzer. Reconstruction of zebrafish early embryonic development by scanned light sheet microscopy. *Science*, 322(5904):1065–9, 2008.

[16] P. A. Santi. Light Sheet Fluorescence Microscopy A Review. *Journal of Histochemistry and Cytochemistry*, 59(2):129–138, 2011.

[17] S. Junek, E. Kludt, F. Wolf, and D. Schild. Olfactory Coding with Patterns of Response Latencies. *Neuron*, 67(5):872–884, September 2010.

[18] D. M. Maurice. A Scanning Slit Optical Microscope. *Investigative Ophthalmology & Visual Science*, 13(12):1033–1037, December 1974.

[19] C.J.R. Sheppard and X.Q. Mao. Confocal Microscopes with Slit Apertures. *Journal of Modern Optics*, 35(7):1169–1185, 1988.

[20] K.-B. Im, S. Han, H. Park, D. Kim, and B.-M. Kim. Simple high-speed confocal line-scanning microscope. *Optics Express*, 13(13):5151, 2005.

[21] B. R. Masters and A. A. Thaer. In vivo human corneal confocal microscopy of identical fields of subepithelial nerve plexus, basal epithelial, and wing cells at different times. *Microscopy Research and Technique*, 29(5):350–356, December 1994.

[22] R. Engelmann. Faster than real-time: confocal linescan systems provide ideal conditions for millisecond-resolution physiological imaging. *Nature Methods*, 3(11), November 2006.

[23] A. Brinkmann. Design, construction and characterisation of a line illumination microscope. Master's thesis, Georg-August-Universität Göttingen, 2013.

[24] E. Mei, P. A. Fomitchov, R. Graves, and M. Campion. A line scanning confocal fluorescent microscope using a CMOS rolling shutter as an adjustable aperture. *Journal of Microscopy*, 247(3):269–76, September 2012.

[25] C. J. R. Sheppard, S. B. Mehta, and R. Heintzmann. Superresolution by image scanning microscopy using pixel reassignment. *Optics Letters*, 38(15):2889–2892, 2013.

[26] C. B. Müller and J. Enderlein. Image Scanning Microscopy. *Physical Review Letters*, 104(19):198101, May 2010.

[27] C.J.R. Sheppard and C.J. Cogswell. Confocal Microscopy with Detector Arrays. *Journal of Modern Optics*, 37(2):267–279, 1990.

[28] E. Sánchez-Ortiga, G. Saavedra, M. Martínez-corral, and A. Doblas. Confocal scanning microscope using a CCD camera as a pinhole-detector system. *Conference: Information Optics*, pages 2–4, 2011.

[29] V. Poher, G. T. Kennedy, H. B. Manning, D. M. Owen, H. X. Zhang, E. Gu, M. D. Dawson, P. M. W. French, and M. A. A. Neil. Improved sectioning in a slit scanning confocal microscope. *Optics Letters*, 33(16):1813–1815, August 2008.

[30] C. J. R. Sheppard. Super-resolution in confocal imaging. *Optik*, 80:5354, 1988.

[31] K. Weisshart. The Basic Principle of Airyscanning. *Zeiss Technology Note*, July 2014.

[32] S. Roth, C. J. R. Sheppard, K. Wicker, and R. Heintzmann. Optical photon reassignment microscopy (OPRA). *Optical Nanoscopy*, 2(1):5, 2013.

[33] M. Wachowiak and M. T. Shipley. Coding and synaptic processing of sensory information in the glomerular layer of the olfactory bulb. *Seminars in Cell & Developmental Biology*, 17(4):411–423, August 2006.

[34] D.-J. Zou, A. Chesler, and S. Firestein. How the olfactory bulb got its glomeruli: a just so story? *Nature Reviews. Neuroscience*, 10(8):611–8, 2009.

[35] C. Y. Su, K. Menuz, and J. R. Carlson. Olfactory Perception: Receptors, Cells, and Circuits. *Cell*, 139(1):45–59, 2009.

[36] N. Uchida, C. Poo, and R. Haddad. Coding and Transformations in the Olfactory System. *Annual Review of Neuroscience*, (May):363–385, 2013.

[37] J. G. Hildebrand and G. M. Shepherd. Mechanisms Of Olfactory Discrimination : Converging Evidence for Common Principles Across Phyla. *Annual Review of Neuroscience*, pages 595–631, 1997.

[38] B. W. Ache and J. M. Young. Olfaction: Diverse species, conserved principles. *Neuron*, 48(3):417–430, 2005.

[39] G. N. Wheeler and A. W. Brändli. Simple vertebrate models for chemical genetics and drug discovery screens: Lessons from zebrafish and Xenopus. *Developmental Dynamics*, 238(6):1287–1308, 2009.

[40] D. Czesnik, W. Rössler, F. Kirchner, A. Gennerich, and D. Schild. Neuronal representation of odourants in the olfactory bulb of Xenopus laevis tadpoles. *European Journal of Neuroscience*, 17(1):113–118, 2003.

[41] A. Brinkmann, C. Okom, E. Kludt, and D. Schild. Recording Temperature-induced Neuronal Activity through Monitoring Calcium Changes in the Olfactory Bulb of Xenopus laevis. *Journal of Visualized Experiments*, (112):1–9, 2016.

[42] J. Gascuel and T. Amano. Exotic models may offer unique opportunities to decipher specific scientific question: the case of Xenopus olfactory system. *The Anatomical Record*, 296(9):1453–61, September 2013.

[43] E. Kludt. *Bilateral processing of thermoreception in the olfactory system of larval Xenopus laevis*. PhD thesis, Georg-August-Universität Göttingen, 2009.

[44] E. Kludt, C. Okom, A. Brinkmann, and D. Schild. Integrating Temperature with Odor Processing in the Olfactory Bulb. *The Journal of Neuroscience*, 35(20):7892–7902, 2015.

[45] F. Lang and P. Lang. *Basiswissen Physiologie*. Springer, Lehrbuch, 2007.

[46] T. V. Getchell. Functional properties of vertebrate olfactory receptor neurons. *Physiological reviews*, 66(3):772–818, July 1986.

[47] G. H. Gold. Controversial issues in vertebrate olfactory transduction. *Annual Review of Physiology*, 61(1):857–71, 1999.

[48] J. E. Schwob. Neural regeneration and the peripheral olfactory system. *Anatomical Record*, 269(1):33–49, 2002.

[49] U. B. Kaupp. Olfactory signalling in vertebrates and insects: differences and commonalities. *Nature Reviews. Neuroscience*, 11(3):188–200, 2010.

[50] S. J. Kleene. The electrochemical basis of odor transduction in vertebrate olfactory cilia. *Chemical Senses*, 33(9):839–859, 2008.

[51] D. Schild and D. Restrepo. Transduction mechanisms in vertebrate olfactory receptor cells. *Physiological Reviews*, 78(2):429–66, April 1998.

[52] I. Manzini and D. Schild. cAMP-independent olfactory transduction of amino acids in Xenopus laevis tadpoles. *The Journal of Physiology*, 551(1):115–123, August 2003.

[53] A. Sansone, T. Hassenklöver, A. S. Syed, S. I. Korsching, and I. Manzini. Phospholipase C and diacylglycerol mediate olfactory responses to amino acids in the main olfactory epithelium of an amphibian. *PLOS ONE*, 9(1):e87721, January 2014.

[54] Peter Mombaerts. Odorant receptor gene choice in olfactory sensory neurons: the one receptor–one neuron hypothesis revisited. *Current Opinion in Neurobiology*, 14(1):31–36, 2004.

[55] L. Tan, Q. Li, and X. S. Xie. Olfactory sensory neurons transiently express multiple olfactory receptors during development. *Molecular Systems Biology*, 11(12):844, 2015.

[56] P. Mombaerts. Axonal wiring in the mouse olfactory system. *Annual Review of Cell and Developmental Biology*, 22:713–37, 2006.

[57] L. Belluscio and L. C. Katz. Symmetry, stereotypy, and topography of odorant representations in mouse olfactory bulbs. *The Journal of Neuroscience*, 21(6):2113–2122, 2001.

[58] L. P. Nezlin, S. Heermann, D. Schild, and W. Rössler. Organization of glomeruli in the main olfactory bulb of Xenopus laevis tadpoles. *Journal of Comparative Neurology*, 464(3):257–268, 2003.

[59] I. Manzini, S. Heermann, D. Czesnik, C. Brase, D. Schild, and W. Rössler. Presynaptic protein distribution and odour mapping in glomeruli of the olfactory bulb of Xenopus laevis tadpoles. *The European Journal of Neuroscience*, 26(4):925–934, August 2007.

[60] A. Gaudin and J. Gascuel. 3D atlas describing the ontogenic evolution of the primary olfactory projections in the olfactory bulb of Xenopus laevis. *The Journal of Comparative Neurology*, 489(4):403–24, September 2005.

[61] L. P. Nezlin and D. Schild. Individual olfactory sensory neurons project into more than one glomerulus in Xenopus laevis tadpole olfactory bulb. *The Journal of comparative neurology*, 481(3):233–239, January 2005.

[62] T. Hassenklöver and I. Manzini. Olfactory Wiring Logic in Amphibians Challenges the Basic Assumptions of the Unbranched Axon Concept. *The Journal of Neuroscience*, 33(44):17247–17252, October 2013.

[63] L. Dryer and P. P. C. Graziadei. Mitral cell dendrites: a comparative approach. *Anatomy and Embryology*, 189(2):91–106, 1994.

[64] W. E. S. Carr and C. D. Derby. Chemically stimulated feeding behavior in marine animals - Importance of chemical mixtures and involvement of mixture interactions. *Journal of Chemical Ecology*, 12(5):989–1011, 1986.

[65] S. Gliem, A. S. Syed, A. Sansone, E. Kludt, E. Tantalaki, T. Hassenklöver, S. I. Korsching, and I. Manzini. Bimodal processing of olfactory information in an amphibian nose: odor responses segregate into a medial and a lateral stream. *Cellular and Molecular Life Sciences: CMLS*, 70(11):1965–1984, June 2013.

[66] R. W. Friedrich and S. I. Korsching. Combinatorial and chemotopic odorant coding in the zebrafish olfactory bulb visualized by optical imaging. *Neuron*, 18(5):737–752, 1997.

[67] E. Yaksi, B. Judkewitz, and R. W. Friedrich. Topological reorganization of odor representations in the olfactory bulb. *PLoS Biology*, 5(7):1453–1473, 2007.

[68] S. H. Rolen, P. W. Sorensen, D. Mattson, and J. Caprio. Polyamines as olfactory stimuli in the goldfish Carassius auratus. *The Journal of Experimental Biology*, 206(Pt 10):1683–1696, 2003.

[69] P. Mombaerts. Seven-transmembrane proteins as odorant and chemosensory receptors. *Science*, 286(5440):707–711, 1999.

[70] Y. Niimura and M. Nei. Evolutionary dynamics of olfactory receptor genes in fishes and tetrapods. *Proceedings of the National Academy of Sciences*, 102(17):6039–6044, 2005.

[71] K. Mamasuew, H. Breer, and J. Fleischer. Grueneberg ganglion neurons respond to cool ambient temperatures. *The European Journal of Neuroscience*, 28(9):1775–85, November 2008.

[72] J. Brechbühl, M. Klaey, F. Moine, E. Bovay, N. Hurni, M. Nenniger-Tosato, and M.-C. Broillet. Morphological and physiological species-dependent characteristics of the rodent Grueneberg ganglion. *Frontiers in Neuroanatomy*, 8(August):87, 2014.

[73] D. D. Frank, G. C. Jouandet, P. J. Kearney, L. J. Macpherson, and M. Gallio. Temperature representation in the Drosophila brain. *Nature*, 519(7543):358–61, 2015.

[74] X. Grosmaitre, L. C. Santarelli, J. Tan, M. Luo, and M. Ma. Dual functions of mammalian olfactory sensory neurons as odor detectors and mechanical sensors. *Nature Neuroscience*, 10(3):348–354, March 2007.

[75] J. Brechbühl, F. Moine, and M.-C. Broillet. Mouse Grueneberg ganglion neurons share molecular and functional features with C. elegans amphid neurons. *Frontiers in Behavioral Neuroscience*, 7(December):193, 2013.

[76] J. Brechbühl, M. Klaey, and M.-C. Broillet. Grueneberg ganglion cells mediate alarm pheromone detection in mice. *Science*, 321(5892):1092–5, 2008.

[77] W. Hanke, K. Mamasuew, M. Biel, R. B. Yang, and J. Fleischer. Odorant-evoked electrical responses in Grueneberg ganglion neurons rely on cGMP-associated signaling proteins. *Neuroscience Letters*, 539:38–42, 2013.

[78] K. Mamasuew, N. Hofmann, H. Breer, and J. Fleischer. Grueneberg ganglion neurons are activated by a defined set of odorants. *Chemical Senses*, 36(3):271–82, March 2011.

[79] S. H. Fuss, M. Omura, and P. Mombaerts. The Grueneberg ganglion of the mouse projects axons to glomeruli in the olfactory bulb. *The European Journal of Neuroscience*, 22(10):2649–54, 2005.

[80] A. Schmid, M. Pyrski, M. Biel, T. Leinders-Zufall, and F. Zufall. Grueneberg ganglion neurons are finely tuned cold sensors. *The Journal of Neuroscience*, 30(22):7563–8, June 2010.

[81] C. Y. Liu, S. E. Fraser, and D. S. Koos. Grueneberg ganglion olfactory subsystem employs a cGMP signaling pathway. *Journal of Comparative Neurology*, 516(1):36–48, 2009.

[82] K. Mamasuew, S. Michalakis, H. Breer, M. Biel, and J. Fleischer. The cyclic nucleotide-gated ion channel cnga3 contributes to coolness-induced responses of grueneberg ganglion neurons. *Cellular and Molecular Life Sciences*, 67(11):1859–1869, 2010.

[83] K. Mori, H. Manabe, and K. Narikiyo. Possible functional role of olfactory subsystems in monitoring inhalation and exhalation. *Frontiers in Neuroanatomy*, 8(September):107, 2014.

[84] T. Connelly, Y. Yu, X. Grosmaitre, J. Wang, L. C. Santarelli, A. Savigner, X. Qiao, Z. Wang, D. R. Storm, and M. Ma. G protein-coupled odorant receptors underlie mechanosensitivity in mammalian olfactory sensory neurons. *Proceedings of the National Academy of Sciences*, 112(2):590–595, 2015.

[85] X. Grosmaitre, S. H. Fuss, A. C. Lee, K. A. Adipietro, H. Matsunami, P. Mombaerts, and M. Ma. SR1, a mouse odorant receptor with an unusually broad response profile. *The Journal of Neuroscience*, 29(46):14545–14552, 2009.

[86] M. A. Model and J. L. Blank. Concentrated dyes as a source of two-dimensional fluorescent field for characterization of a confocal microscope. *Journal of Microscopy*, 229(1):12–16, 2008.

[87] P.D. Nieuwkoop and J. Faber. *Normal table of Xenopus laevis (Daudin)*. New York: Garland Publishing, 1994.

[88] J. Caprio and R. P. Byrd. Electrophysiological evidence for acidic, basic, and neutral amino acid olfactory receptor sites in the catfish. *The Journal of General Physiology*, 84(3):403–422, 1984.

[89] I. Manzini, C. Brase, T.-W. Chen, and D. Schild. Response profiles to amino acid odorants of olfactory glomeruli in larval Xenopus laevis. *The Journal of Physiology*, 581(2):567–579, June 2007.

[90] H. Altner. Untersuchungen über Leistungen und Bau der Nase des südafrikanischen Krallenfrosches Xenopus Laevis (Daudin, 1803). *Journal of Comparative Physiology A: Neuroethology, Sensory, Neural, and Behavioral Physiology*, 45:272–306, 1962.

[91] D. Schild. A computer-controlled device for the application of odors to aquatic animals. *Journal of Electrophysiological Techniques*, 12:71–79, 1985.

[92] G. Bao and D. Schild. Fast and accurate fitting and filtering of noisy exponentials in legendre space. *PloS ONE*, 9(3):e90500, 2014.

[93] Life Technologies Corporation. Alexa Fluor 647, Rhod-2, Calcium Green Spectra. *http://www.lifetechnologies.com/de/de/home/life-science/cell-analysis/labeling-chemistry/fluorescence-spectraviewer.html.*, Accessed on June 2016.

[94] R. Heintzmann, V. Sarafis, P. Munroe, J. Nailon, Q. S. Hanley, and T. M. Jovin. Resolution enhancement by subtraction of confocal signals taken at different pinhole sizes. *Micron*, 34(6–7):293–300, October 2003.

[95] R. Wolleschensky, B. Zimmermann, R. Ankerhold, and M. Kempe. High-speed scanning confocal microscope for the life sciences. In *European Conference on Biomedical Optics 2005*, pages 58600N–58600N. International Society for Optics and Photonics, 2005.

[96] E. Dusch, T. Dorval, N. Vincent, M. Wachsmuth, and A. Genovesio. Three-dimensional point spread function model for line-scanning confocal microscope with high-aperture objective. *Journal of Microscopy*, 228(2):132–138, 2007.

[97] A. Brinkmann and D. Schild. One special glomerulus in the olfactory bulb of Xenopus laevis tadpoles integrates a broad range of amino acids and mechanical stimuli. *The Journal of Neuroscience*, 2016 (Accepted).

[98] I. Manzini and D. Schild. Classes and Narrowing Selectivity of Olfactory Receptor Neurons of Xenopus laevis Tadpoles. *The Journal of General Physiology*, 123(2):99–107, February 2004.

[99] D. Schild and I. Manzini. Cascades of response vectors of olfactory receptor neurons in Xenopus laevis tadpoles. *European Journal of Neuroscience*, 20(8):2111–2123, 2004.

[100] D.-J. Zou, P. Feinstein, A. L. Rivers, G. A. Mathews, A. Kim, C. A. Greer, P. Mombaerts, and S. Firestein. Postnatal refinement of peripheral olfactory projections. *Science*, 304(5679):1976–1979, 2004.

[101] The Molecular Probes Handbook—A Guide to Fluorescent Probes and Labeling Technologies. *Thermo Fisher Scientific*, 2016.

[102] D. de Jong. *Glomerular information processing in Xenopus laevis*. PhD thesis, Georg-August-Universität Göttingen, 2016.

[103] A. E. Oliver, G. A. Baker, R. D. Fugate, F. Tablin, and J. H. Crowe. Effects of temperature on calcium-sensitive fluorescent probes. *Biophysical Journal*, 78(April):2116–2126, 2000.

[104] J. Porter, T. Anand, B. Johnson, R. M. Khan, and N. Sobel. Brain mechanisms for extracting spatial information from smell. *Neuron*, 47(4):581–592, 2005.

[105] K. C. Catania. Stereo and serial sniffing guide navigation to an odour source in a mammal. *Nature Communications*, 4:1441, 2013.

[106] R. Rajan, J. P. Clement, and U. S. Bhalla. Rats Smell in Stereo. *Science*, 311(February):666–670, 2006.

[107] J. M. Gardiner and J. Atema. The function of bilateral odor arrival time differences in olfactory orientation of sharks. *Current Biology*, 20(13):1187–1191, 2010.

[108] B. J. Duistermars, D. M. Chow, and M. a. Frye. Flies Require Bilateral Sensory Input to Track Odor Gradients in Flight. *Current Biology*, 19(15):1301–1307, 2009.

[109] E. A. Hallem and J. R. Carlson. Coding of Odors by a Receptor Repertoire. *Cell*, 125(1):143–160, 2006.

[110] H. Tian and M. Ma. Molecular organization of the olfactory septal organ. *The Journal of Neuroscience*, 24(38):8383–90, 2004.

[111] H. Spors, M. Wachowiak, L. B. Cohen, and R. W. Friedrich. Temporal dynamics and latency patterns of receptor neuron input to the olfactory bulb. *The Journal of Neuroscience*, 26(4):1247–59, January 2006.

[112] A. T. Schaefer and T. W. Margrie. Spatiotemporal representations in the olfactory system. *Trends in Neurosciences*, 30(3):92–100, 2007.

[113] B. Bathellier, D. L. Buhl, R. Accolla, and A. Carleton. Dynamic Ensemble Odor Coding in the Mammalian Olfactory Bulb: Sensory Information at Different Timescales. *Neuron*, 57(4):586–598, 2008.

[114] J. Van Buskirk and S. A. McCollum. Influence of tail shape on tadpole swimming performance. *The Journal of Experimental Biology*, 203(Pt 14):2149–2158, 2000.

[115] J. Mainland and N. Sobel. The sniff is part of the olfactory percept. *Chemical Senses*, 31(2):181–196, 2006.

[116] M. Halpern and J. L. Kubie. Snake tongue flicking behavior: Clues to vomeronasal system functions. In *Chemical signals in vertebrates 3*, pages 45–72. Springer, 1983.

[117] K. B. Døving and G. Thommesen. Some properties of the fish olfactory system. *Olfaction and Taste*, 6:175–183, 1977.

# Danksagung

Schlussendlich möchte ich mich noch für die großartige Unterstützung, Hilfe und Freundschaft bedanken, die ich während meiner gesamten Zeit als Doktorand erfahren habe:
Mein aller erster Dank geht an **Prof. Dr. Dr. Detlev Schild**, dafür dass er es mir ermöglicht hat diese Arbeit durchzuführen, für seine Betreuung, Hilfe und die vielen inspirierenden Gespräche. Durch die Themenvielfalt und die Freiheit bei der Umsetzung neuer Ideen werde ich die Zeit in Ihrem Institut immer als eine der interessantesten und angenehmsten in Erinnerung behalten.
Bei **Prof. Dr. Tim Salditt** bedanke ich mich für seine langjährige Begleitung durch mein Studium, die Unterstützung in meinem Thesis-Komitee und die Begutachtung dieser Arbeit.
**Prof. Dr. André Fiala** danke ich für die Betreuung in meinem Thesis-Komitee und die weitere angenehme Zusammenarbeit.
**Prof. Dr. Swen Hülsmann, Prof. Dr. Michael Müller** und **Dr. Katrin Willig** möchte ich für die Bereitschaft danken, als Prüfer an meiner Verteidigung teilzunehmen.
Im Besonderen möchte ich mich noch bei **Camille Okom** für die großartige Büronachbarschaft, die gemeinsame Arbeit an Veröffentlichungen und Videos sowie die gute Freundschaft bedanken. **Mihai Alevra** und **Guobin Bao** bin ich ebenfalls dankbar für die Freundschaft und die viele Hilfe bei dem Auf- und Umbau des LIMs. Zu letzterem haben auch **Jens Kowalski** und **Torsten Nägel** mit Ihrer Unterstützung bei allen elektronischen Sonderanfertigungen beigetragen. Danke dafür! **Christina Patzelt** hat mir mit der Vorbereitung der diversen Experimente und der Versorgung der Kaulquappen weitergeholfen, wofür ich ihr danke. Weiterhin danke ich für das Korrekturlesen dieser Arbeit: **Bernd Nöding, Jakob Eifler** und **Camille Okom**. Darüberhinaus möchte ich mich bei der gesamten Arbeitsgruppe und den Arbeitsgruppen von **Dr. Ivan Manzini** und **Prof. Dr. Hülsmann** für die angehme Arbeitsatmosphäre sowie die Freundschaft während dieser Zeit bedanken. Durch die

gemeinsamen Laborseminare, Ausflüge und sicherlich nicht zuletzt die Kaffeerunden ist meine Doktorandenzeit erst zu der großartigen Erfahrung geworden, die sie jetzt für mich darstellt.
Nicht zuletzt geht ein riesiges Dankeschön natürlich und immer an meine Eltern und meine Frau: Vielen Dank für all die Hilfe, Motivation und Unterstützung!